Engineering Journal

Third Quarter 2025 | Volume 62, No. 3

Smarter.
Stronger.
Steel.

83 A Numerical Study on the Buckling Behavior of Austenitic Stainless Steel Unequal-Leg Angle Columns
Edward J. Sippel and Hannah B. Blum

105 Review and Evaluation of the Separation Factor Approach for Structural Reliability
Isabelle M. Jollymore, Kyle Tousignant, and Jeffrey A. Packer

127 Impact of Bolt Pretension on Bearing Strength for All-Steel Members and Composite Members
Jia-Hau Liu and Michel Bruneau

Engineering Journal

American Institute of Steel Construction

Dedicated to the development and improvement of steel construction, through the interchange of ideas, experiences, and data.

Editorial Staff

Editor	Margaret A. Matthew, PE
Managing Editor	Keith A. Grubb, SE, PE
Research Editor	Judy Liu, PhD
Production Editor	Kristin Hall

Officers

Chair
Hugh J. McCaffrey

Vice Chair
Glenn R. Tabolt

Secretary/Legal Counsel
Edward Seglias

President
Charles J. Carter, SE, PE, PhD

Senior Vice Presidents
Scott L. Melnick
Mark W. Trimble, PE

Vice Presidents
Todd Alwood
Brandon Chavel, PE, PhD
Carly Hurd, CAE
Christopher H. Raebel, SE, PE, PhD
Brian Raff

The articles contained herein are not intended to represent official attitudes, recommendations or policies of the Institute. The Institute is not responsible for any statements made or opinions expressed by contributors to this Journal.

The opinions of the authors herein do not represent an official position of the Institute, and in every case the officially adopted publications of the Institute will control and supersede any suggestions or modifications contained in any articles herein.

The information presented herein is based on recognized engineering principles and is for general information only. While it is believed to be accurate, this information should not be applied to any specific application without competent professional examination and verification by a licensed professional engineer. Anyone making use of this information assumes all liability arising from such use.

Manuscripts are welcomed, but publication cannot be guaranteed. All manuscripts should be submitted in duplicate. Authors do not receive a remuneration. Guidelines for authors are printed on the inside back cover.

Engineering Journal (ISSN 0013-8029) is published quarterly. Published by the American Institute of Steel Construction at 130 E Randolph Street, Suite 2000, Chicago, IL 60601.

Copyright 2025 by the American Institute of Steel Construction. All rights reserved. No part of this publication may be reproduced without written permission. The AISC logo is a registered trademark of AISC.

Archives: Search at **aisc.org/ej**.
Article downloads are free for current members and are available for a nominal fee for non-members.

Numerical Study on the Buckling Behavior of Austenitic Stainless Steel Unequal-Leg Angle Columns

EDWARD J. SIPPEL and HANNAH B. BLUM

ABSTRACT

A computational-based parametric study on stainless steel unequal-leg angles with various end conditions was conducted to assess the buckling behavior and comparison to ANSI/AISC 370 provisions. Experimental work completed at the University of Wisconsin–Madison subjected hot-rolled Grade 304 austenitic stainless steel unequal-leg angles, ranging in length from 10 to 148 in., to uniform compression with fixed supports. The angles failed in flexural-torsional buckling with variable degrees of flexural and torsional deformations. This paper reports on the finite element modeling validation of the flexural-torsional buckling failures and subsequent 2,880-model parametric study. The finite element analysis utilized a simplified approach that isolated the angle column with perfect fixed-fixed boundary conditions and incorporated measured material properties, cross-section dimensions, and geometric imperfections. This method accurately simulated the appropriate nonlinear stiffness, deflection patterns, and ultimate capacities associated with the torsion-dominated buckling failures. Flexure-dominated failures of the long specimens were not as accurately predicted by this modeling; however, the assumption of continuous positive contact and a perfect bearing surface was noted to be inaccurate. Further investigation noted that accounting for imperfect bearing and plastic deformation of the base plates from previous tests captured the reduced ultimate capacity and ductility of the column, similar to what was observed in testing. Therefore, the base modeling technique was adequate to conduct a parametric study that utilizes perfect supports. The evaluation of 12 nonslender-element unequal-leg angles, considering both nominal and measured material properties supported by fixed-fixed or pinned-pinned boundary conditions, provided additional data to qualify the behavior of unequal-leg single angles. Considering the nominal stress-strain response indicated in AISC 370, flexural-torsional buckling is consistently observed as the overall failure mode with transitions from flexural buckling dominated to torsional buckling dominated behavior. Comparisons to existing AISC 370 strength provisions indicated that the direct consideration of flexural-torsional buckling was necessary to conservatively predict the capacity. However, accounting for the measured stress-strain response resulted in a substantially higher tangent stiffness before yielding compared to the nominal response, which led to a change in overall behavior. Similar flexural-torsional buckling failures were observed, but the increased stiffness reduced the impact from the onset of increased torsional buckling participation at maximum load. The reduced design capacity from considering flexural-torsional buckling was not needed to obtain a conservative result. Instead, the flexural buckling provisions alone resulted in reasonable predictions of strength for the nonslender-element cross sections. This result is not enough evidence to change ANSI/AISC 370 provisions; however, it highlights the importance in confirming the nominal stress-strain behavior of hot-rolled stainless steel angles for compression design as this assumption could alter the importance of considering flexural-torsional buckling.

Keywords: stainless steel, unequal-leg angles, flexural-torsional buckling, flexural buckling, compression member.

INTRODUCTION

The recent release of the AISC *Specification for Structural Stainless Steel Buildings*, ANSI/AISC 370, (2021), hereafter referred to as AISC 370, has provided additional opportunities to implement stainless steel members and take advantage of their corrosion resistance, thermal properties, and aesthetics among other benefits (Houska, 2014). AISC 370 provides an approved design procedure to evaluate members in compression, including nonslender-element, equal-leg single angles. Unlike carbon steel members designed according to the AISC *Specification for Structural Steel Buildings*, ANSI/AISC 360 (2022), hereafter referred to as AISC 360, the stainless steel provisions incorporate a three-stage buckling model that separates the response into full member yield, inelastic buckling, and elastic buckling. Another difference introduced to the stainless steel design procedure is the consideration of flexural-torsional buckling with single angles. This is a change from guidance provided in the first edition AISC Design Guide 27, *Structural Stainless Steel* (Baddoo, 2013), which aligned with the design provisions for carbon steel single angles that permitted excluding the direct calculation of flexural-torsional buckling because the local buckling reduction adequately reduces the flexural buckling capacity to produce a safe

---

Edward J. Sippel, Assistant Professor, Milwaukee School of Engineering, Milwaukee, Wis. Formerly, Graduate Research Assistant, University of Wisconsin–Madison. Email: sippel@msoe.edu (corresponding)

Hannah B. Blum, Alain H. Peyrot Associate Professor, University of Wisconsin–Madison, Madison, Wis. Email: hannah.blum@wisc.edu

Paper No. 2023-10R

ISSN 2997-4720

design (Galambos, 1991). There is interest in expanding the available data for unequal-leg angles subjected to uniform compression such that the new provisions can be properly assessed with regard to the capacity and the types of failure modes checked.

Material Properties

Stainless steel exhibits a nonlinear stress-strain response, as shown in Figure 1, unlike typical structural carbon steels. While carbon steels have a well-defined yield behavior, stainless steels have no definitive yield point. Stainless steel behavior is characterized by a departure from the linear elastic response at low stresses, which varies with the exact material alloy. The yield point is alternatively defined using a specified offset strain, commonly 0.2% strain as highlighted in Figure 1.

Various models (Dundu, 2018) have been considered to capture the nonlinear behavior of stainless steel, with the most popular ones being based on the modified Ramberg-Osgood model (Hill, 1944). While this model has been shown to effectively capture stresses below the yield stress, it regularly overpredicts observed stresses at higher strains as shown in Figure 2. Researchers have addressed this issue in different ways (MacDonald et al., 2000; Olsson, 2001; Mirambell and Real, 2000; Rasmussen, 2003; Gardner and Nethercot, 2004; Gardner and Ashraf, 2006; Quach et al., 2008; Hradil et al., 2013); however, one of the more common solutions is the application of a two-stage, modified Ramberg-Osgood stress-strain relationship as shown in Equation 1:

$$\varepsilon = \begin{cases} \dfrac{f}{E_0} + 0.002\left(\dfrac{f}{f_{0.2}}\right)^{n} & \text{if } f \le f_{0.2} \\[2ex] \dfrac{f - f_{0.2}}{E_{0.2}} + \varepsilon_{max}\left(\dfrac{f - f_{0.2}}{f_{max} - f_{0.2}}\right)^{n_{0.2,max}} + \dfrac{f_{0.2}}{E_{0.2}} + 0.002 & \text{otherwise} \end{cases} \tag{1}$$

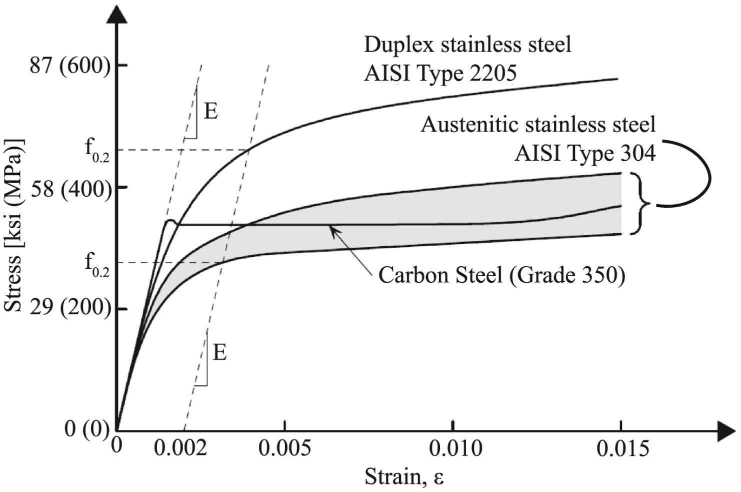

Fig. 1. Typical stress-strain curves of carbon and stainless steels (Dundu, 2018).

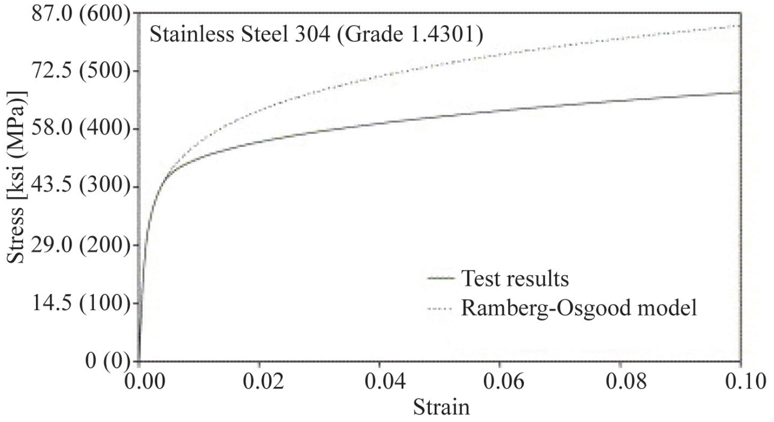

Fig. 2. Comparison of modified Ramberg-Osgood model and experimental stress-strain curves (Ashraf et al., 2006).

where ε is the current strain, f is the current stress, $f_{0.2}$ is the 0.2% offset yield stress, E_0 is the initial modulus of elasticity, n is the strain hardening exponent, $E_{0.2} = \dfrac{E_0}{1 + 0.002nE_0/f_{0.2}}$ is the tangent modulus of elasticity at $f_{0.2}$, f_{max} is the maximum reference stress, ε_{max} is the maximum reference strain, and $n_{0.2,max}$ is the Ramberg-Osgood strain-hardening coefficient for the second stage.

Compression Testing

The buckling behavior of concentrically loaded angles has been studied for a number of years. The majority of research has been conducted on carbon steel equal-leg angles. Some research has been conducted on carbon steel unequal-leg angles and stainless steel equal-leg angles. Research on stainless steel unequal-leg angles was not found in the literature search.

Stainless Steel Equal-Leg Angles

In recent years, research on stainless steel equal-leg angles subjected to uniform compression has become an active topic. Before this, Kuwamura (2003) and Sun et al. (2019) provided some of the limited relevant results. Kuwamura was primarily concerned with the local buckling behavior of thin-walled stainless steel sections. As part of that study, 12 cold-formed austenitic equal-leg angle stub columns were tested to failure with nominally fixed-fixed end conditions. Flexural-torsional buckling was observed at failure of the columns with nonslender cross sections having ultimate loads greater than the yield strength of the column (F_yA_g). As the slenderness of individual legs increased, the buckling load decreased and was found to be less than the yield strength for slender legs. Sun et al. investigated hot-rolled stainless steel equal-leg angles subjected to constrained bending where two angles were tested as a pair, clamped together at the quarter points with a spacer, to limit rotation. Of particular interest from this work, Sun et al. completed a series of stub column tests on 9.5 and 12 in. members to obtain material properties. All 10 tests were also found to fail by flexural-torsional buckling with most exceeding the nominal yield strength.

Reynolds (2013) investigated the behavior of laser-welded duplex equal-leg angles. Thirty-three specimens were subjected to concentric compression with the ends pinned for weak-axis bending, fixed for strong-axis bending, and fixed for warping. Weak-axis flexural buckling was observed in 28 of the specimens, while the remaining 5 were found to exhibit flexural-torsional buckling. Considering a draft version of the first edition of the AISC Design Guide 27 (Baddoo, 2013), Reynolds found that the evaluation of flexural-torsional buckling design provisions, which existed in that draft, resulted in overly conservative results, while the accuracy of flexural buckling provisions varied among different specifications. A parametric study using shell finite elements indicated the flexural-torsional buckling became increasingly critical as the cross-section slenderness increased.

Liang et al. (2019) subjected 16 fixed-ended hot-rolled austenitic stainless steel equal-leg angles to concentric compression. All members depicted flexural-torsional buckling, but longer members also incorporated an interaction with flexural buckling. Liang et al. used the experimental results to develop a complementary finite element parametric study. When comparing these results with existing design provisions, flexural-torsional buckling was conservatively predicted. They also compared the results to proposed carbon steel direct strength method provisions for flexural-torsional buckling, which resulted in improved accuracy in terms of capacity. However, approximately half of the estimated direct strength method capacities were unconservative due to not accounting for the softer material response of stainless steel relative to carbon steel. A comparable study completed by Sirqueira et al. (2020) with 18 fixed-ended, hot-rolled, austenitic stainless steel equal-leg angles obtained similar conclusions. Additional numerical work with slender-element equal-leg angles noted that observed local buckling did not correspond with the behavior indicated by the Eurocode 3 provisions (Sarquis et al., 2020).

An extended series of compression tests were completed at the University of Belgrade, including hot-rolled (Filipović et al., 2021a), laser welded (Filipović et al., 2021b), and cold-formed (Dobrić et al., 2020) stainless steel equal-leg angles. All columns were fixed for strong-axis bending and torsion while pinned for weak-axis bending. The measured yield strength was consistently found to exceed the specified nominal value with the largest variation of 55% noted for the hot-rolled sections. The shorter stub column tests were found to fail in flexural-torsional buckling. The slender-element cold-formed section exhibited failure below the yield stress, while the laser welded and hot-rolled specimens exceeded the yield stress. Flexural-torsional buckling was observed throughout the shorter specimens with a gradual transition to flexural buckling behavior at long lengths. The test results indicated that existing design procedures in the Eurocode and the first edition AISC Design Guide 27 (Baddoo, 2013) resulted in safe, but inaccurate strength predictions. For the AISC calculations, only flexural buckling was considered as recommended in the first edition of the AISC Design Guide 27. Another test series of 24 hot-rolled, stainless steel equal-leg angles, including short and long member lengths studied by Zhang, Y., et al. (2020; 2021), observed similar global buckling behaviors and inaccurate strength predictions by the Eurocode and AISC Design Guide 27 design procedures.

Table 1. Flexural Buckling Coefficients for Stainless Steel (AISC, 2021)

Member Type	Curve	α	β_0	β_1	β_2
Rolled or built-up I-shaped sections buckling about the minor axis, and other sections not specified in this table	A	0.56	0.759	0.409	0.690
Rolled or built-up I-shaped sections buckling about the major axis, welded box sections, and round HSS	B	0.58	0.891	0.455	0.820
Rectangular HSS	C	0.69	1.195	0.501	0.820

Behzadi-Sofiani et al. (2021) completed an experimental and numerical study on fixed-ended stainless steel equal-leg angle columns. The flexural buckling controlled capacities were reasonably estimated using existing Eurocode design provisions, but flexural-torsional buckling controlled design predictions varied significantly ranging from near capacity to less than 20% of the expected strength. They noted that current Eurocode flexural-torsional buckling design procedures effectively double counted the reduction in strength from flexural-torsional buckling and local buckling as the two phenomena are mechanically equivalent in equal-leg single angles.

Unequal-Leg Angles

Despite the growing database for equal-leg angles, only minimal published research on unequal-leg angles subjected to uniform compression was located, and none for stainless steel members. Early work by Liu and Chantel (2011) considered 26 carbon steel unequal-leg angles subjected to compression with varying amounts of eccentricity. All five concentrically loaded angles failed primarily in flexural buckling at less than 40% of the yield stress. Dinis et al. (2015) evaluated four carbon steel unequal-leg angles to investigate the elastic flexural-torsional response in asymmetric sections. Experimental results and subsequent modeling were in agreement with the standard theoretical elastic buckling capacity used in the AISC *Specifications*. Ojalvo (2011) summarized the results of three fixed-end aluminum unequal-leg angles tests (Liao, 1982; Wu, 1982). The inelastic response of the fixed-ended columns captured additional post-critical strength excluded in standard elastic buckling assumptions. Recently, Y. Zhang and colleagues (2020, 2021) tested a combined 22 pinned-end aluminum unequal-leg angle columns. Experimental results consistently exhibited flexural-torsional buckling. The response was dominated by torsional behavior at short lengths with a gradual transition to significant flexural behavior at long lengths.

Design Provisions

In the late 1800s, Engesser demonstrated how inelastic buckling capacity could be determined by considering the tangential stiffness of a perfectly straight column, which was in agreement with experimental results (Timoshenko and Gere, 1961). This approach still serves as the basis behind current methods included in AISC 370 (2021). These provisions capture this phenomenon by converting the elastic buckling stress, F_e, into the critical buckling stress, F_{cr}, using a three-stage response. Similar to carbon steel, low compressive stresses correspond to an elastic buckling behavior with a minor reduction for member imperfections. As the stress increases, the response transitions to include inelastic buckling behavior. Unlike carbon steel, designs with stainless steel allow for full yield in compression at short lengths. Based on existing research, Meza et al. (2021) developed the current flexural design provisions for compression members, given by Equation 2:

$$F_{cr} = \begin{cases} F_y & \text{if } \dfrac{F_y}{F_e} \le \left(\dfrac{\beta_0}{\pi}\right)^2 \\ 1.2\left[\beta_1^{\left(\frac{F_y}{F_e}\right)^{\alpha}}\right]F_y & \text{if } \left(\dfrac{\beta_0}{\pi}\right)^2 < \dfrac{F_y}{F_e} \le 3.20 \\ \beta_2 F_e & \text{if } \dfrac{F_y}{F_e} > 3.20 \end{cases} \tag{2}$$

where α, β_0, β_1, β_2 are flexural buckling coefficients that vary based on the member type as shown in Table 1. Multiple column curves have been adopted to capture the increased strength associated with different cross sections buckling.

When applying AISC 370, single-angle compression member design is currently limited to equal-leg, nonslender cross sections. Despite the buckling coefficients being based on flexural buckling, the design procedures require the determination of the minimum controlling elastic global buckling behavior, including flexural-torsional buckling, which is then adjusted using Equation 2 with Curve A coefficients from Table 1. The singly symmetric geometry of equal-leg angles normally exhibits flexural buckling about the weak axis at longer lengths with a transition to flexural-torsional buckling at short lengths. This transition is typically associated with a significant drop in buckling capacity compared to the flexural buckling response. While

Table 2. Experimental Mechanical Properties

Specimen	E_0 (ksi)	f_y (ksi)	$f_{1.0}$ (ksi)	n	$n_{0.2,1.0}$
C-1-A	28750	52.6	64.7	5.35	2.57
C-2-B	27780	38.9	50.9	4.23	2.20
C-3-C	28350	43.4	46.2	10.45	1.51
C-4-A	25760	54.9	63.5	8.78	2.12
C-5-A	27800	54.5	62.3	9.13	2.55
C-6-B	27760	46.1	53.7	8.83	2.29
Average	27700	48.4	56.9	7.80	2.21

not covered by the AISC 370, an asymmetric unequal-leg angle would behave similarly, in that flexural behavior dominates at long lengths, which then transitions to torsional dominated behavior at short lengths. However, the controlling response is always a flexural-torsional buckling, which means there is consistently an additional reduction applied to the buckling capacity.

An interesting phenomenon in single angles is the equivalency of flexural-torsional buckling and local buckling, both in terms of the deformed shape and buckling capacity for equal-leg angles (Rasmussen, 2005; Behzadi-Sofiani et al., 2021). As a result, existing design provisions run the risk of double counting the same effect when evaluating flexural-torsional buckling and local buckling in single angles. This issue is addressed in AISC 360 for carbon steel members (AISC, 2022) by not requiring the consideration of flexural-torsional buckling in compression member design for most single angles, except if they are very slender cross sections. Galambos (1991) demonstrated that carbon steel single angles, both equal-leg and unequal-leg cross sections, could safely be designed using the flexural buckling capacity reduced for local buckling concerns. This provision was carried forward to the first edition AISC Design Guide 27 (Baddoo, 2013) as it was modeled after AISC 360 with additional reductions for the nonlinear behavior of stainless steel. However, that exception was not incorporated into the current AISC 370 or second edition AISC Design Guide 27 (Baddoo and Meza, 2022).

EXPERIMENTAL DATA

This computational study utilized the hot-rolled stainless steel unequal-leg angle compression testing program completed at the University of Wisconsin-Madison (Laracuente et al., 2022; Laracuente, 2022; Laracuente et al., 2023). As part of the preliminary investigation, the stress-strain behavior of the Gr. 304 stainless steel angles was measured via six tensile coupon tests. The coupons, C, were labeled with the overall test numeric identifier and a second letter based on the position around the cross section as illustrated in Figure 3. Table 2 summarizes the best fit of the experimental results using a two-stage modified Ramberg-Osgood model using a 1% maximum strain as reference point in line with Arrayago et al. (2015).

The main experimental series evaluated 18 hot-rolled stainless steel L3×2×¼ columns, which included three nominally identical specimens, each at six different lengths. Each specimen, S, was given a unique name that identifies the nominal length in inches and a numeric identifier. Prior to testing, the dimensions of the angles were measured by hand. Table 3 summarizes the measured dimensions, where L is the length of the specimen; b and h are the width and height of the section, respectively; and t_b and t_h are the corresponding leg thicknesses as depicted in Figure 4. The imperfections along the length of the specimen were measured using noncontact laser methods (Laracuente et al. 2022; Sippel, 2022) with the maximum imperfections

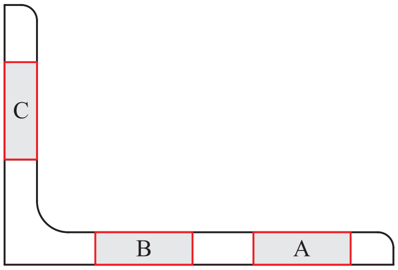

Fig. 3. Coupon position around cross section.

Table 3. Measured Geometric Properties of Test Specimens

Specimen	*L* (in.)	*b* (in.)	*h* (in.)	t_b (in.)	t_h (in.)	Area (in.^{2})
S10-1	10	2.049	2.979	0.257	0.266	1.251
S10-2	10	2.055	2.977	0.258	0.243	1.191
S10-3	10	2.052	2.966	0.258	0.244	1.192
S20-1	20	2.030	2.981	0.253	0.253	1.203
S20-2	20	2.063	2.958	0.258	0.241	1.182
S20-3	20	2.063	2.965	0.259	0.243	1.190
S36-1	36	2.019	2.985	0.251	0.253	1.198
S36-2	36	2.014	2.991	0.251	0.253	1.198
S36-3	36	2.076	2.964	0.259	0.241	1.190
S72-1	72	2.005	2.987	0.250	0.250	1.185
S72-2	72	2.010	2.985	0.251	0.249	1.184
S72-3	72	2.034	2.980	0.253	0.256	1.214
S100-1	100	2.057	2.957	0.258	0.252	1.210
S100-2	100	2.067	2.933	0.258	0.252	1.208
S100-3	100	2.063	2.939	0.258	0.253	1.209
S148-1	$147\frac{15}{16}$	2.006	2.999	0.249	0.254	1.199
S148-2	$147\frac{15}{16}$	2.033	2.972	0.256	0.244	1.182
S148-3	$147\frac{15}{16}$	2.020	2.989	0.255	0.254	1.210

summarized in Table 4. As illustrated in Figure 4, dx and dy are the lateral imperfection in the x- and y-direction at the heel of the angle, and $d\theta$ is the rotation of the cross section.

Compression Tests

The full-scale compression tests were conducted using a Southwark Emery Testing Machine with a 1-million-pound capacity. As illustrated in Figure 5, the tests were completed with nominal fixed-fixed boundary conditions using reusable ASTM A572/A572M Gr. 50 (2021) carbon-steel top and bottom bearing plates. Before starting the test series, the 10×10×1¼ bottom plate, the 14×14×1¼ top plate, and the end of each angle were milled flat to provide full end bearing. Three ¾-in.-thick, ASTM A36/A36M (2019) clamping brackets were then used to laterally position the angle and provide lateral restraint at the base of the member since there was no positive connection to the bearing plates. All test specimens were observed to exhibit flexural-torsional buckling at the failure loads summarized in Table 5. The buckling response was dominated by torsional deformations for short specimens and transitioned to flexural bending for longer specimens.

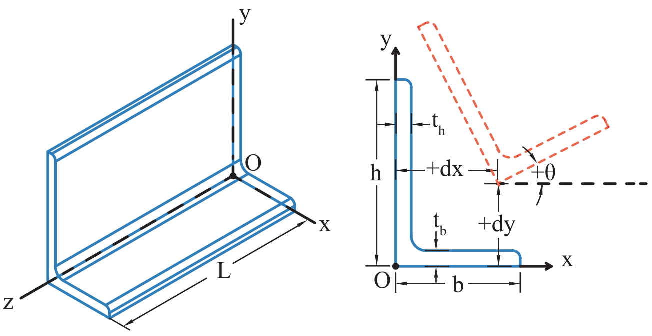

Fig. 4. Unequal-leg angle conventions for dimensions, axes, and displacements.

COMPUTATIONAL STUDY

Modeling Methodology

Using the experimental series just discussed, the modeling approach for an unequal-leg angle was validated before conducting a finite element-based parametric study. The reference L3×2×¼ specimens were evaluated using finite element analysis (FEA) via Abaqus (Dassault Systems, 2015b). The unequal-leg cross sections were modeled as S4R shell elements, which has a four-node linear formulation with reduced integration, hour-glass control, and a general formulation that includes both thick and thin shell behavior (Dassault Systems, 2015a). This approach aligned with previous works (Reynolds, 2013; Liang et al., 2019;

Table 4. Maximum Measured Imperfections

Specimen	Measured			Normalized		
	dx (in.)	dy (in.)	θ (deg)	$dx/(L/1000)$	$dy/(L/1000)$	$\theta/\tan^{-1}(L/1000h)$
S10-1	−0.014	−0.007	−0.20	−1.434	−0.705	−1.05
S10-2	0.003	0.002	0.04	0.347	0.197	0.21
S10-3	0.003	0.002	N/A[1]	0.300	0.150	N/A[1]
S20-1	−0.016	−0.013	−0.22	−0.787	−0.639	−0.56
S20-2	−0.006	−0.003	0.04	−0.288	−0.160	0.09
S20-3	0.005	−0.009	0.05	0.236	−0.442	0.13
S36-1	0.018	−0.018	−0.12	0.494	−0.499	−0.17
S36-2	−0.011	−0.036	−0.18	−0.299	−1.000	−0.26
S36-3	−0.048	−0.022	−0.21	−1.339	−0.603	−0.31
S72-1	0.063	−0.064	0.26	0.873	−0.893	0.19
S72-2	−0.142	−0.134	0.15	−1.978	−1.857	0.11
S72-3	0.035	−0.037	0.10	0.483	−0.520	0.07
S100-1	0.218	0.070	−0.30	2.183	0.695	−0.16
S100-2	0.086	−0.073	−0.37	0.858	−0.732	−0.19
S100-3	−0.037	−0.126	0.35	−0.369	−1.259	0.18
S148-1	−0.070	−0.141	−0.20	−0.472	−0.955	−0.07
S148-2	0.470	0.206	−0.33	3.178	1.389	−0.12
S148-3	0.287	−0.070	−0.20	1.943	−0.474	−0.07

[1] Results from scanned data not available due to poor scan quality.

Table 5. Experimental Failure Loads for All Test Specimens

Specimen	Load (kips)	Specimen	Load (kips)	Specimen	Load (kips)
S10-1	62.1	S36-1	57.1	S100-1	19.2
S10-2	69.5	S36-2	52.7	S100-2	18.4
S10-3	68.8	S36-3	53.3	S100-3	18.0
S20-1	61.3	S72-1	30.8	S148-1	7.8
S20-2	66.8	S72-2	24.8	S148-2	5.6
S20-3	65.4	S72-3	34.4	S148-3	6.7

Sirqueira et al., 2020; Behzadi-Sofiani et al. 2021; Zhang, L., et al., 2019, 2020, 2021; Dinis et al., 2015; de Menezes et al., 2019) that have shown shell elements can be used to accurately model single angles in compression.

The unequal-leg geometry was modeled using the centerline model shown in Figure 6(b) using centered elements, which has been shown to provide similar computational results compared to solid element models (Reynolds, 2013; Dinis et al., 2015). Based on a refinement study, the member was modeled using a square mesh with 16 elements across the short flange with equivalent sized elements on the long flange as indicated in Figure 6(c). The end boundary

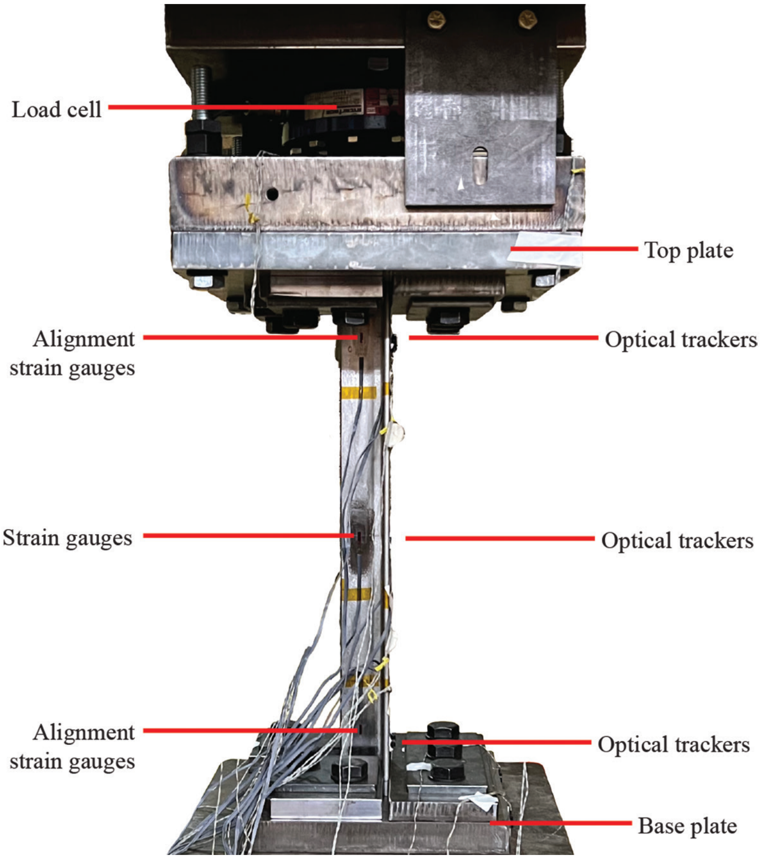

Fig. 5. Typical compression testing setup.

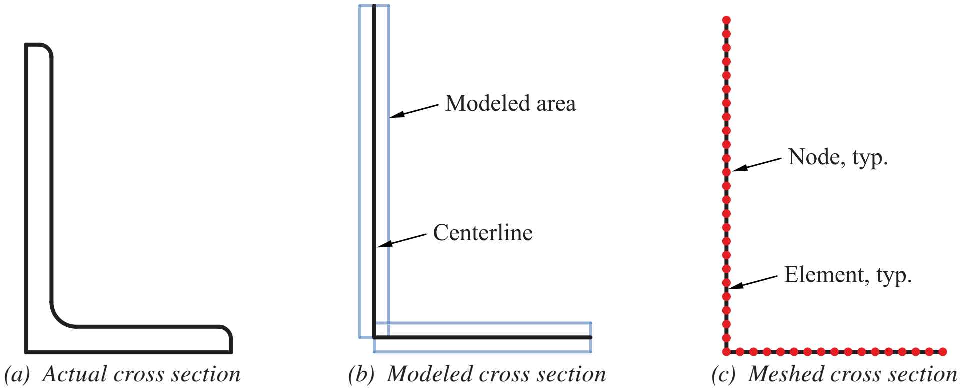

(a) Actual cross section *(b) Modeled cross section* *(c) Meshed cross section*

Fig. 6. Typical model of unequal-leg cross section.

Table 6. Imperfection Distributions Considered in the Validation Study

Label	Translations		Rotations	
	Smooth	Sine	Smooth	Sine
IV-1	×			
IV-2	×		×	
IV-3	×			×
IV-4		×		×

condition for the unequal-leg angle models was applied using a single reference node at the angle centroid that was connected to all nodes across the end of the angle through a rigid tie constraint. As a result, the angle ends were always fully constrained against warping, and the flexural boundary condition could be readily defined as fixed or pinned in the geometric orientations. For the validation analysis, the end of the member was fixed for bending about both axes.

The material model for this study was selected from the experimental results listed in Table 2. Evaluating the axial response of the 10 in. columns, which correspond to typical stub column test geometry, stress-strain curve 5 (C-5-A) from Table 2 was selected as it best captured the ultimate capacity, initial modulus of elasticity, and intermediate stiffness as depicted in Figure 7. Due to the variable stress-strain behavior captured within each leg in the initial coupon tests, this comparison included the average strain result at the middle of each leg to confirm that the selected model was appropriate for both legs. This behavior was implemented in the finite element analysis using an elastic-plastic model that ignored the initial $(0.5\text{ ksi})/E_0$ plastic strain to minimize the concerns of underestimating capacity noted by Schafer et al. (2010).

Four variations of the measured imperfections were evaluated, as summarized in Table 6, where IV represents imperfection variation, to investigate the effect of the imperfection shape. Rotation and translations were treated as distributions that could be separately applied to determine the importance of including the rotation imperfection that is occasionally excluded in parametric studies. Additionally, the imperfection profile was applied as a "Smooth" or "Sine" profile as shown in Figure 8. The Sine profile applied a traditional half-sine curve profile based on the maximum imperfection value noted in Table 4. The Smooth profile accounted for the variable imperfection along the length of the specimen. The profile was interpolated from the measured profile to fit the underlying finite element mesh. This process included a smoothing filter to eliminate localized kinks that created unrealistic stress concentrations.

Validation Results

The results of the validation study are provided in Table 7. The computational models matched well with the experimental results for all specimens 72 in. and shorter. The finite element analysis was able to replicate the torsional buckling dominant response in short columns as shown in Figure 9. The inclusion of additional flexural movement as the column length increased was also captured as depicted in Figure 10. However, as the buckling transitioned to a

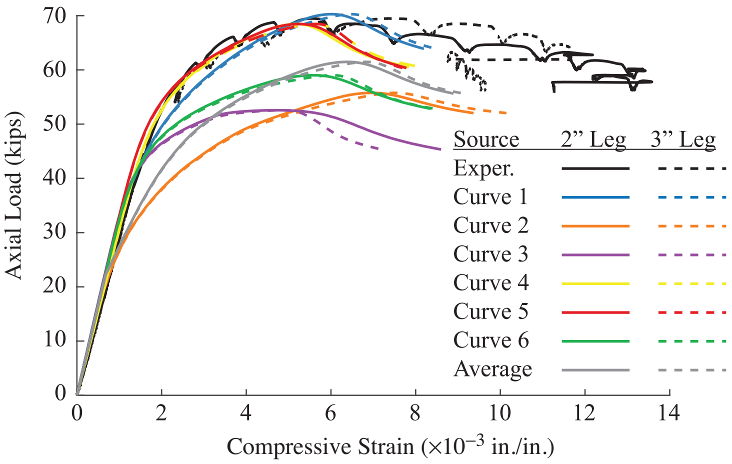

Fig. 7. Applied axial load-strain response of S10-2 column.

Table 7. Ultimate Failure Loads for Validation Modeling with Variable Imperfections

	Test	Ultimate Load (kips) with			
Specimen	**(kips)**	**IV-1**	**IV-2**	**IV-3**	**IV-4**
S10-1	62.1	70.3	69.5	69.5	69.6
S10-2	69.5	68.9	68.4	68.4	68.4
S10-3	68.8	69.1	69.1	69.1	69.1
S20-1	61.3	62.0	61.4	61.5	61.6
S20-2	66.8	63.4	63.5	63.6	63.3
S20-3	65.4	63.5	63.5	63.3	63.0
S36-1	57.1	53.0	53.1	53.2	53.7
S36-2	52.7	54.4	54.0	53.9	52.9
S36-3	53.3	51.7	51.3	51.4	51.3
S72-1	30.8	33.2	33.0	32.9	33.4
S72-2	24.8	28.3	28.3	28.4	28.4
S72-3	34.4	35.1	35.1	35.0	36.7
S100-1	19.2	19.1	19.1	19.1	19.2
S100-2	18.4	22.9	22.9	23.0	22.9
S100-3	18.0	22.4	22.6	22.7	22.2
S148-1	7.8	10.4	10.4	10.4	10.2
S148-2	5.6	9.1	9.1	9.1	9.0
S148-3	6.7	9.9	9.9	9.9	9.9
Full series	**Mean**	1.12	1.12	1.12	1.12
	CoV	0.17	0.17	0.17	0.17
0 in.–72 in. series	**Mean**	1.02	1.02	1.02	1.02
	CoV	0.06	0.06	0.07	0.07

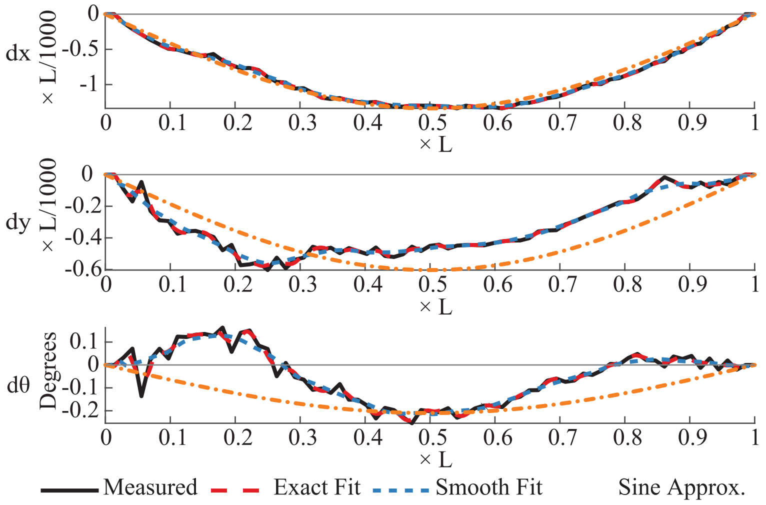

Fig. 8. Initial imperfections as adjusted for finite element modeling for S36-3.

primarily flexural buckling response at long lengths, significant variations between the modeled and actual response were noted. The FEA captured the overall behavior, but at higher magnitudes than the experimental results, as shown in Figure 11.

While investigating the deviation noted in the FEA results for longer specimens, it was observed that the larger flexural deformation of the buckled column combined with the fixed boundary condition caused tension to develop at the end of the specimens in the finite element analysis. While reasonable, this behavior was not possible in the existing test setup because bearing would be lost if tensile flexural stresses exceeded the axial compression. Exploratory work to directly account for contact at the base plate confirmed that uplift did occur at buckling for the longer specimens due to the lack of a positive connection to the bearing plate. It was found that the angle lifted at the heel, which increased the bearing stress at the tip, causing more localized yielding of the angle as shown in Figure 12. The loss of bearing was not visually confirmed during testing due to the lateral clamping plates, but the direction the angle moved while buckling corresponded with the tensile stresses at the heel from bending. The FEA results with contact exhibited a reduced ultimate capacity and less post-buckling

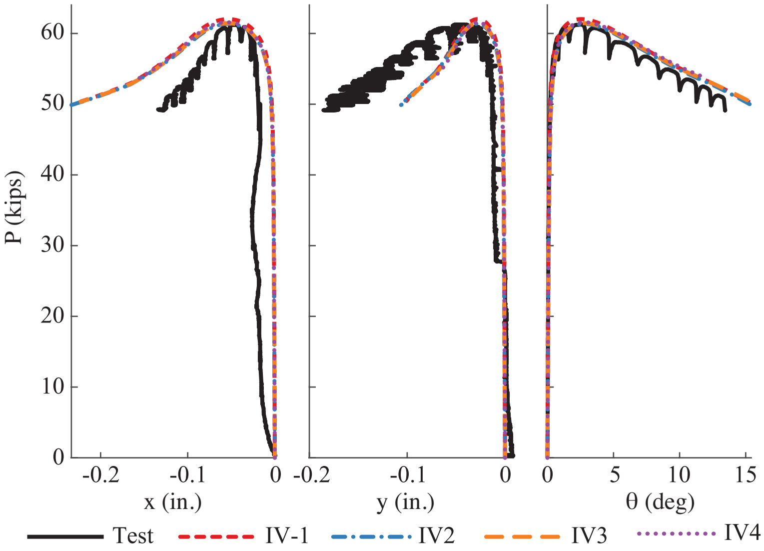

Fig. 9. Torsion dominated buckling displacement of S20-1.

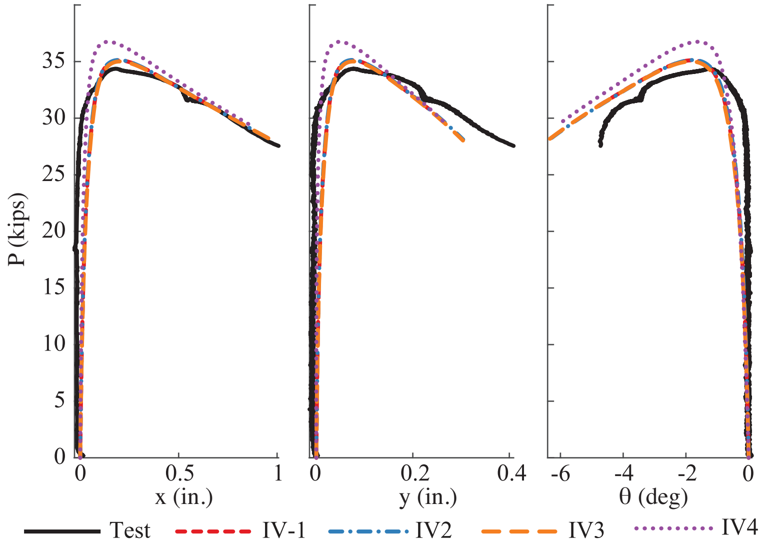

Fig. 10. Intermediate flexural-torsional buckling displacement of S72-3.

ductility from the perfect support, but not enough to match the experimental results.

Upon closer inspection of the base plates after the compression tests, it was noted that there was permanent deformation as shown in Figure 13. While it was not anticipated that the base plates would plastically deform under ultimate loads based on the nominal stainless steel yield strength, the actual experimental yield strength of the angles was measured as 60% greater than nominal (Laracuente et al., 2022), which caused small impressions on the base plates under the tips of each angle leg. While the high stresses of the short columns affected the entire bearing area, the primary concern was the tips of each leg where roughly the end 0.6 in. of each leg was clearly deformed, varying approximately linearly to a max impression of 0.02 in. at the tip.

Due to these observations, the finite element model was refined to account for the imperfect base plate. The base plate was modeled as a solid body with a perfectly elastic-perfectly plastic response accounting for the nominal 50 ksi yield strength. The angle and base plate were modeled with contact and allowed to separate under tension. Initial investigations utilized a perfect rectangular cube for the base plate geometry, but later variations considered existing initial imperfections by utilizing a trapezoidal profile as shown in Figure 14. Multiple profiles were considered to address the limitations in defining the exact geometry of the indentations. This modeling incorporating contact, the imperfect bearing surface, and deformation of the base plate resulted in only minor changes for shorter columns; however, the majority of 100 and 148 in. models captured a significantly reduced capacity, as shown in

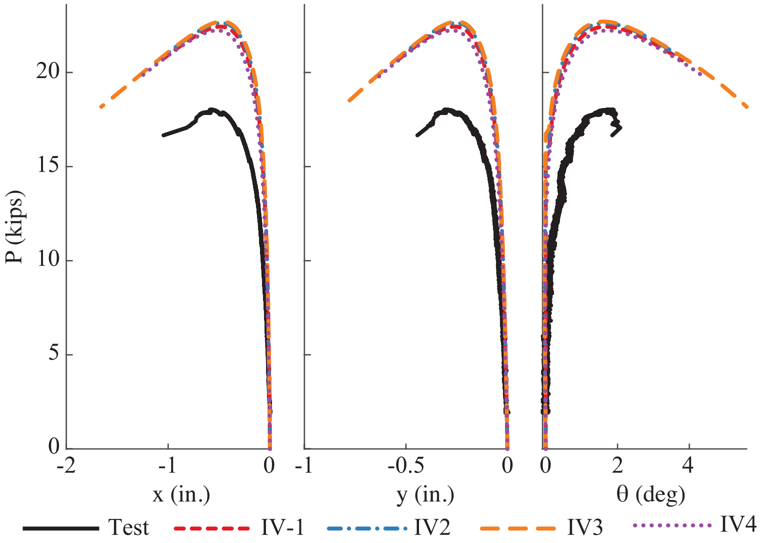

Fig. 11. Flexure dominated buckling displacement of S100-3.

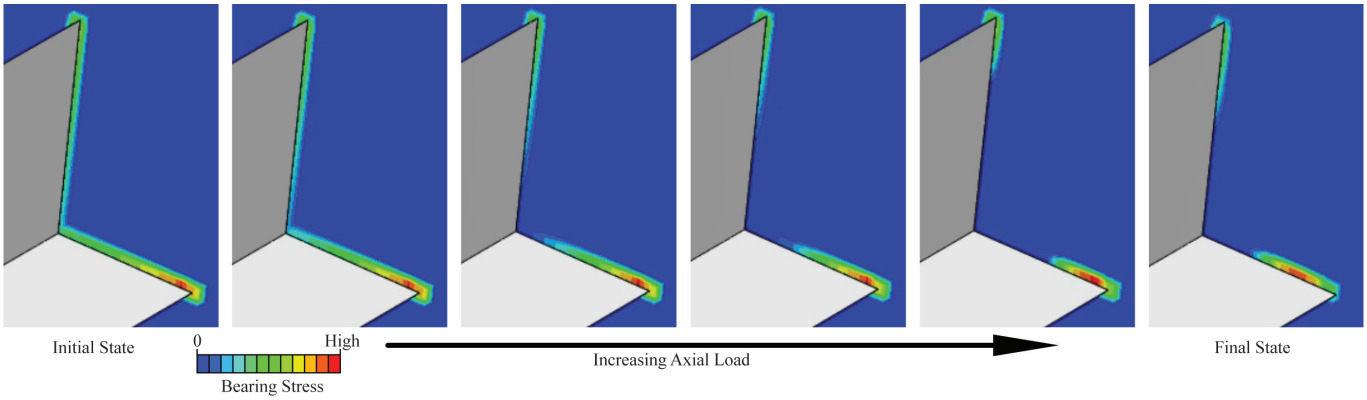

Fig. 12. Typical changes in bearing stress when allowing for uplift of angle specimen at support.

Figure 15; less overall deflection at ultimate capacity; and partial bearing, which occurred with both the perfect cube or modified deformed base plate geometry. These results indicated that the longer-length specimens were sensitive to the bearing support condition and, therefore, explained the discrepancy between the experiments and modeling results. The validation study demonstrated that the modeling approach was capable of depicting the behavior of stainless steel unequal-leg angles with perfect boundary conditions, and thus was acceptable to implement in a FEA-based parametric study.

PARAMETRIC STUDY

A parametric study was conducted to expand the available data for unequal-leg single angles. In total, 12 representative nonslender, unequal-leg angle cross sections, listed in Table 8, were selected to cover typical h/t, b/t, and h/b ratios of the 50 nonslender-element cross sections that are currently available for purchase or listed in the AISC *Steel Construction Manual* (AISC, 2017).

Each cross section was evaluated with nominal dimensions; nominal imperfections; and an effective slenderness ratio, L_e/r_z, ranging from 5 to 200. The nominal imperfections were half-sine wave imperfections with a magnitude of L/1000 in the negative x- and y-directions and a rotation of $-\tan^{-1} L/(1000h)$, but limited to 1°. All cross sections were modeled for both a fixed-fixed, $L_e = 0.5L$, and pinned-pinned, $L_e = 1.0L$, boundary condition. The angles were then modeled with either the measured material properties, matching the validation study, or nominal material properties for 304 or 304L based on AISC 370 nominal values (2021) listed in Table 9. These parameters created 960 models that were evaluated for each of the three material models, resulting in a total of 2,880 models. In these models, flexural-torsional buckling was consistently observed. Similar to the experimental results, flexural deformations were dominant at high slenderness ratios, and as the slenderness ratio decreased, torsional deformations became more dominant. Due to the selected imperfection, a few geometries displayed a deviation from the typical flexural buckling response as shown in Figure 16; however, this consistently

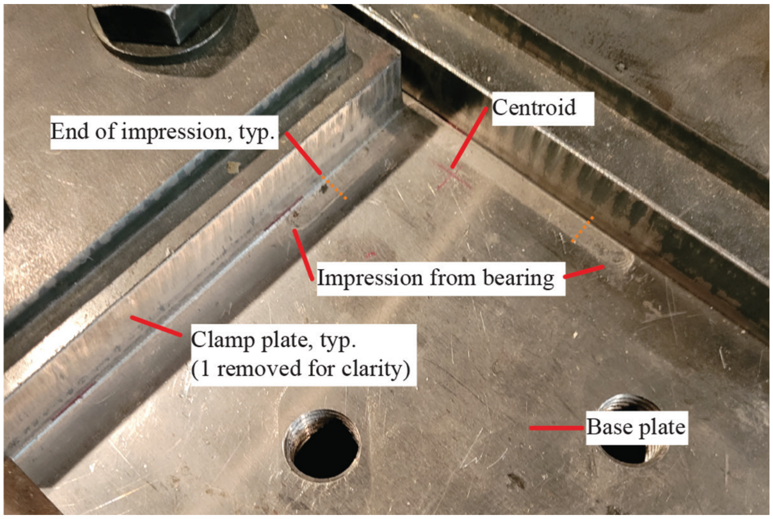

Fig. 13. Base plate after final compression test series.

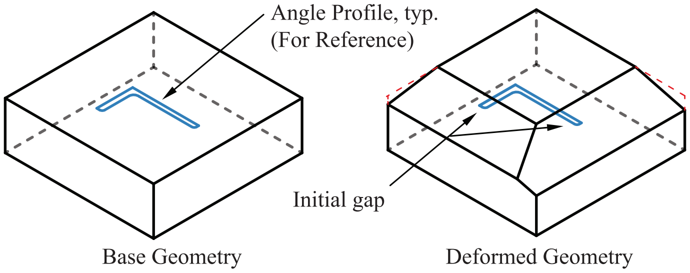

Fig. 14. Base plate geometry (not to scale).

Table 8. Angles in Parametric Study

Section	h/t	b/t	h/b
L1½×1¼×⅛	12.0	10.0	1.20
L2×1×¼	8.0	4.0	2.00
L2×1½×¼	8.0	6.0	1.33
L3×1½×¼	12.0	6.0	2.00
L3×2×¼	12.0	8.0	1.50
L3×2×⅜	8.0	5.3	1.50
L4×3×⅜	10.7	8.0	1.33
L4×3×½	8.0	6.0	1.33
L5×3×½	10.0	6.0	1.67
L6×3×½	12.0	6.0	2.00
L6×4×½	12.0	8.0	1.50
L6×5×½	12.0	10.0	1.20

Table 9. Nominal Material Properties

Grade	E (ksi)	f_y (ksi)	f_u (ksi)	n	m
304	28000	30	75	7	2.12
304L	28000	25	70	7	2

corresponded with an increase in capacity relative to the design flexural buckling curve, not the decrease typically associated with including flexural-torsional buckling.

The initial parametric study comparison, shown in Figures 16 and 17, considered all three AISC 370 flexural buckling curves as identified previously in Equation 2 and Table 1. If unequal-leg angles were covered by AISC 370, the section would be evaluated with Curve A values. The other alternatives were included to investigate whether the capacity increase associated with Curves B or C could be considered for unequal-leg angles as the section has not been thoroughly investigated.

DISCUSSION

As shown in Figure 17 [see Sippel (2022) for plots of each angle individually], a consistent result of the parametric study was that neither Curve B nor Curve C (refer to Table 1) were conservative estimates of strength for the buckling response. Therefore, the possible increase in

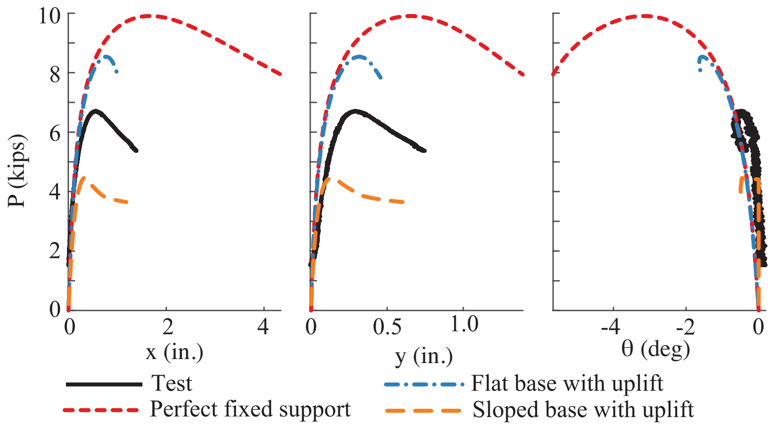

Fig. 15. Effect of changing support on buckling behavior of S148-3.

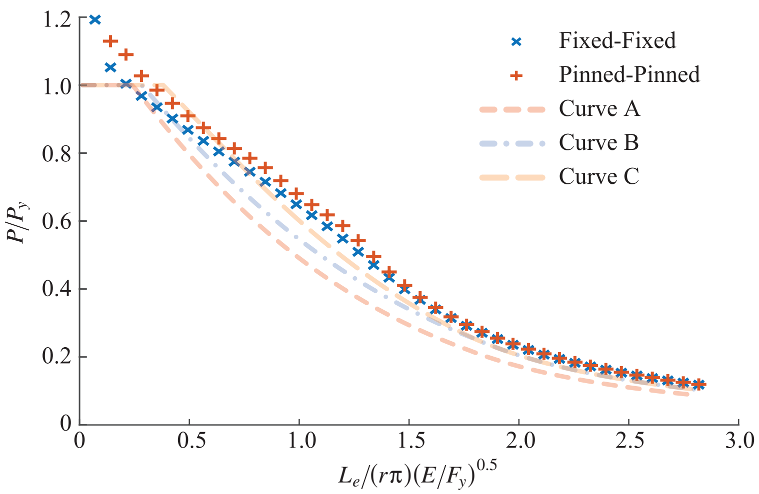

Fig. 16. Buckling behavior of L6×4×½ with measured material properties versus AISC 370 buckling curves using measured yield strength.

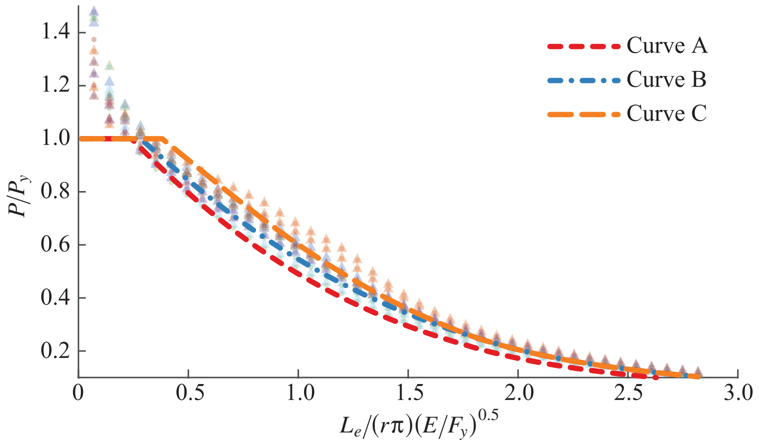

(a) Measured material properties

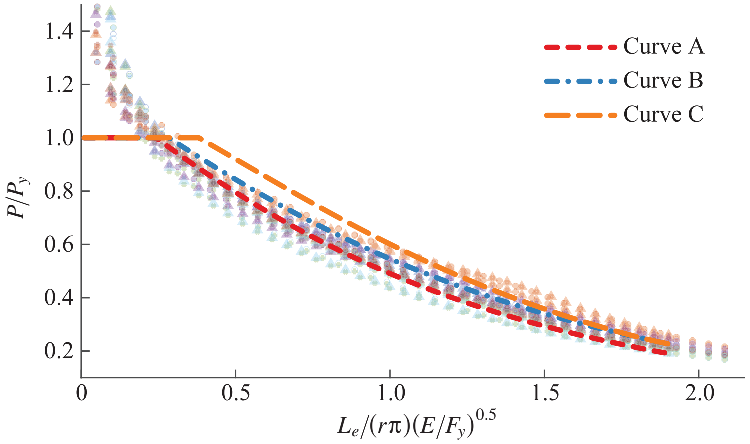

(b) Nominal material properties

Fig. 17. Buckling behavior with different material properties versus AISC 370 buckling curves using corresponding yield strength. All sizes from Table 8 included.

capacity associated with these curves was deemed unlikely, and the remainder of this study focused on comparisons to buckling capacities calculated using Curve A, the applicable parameters for single equal-leg angles. The parametric study showed different behavior depending on the material properties considered. The FEA results with measured material properties were found to be normally greater than Curve A [Figure 17(a)], while a number of FEA results with nominal material properties were lower than Curve A [Figure 17(b)]. By comparing the effective stiffness included in each model in Figure 18, there is a distinct variation between the nominal assumed material behavior, AISC 370-304 and AISC 370-304L, and the measured material behavior, Measured 304. The increased strain-hardening coefficient, n, from the measured material properties in this study, which agrees with previous research on hot-rolled sections (Behzadi-Sofiani et al., 2021; Liang et al., 2019; de Menezes et al., 2019; Sun et al., 2019), caused a stiffer material response.

This dissimilarity of results within the parametric study between FEA with measured and nominal material properties is further highlighted when comparing the simulated FEA column capacity, P_{SIM}, to the compression capacity from AISC 370 design provisions with the corresponding yield strength and considering flexural buckling, P_{FB}, or flexural-torsional buckling, P_{FTB}—that is, Figure 19 normalizes the FEA results from nominal material properties with buckling capacities based on the nominal yield strength, and Figure 20 normalizes the FEA results from measured material properties with buckling capacities calculated using the measured yield strength. For the nominal material properties with results summarized in Figure 19, the flexural buckling capacity alone was observed to underestimate the capacity of multiple sections at shorter lengths [Figure 19(b)]. Including flexural-torsional buckling effects caused the buckling capacity to be reduced for all cross sections, which included a maximum change between 5% and 24%. As shown in Figure 19(a), this change resulted in a conservative estimate in all cross sections except for the pinned L2×1×¼ and L5×3×½ columns. This contrasts with the measured material property results, Figure 20, that indicate that flexural buckling alone was an adequate predictor of strength [Figure 20(b)]. Note that the unconservative results using the flexural buckling prediction would be eliminated in most instances, except for a narrower range of the same pinned L2×1×¼ and L5×3×½ columns if local buckling was considered, which is shown in Figure 20(c). The measured yield strength would reclassify some cross sections as slender.

The varied results of the parametric study highlighted the importance of correctly defining the material properties and stress-strain response for the advanced FEA. With carbon steel sections, the majority of steel grades used for structural design exhibit a consistent material behavior that is readily simplified to an approximate elastic-plastic response. Despite a simple, consistent material model, multiple compression design curves have been developed that vary with the cross-section shape being analyzed (Ziemian, 2010). This issue is complicated for stainless steel members because the variability of the nonlinear constitutive relationship adds an additional dimension. The nominal stress-strain relationship has experimental backing that it is appropriate for the baseline behavior of 304/304L stainless steel in a very broad range of applications. However, additional research, including the testing related to this study (Laracuente et al., 2022, 2023), has regularly noted

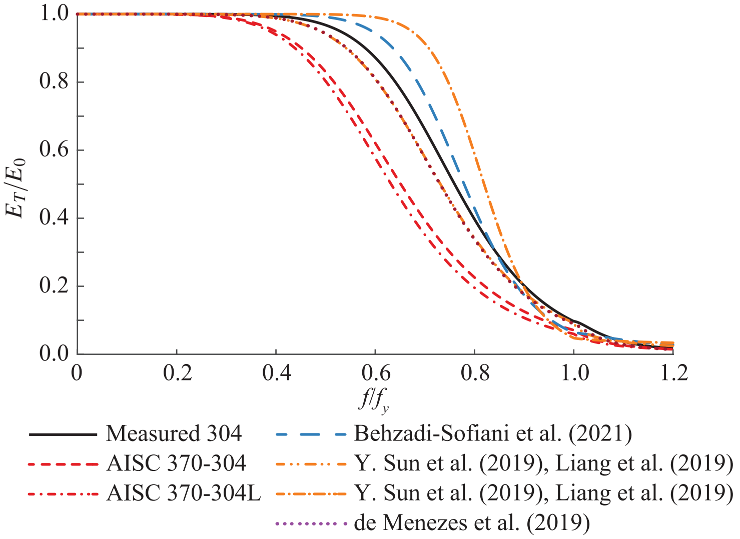

Fig. 18. Effective modulus of elasticity within material models.

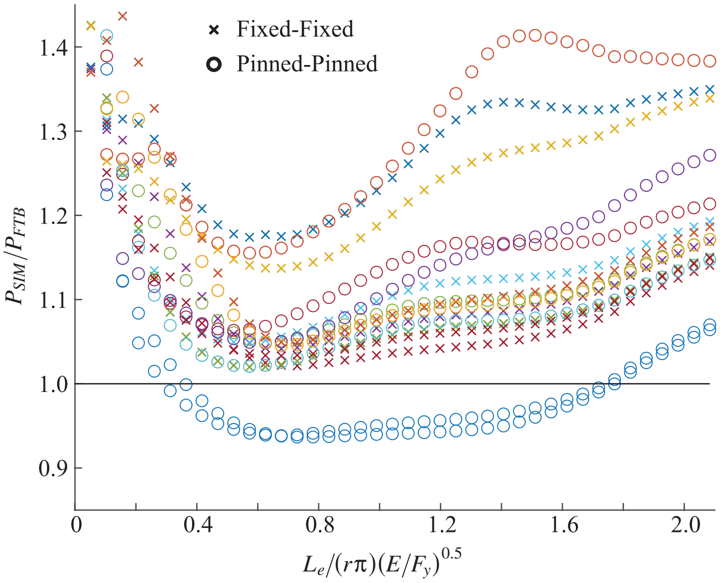

(a) Flexural-torsional buckling design provisions

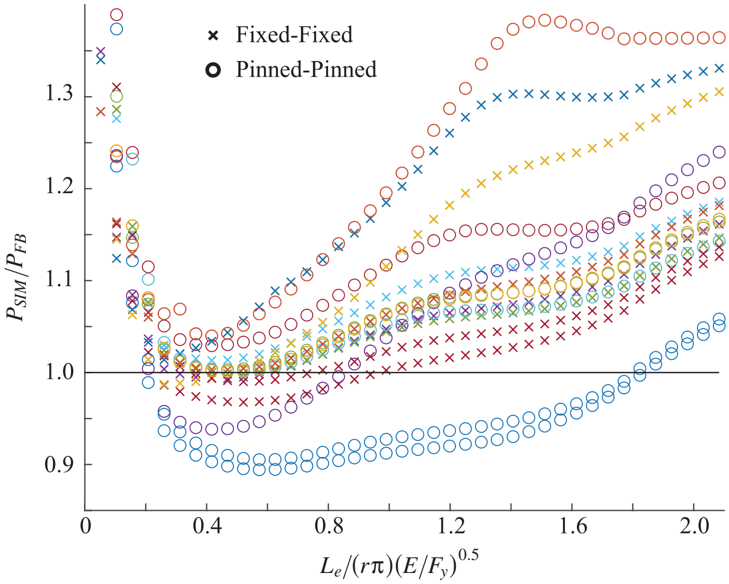

(b) Flexural buckling provisions only

Fig. 19. FEA capacity versus design provision strength calculations with nominal material properties. All sizes from Table 8 included.

significant increases in strength and stiffness when investigating structural stainless steel sections as highlighted in Figure 18. As a result, the three design curves in AISC 370 are attempting to balance the impact of different geometries, including the variable cross sections and typical imperfections as had been done with carbon steel, as well a realistic, average response of typical stainless steel members.

Based on the results of this study, if the nominal AISC material properties are an accurate depiction of a conservative stress-strain relationship and corresponding tangent modulus of elasticity, the design provisions need to include flexural-torsional buckling provisions to determine conservative predictions of capacity in compression. However, if the nominal response is underestimating the tangent modulus of elasticity before yield for typical structural stainless steel sections as observed with the experimental data, the same procedure could result in excessively conservative predictions. Along those lines, an expanded parametric study including slender cross sections and the nominal stress-strain curve would allow for a fundamental understanding of how existing buckling provisions align with the behavior of unequal-leg single angles, which would provide a worst-case design envelope to incorporate them into the specification. Yet, additional investigation into the appropriateness of the nominal stress-strain curve specified in

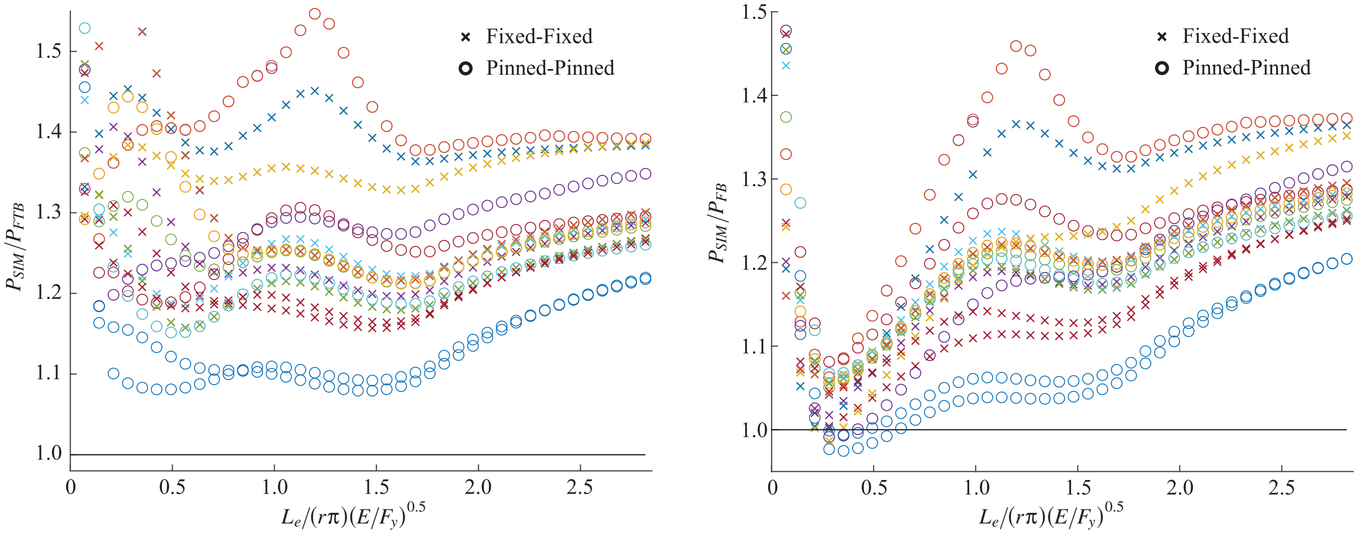

(a) *Flexural-torsional buckling design provisions*

(b) *Flexural buckling provisions only*

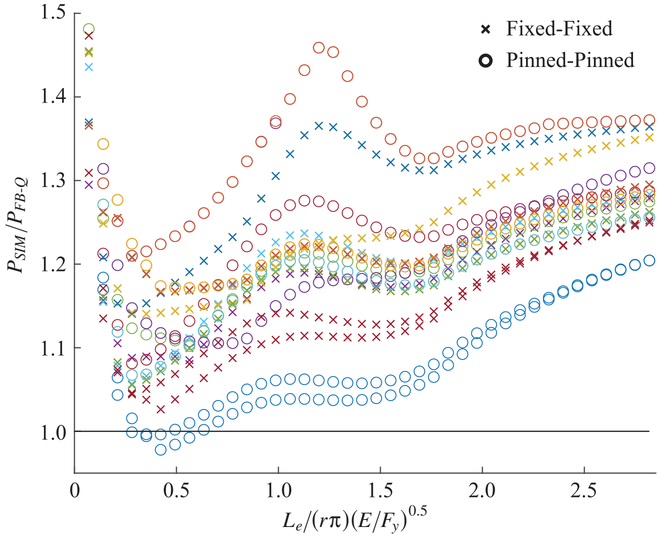

(c) *Flexural buckling provisions plus local buckling reductions.*

Fig. 20. FEA capacity versus design provision strength calculations with measured material properties. All sizes from Table 8 included.

AISC 370 could warrant later simplifications to the design provisions of unequal-leg angles.

The complex buckling behavior of stainless steel unequal-leg angles makes it difficult to establish a straightforward set of design provisions that accurately predict the true response. A central component of this challenge is accounting for the flexural-torsional buckling response, which is expected to control in all instances, in a form suitable for practicing engineers to apply. The current approach requires consideration of all global elastic buckling modes and then applying the same equations that were developed for flexural buckling to determine the nominal capacity of the column. As currently implemented, the inclusion of flexural-torsional buckling in the design provisions is a significant reduction from the flexural buckling capacity at short lengths as shown in Figure 21. This comparison was completed using the nominal yield strength but follows a similar pattern when using the measured yield strength.

As mentioned previously, this reduction was necessary when using nominal material properties to match finite element simulations. However, the simulations using measured material properties did not need the same reduction despite these models still exhibiting flexural-torsional buckling. When evaluating the same design equations for any global buckling mode, it should be noted that the assumed behavior reflects that the shear stiffness of stainless steel angles reduces proportionally with the longitudinal stiffness, which is not observed in carbon steel for axially loaded members (Galambos, 1991). The consideration of the actual shear stiffness can result in a smaller reduction from flexural buckling to the flexural-torsional response. Based on this reduced difference, not including the global flexural-torsional buckling reduction for carbon steel angles was determined to be acceptable as long as local buckling reductions were included to capture extreme cases of slender cross sections.

Determining the significance of the overestimated capacity requires knowledge of the realistic capacity of single angles. The flexural buckling coefficients given in Curve A were determined to be conservative for the physical stainless steel angles in this study; however, additional data are needed to determine if this is a trend or a unique result. An equivalent investigation can be extended to various stainless steel angle cross sections to consider implementing a similar methodology.

CONCLUSIONS

This study investigated the flexural-torsional buckling behavior of stainless steel unequal-leg single angles. A finite element modeling procedure was developed and validated by comparison to experimental results from 18 fixed-fixed Grade 304 stainless steel L3×2×¼ columns with lengths ranging from 10 to 148 in. The subsequent finite element-based parametric study considered 12 cross sections, nonslender-element for nominal material properties, with a L_e/r_z ratio ranging from 5 to 200 to incorporate elastic and inelastic failures. Each cross section was evaluated for a fixed-fixed and pinned-pinned flexural end restraint and one of three material models: nominal Grade 304, nominal Grade 304L, or the measured material properties determined through the validation study. A total of 2,880

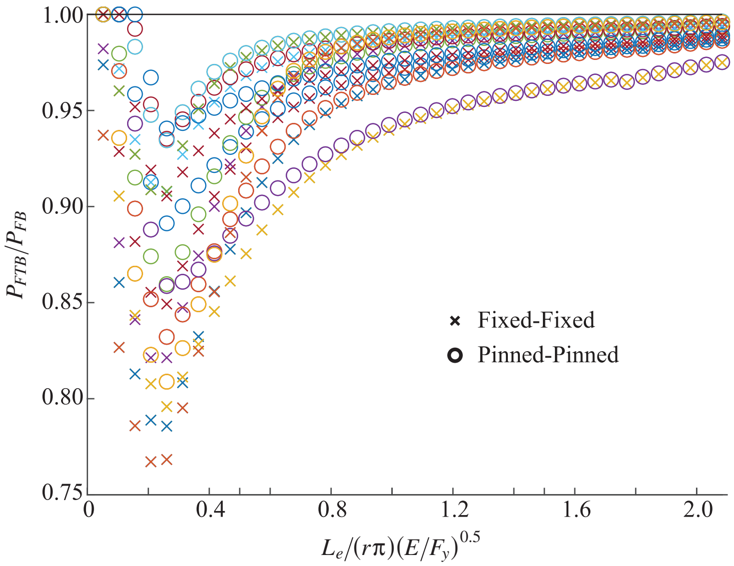

Fig. 21. Current design provision normalized by the flexural buckling only result using nominal material properties. All sizes from Table 8 included.

finite element models were run, and the simulations captured flexural-torsional buckling of all cross sections with both flexural and torsional dominated failures. It was determined that using the existing Curve A buckling coefficients in AISC 370 with nominal material properties required the consideration of flexural-torsional buckling design provisions to obtain results that were consistently conservative compared to the finite element results. Only considering flexural buckling resulted in an average 7% less conservative prediction in the worst-case instance, and half the models exhibited an unconservative prediction. While flexural-torsional buckling was also consistently observed when considering measured material properties, evaluation of the same flexural-torsional buckling design provisions resulted in excessive conservatism for most finite element results with measured material properties. The evaluation of flexural buckling with local buckling reductions, similar to the design provisions for carbon steel single angles, was found to approximate most flexural-torsional buckling concerns for the stainless steel single angles in this part of the study. Additional work should focus on verifying the appropriate stress-strain response for modeling stainless steel and expanding the study to include more slender-element cross sections to validate the consistency of this result and to determine if a limiting element slenderness of the cross section is applicable.

REFERENCES

AISC (2017), *Steel Construction Manual*, 15th Ed., American Institute of Steel Construction, Chicago, Ill.

AISC (2021), *Specification for Structural Stainless Steel Buildings,* ANSI/AISC 370-21, American Institute of Steel Construction, Chicago, Ill.

AISC (2022), *Specification for Structural Steel Buildings,* ANSI/AISC 360-22, American Institute of Steel Construction, Chicago, Ill.

Arrayago, I., Real, E., and Gardner, L. (2015), "Description of Stress–Strain Curves for Stainless Steel Alloys," *Materials & Design,* 87, 540–552. https://doi.org/10.1016/j.matdes.2015.08.001

Ashraf, M., Gardner, L., and Nethercot, D.A. (2006), "Compression Strength of Stainless Steel Cross-Sections," *Journal of Constructional Steel Research*, Vol. 62, No. 1-2, pp. 105–115. https://doi.org/10.1016/j.jcsr.2005.04.010

ASTM (2019), *Standard Specification for Carbon Structural Steel*, ASTM A36/A36M-19, ASTM International, West Conshohocken, Pa.

ASTM (2021), *Standard Specification for High-Strength Low-Alloy Columbium-Vanadium Structural Steel*, ASTM A572/A572M-21, ASTM International, West Conshohocken, Pa.

Baddoo, N. (2013), *Structural Stainless Steel*, Design Guide 27, American Institute of Steel Construction, Chicago, Ill.

Baddoo, N. and Meza, F. (2022), *Structural Stainless Steel*, Design Guide 27, 2nd Ed., American Institute of Steel Construction. Chicago, Ill.

Behzadi-Sofiani, B., Gardner, L., and Wadee, M.A. (2021), "Stability and Design of Fixed-Ended Stainless Steel Equal-Leg Angle Section Compression Members," *Engineering Structures,* Vol. 249, 113281. https://doi.org/10.1016/j.engstruct.2021.113281

Dassault Systems (2015a), *Abaqus 2016 Documentation*. http://130.149.89.49:2080/v2016/index.html

Dassault Systems (2015b), *Abaqus/CAE,* Version 6.16, Dassault Systems, Johnston, R.I.

de Menezes, A.A., da S. Vellasco, P.C.G., de Lima, L.R.O., and da Silva, A.T. (2019), "Experimental and Numerical Investigation of Austenitic Stainless Steel Hot-Rolled Angles under Compression," *Journal of Constructional Steel Research,* Vol. 152, pp. 42–56. https://doi.org/10.1016/j.jcsr.2018.05.033

Dinis, P.B., Camotim, D., Belivanis, K., Roskos, C., and Helwig, T.A. (2015), "On the Buckling, Post-Buckling and Strength Behavior of Thin-Walled Unequal-Leg Angle Columns," *Proceedings of the 2015 SSRC Annual Stability Conference*, Nashville, Tenn.

Dobrić, J., Filipović, A., Marković, Z., and Baddoo, N. (2020), "Structural Response to Axial Testing of Cold-Formed Stainless Steel Angle Columns," *Thin-Walled Structures,* Vol. 156, 106986. https://doi.org/10.1016/j.tws.2020.106986

Dundu, M. (2018), "Evolution of Stress–Strain Models of Stainless Steel in Structural Engineering Applications," *Construction and Building Materials,* Vol. 165, pp. 413–423. https://doi.org/10.1016/j.conbuildmat.2018.01.008

Filipović, A., Dobrić, J., Baddoo, N. R., and Može, P. (2021a), "Experimental Response of Hot-Rolled Stainless Steel Angle Columns," *Thin-Walled Structures,* Vol. 163, 107659. https://doi.org/10.1016/j.tws.2021.107659

Filipović, A., Dobrić, J., Budevac, D., Fric, N., and Baddoo, N. (2021b), "Experimental Study of Laser-Welded Stainless Steel Angle Columns," *Thin-Walled Structures,* Vol. 164, 107777. https://doi.org/10.1016/j.tws.2021.107777

Galambos, T.V. (1991), "Design of Axially Loaded Compressed Angles," *Proceedings of the 1991 SSRC Annual Stability Conference: 'Inelastic Behavior and Design of Frames,'* Chicago, Ill.

Gardner, L. and Ashraf, M. (2006), "Structural Design for Non-Linear Metallic Materials," *Engineering Structures,* Vol. 28, No. 6, pp. 926–934. https://doi.org/10.1016/j.engstruct.2005.11.001

Gardner, L. and Nethercot, D. (2004), "Experiments on Stainless Steel Hollow Sections—Part 1: Material and Cross-Sectional Behaviour," *Journal of Constructional Steel Research,* Vol. 60, No. 9, pp. 1291– 1318. https://doi.org/10.1016/j.jcsr.2003.11.006

Hill, H. (1944), *Determination of Stress-Strain Relations from the Offset Yield Strength Values*, Technical Note 927, National Advisory Committee for Aeronautics, Washington, D.C.

Houska, C. (2014), *Designing Stainless Steel Part 1*, Conference Presentation, NASSC: The Steel Conference, American Institute of Steel Construction, Toronto, ON, Canada.

Hradil, P., Talja, A., Real, E., Mirambell, E., and Rossi, B. (2013), "Generalized Multistage Mechanical Model for Nonlinear Metallic Materials," *Thin-Walled Structures,* Vol. 63, pp. 63–69. https://doi.org/10.1016/j.tws.2012.10.006

Kuwamura, H. (2003), "Local Buckling of Thin Walled Stainless Steel Members," *Steel Structures,* Vol. 3, pp. 191–201.

Laracuente, M.E. (2022), "Behavior of Concentrically Loaded Austenitic Stainless Steel Single Unequal-Leg Angles," Master's Thesis, University of Wisconsin–Madison, Madison, Wis.

Laracuente, M.E., Sippel, E.J., and Blum, H.B. (2022), "Stability Considerations of Unequal-Leg Angle Stainless Steel Columns," *Proceedings of the 2022 SSRC Annual Stability Conference,* SSRC, Denver, Colo.

Laracuente, M.E., Sippel, E.J., and Blum, H.B. (2023), "Stability Considerations of Laser Fused Unequal-Leg Angle Stainless Steel Columns," *Proceedings of the 2023 SSRC Annual Stability Conference*, SSRC, Charlotte, N.C.

Liang, Y., Jeyapragasam, V.V.K., Zhang, L., and Zhao, O. (2019), "Flexural-Torsional Buckling Behaviour of Fixed-Ended Hot-Rolled Austenitic Stainless Steel Equal-Leg Angle Section Columns," *Journal of Constructional Steel Research,* Vol. 154, pp. 43–54. https://doi.org/10.1016/j.jcsr.2018.11.019

Liao, K. (1982), "Compression Tests of Unequal-Leg Angles," Master's Thesis, Ohio State University, Columbus, Ohio.

Liu, Y. and Chantel, S. (2011), "Experimental Study of Steel Single Unequal-Leg Angles under Eccentric Compression," *Journal of Constructional Steel Research,* Vol. 67, No. 6, pp. 919–928. https://doi.org/10.1016/j.jcsr.2011.02.005

MacDonald, M., Rhodes, J., and Taylor, G.T. (2000), "Mechanical Properties of Stainless Steel Lipped Channels," *CCFSS Proceedings of International Specialty Conference on Cold-Formed Steel Structures (1971–2018)*, Session 11, No. 4. https://scholarsmine.mst.edu/isccss/15iccfss/15iccfss-session11/4

Meza, F.J., Baddoo, N., and Gardner, L. (2021), "Development of Flexural Buckling Rules for the New AISC Stainless Steel Design Specification," *ce/papers,* Vol. 4, pp. 1537–1542. https://doi.org/10.1002/cepa.1453

Mirambell, E. and Real, E. (2000), "On the Calculation of Deflections in Structural Stainless Steel Beams: An Experimental and Numerical Investigation," *Journal of Constructional Steel Research,* Vol. 54, No. 1, pp. 109–133. https://doi.org/10.1016/S0143-974X(99)00051-6

Ojalvo, M. (2011), "Opposing Theories and the Buckling Strength of Unequal-Leg Angle Columns," *Journal of Structural Engineering,* Vol. 137, No. 10, pp. 1104–1106. https://doi.org/10.1061/(ASCE)ST.1943-541X.0000389

Olsson, A. (2001), "Stainless Steel Plasticity: Material Modelling and Structural Applications," Doctoral Dissertation, Luleå University of Technology, Luleå, Sweden.

Quach, W., Teng, J.G., and Chung, K.F. (2008), "Three-Stage Full-Range Stress-Strain Model for Stainless Steels," *Journal of Structural Engineering,* Vol. 134, No. 9, pp. 1518–1527. https://doi.org/10.1061/(ASCE)0733-9445(2008)134:9(1518)

Rasmussen, K.J. (2003), "Full-Range Stress–Strain Curves for Stainless Steel Alloys," *Journal of Constructional Steel Research,* Vol. 59, No. 1, pp. 47–61. https://doi.org/10.1016/S0143-974X(02)00018-4

Rasmussen, K.J. (2005), "Design of Angle Columns with Locally Unstable Legs," *Journal of Structural Engineering,* Vol. 131, No. 10, pp. 1553–1560. https://doi.org/10.1061/(ASCE)0733-9445(2005)131:10(1553)

Reynolds, N.A. (2013), "Behavior and Design of Concentrically Loaded Duplex Stainless Steel Single Equal-Leg Angle Struts," Doctoral Dissertation, Georgia Institute of Technology, Atlanta, Ga.

Sarquis, F.R., Lima, L.R.O. de, da S. Vellasco, P.C.G., and Rodrigues, M.C. (2020), "Experimental and Numerical Investigation of Hot-Rolled Stainless Steel Equal Leg Angles under Compression," *Thin-Walled Structures,* Vol. 151, 106742. https://doi.org/10.1016/j.tws.2020.106742

Schafer, B.W., Li, Z., and Moen, C.D. (2010), "Computational Modeling of Cold-Formed Steel," *Thin-Walled Structures,* Vol. 48, No. 10-11, pp. 752–762. https://doi.org/10.1016/j.tws.2010.04.008

Sippel, E.J. (2022), "Structural Analysis with Non-Symmetric Cross Sections," Doctoral Dissertation, University of Wisconsin–Madison. https://asset.library.wisc.edu/1711.dl/IAZMR5L7NRQME8F/R/file-e9e51.pdf

Sirqueira, A.d.S., Vellasco, P.C.S., Lima, L.R.O. de, and Sarquis, F.R. (2020), "Experimental Assessment of Stainless Steel Hot-Rolled Equal Legs Angles in Compression," *Journal of Constructional Steel Research,* Vol. 169, 106069. https://doi.org/10.1016/j.jcsr.2020.106069

Sun, Y., Liu, Z., Liang, Y., and Zhao, O. (2019), "Experimental and Numerical Investigations of Hot-Rolled Austenitic Stainless Steel Equal-Leg Angle Sections," *Thin-Walled Structures,* Vol. 144, 106225. https://doi.org/10.1016/j.tws.2019.106225

Timoshenko, S. and Gere, J. (1961), *Theory of Elastic Stability*, 2nd Ed., McGraw-Hill Book Company, New York, N.Y.

Wu, F.-H. (1982), "Experimental Determination of Buckling Loads for Unequal Leg Angles with Concentric Loads," Master's Thesis, Ohio State University, Columbus, Ohio.

Zhang, L., Liang, Y., and Zhao, O. (2020), "Experimental and Numerical Investigations of Pin-Ended Hot-Rolled Stainless Steel Angle Section Columns Failing by Flexural Buckling," *Thin-Walled Structures,* Vol. 156, 106977. https://doi.org/10.1016/j.tws.2020.106977

Zhang, L., Liang, Y., and Zhao, O. (2021), "Laboratory Testing and Numerical Modelling of Pin-Ended Hot-Rolled Stainless Steel Angle Section Columns Failing by Flexural-Torsional Buckling," *Thin-Walled Structures,* Vol. 161, 107395. https://doi.org/10.1016/j.tws.2020.107395

Zhang, L., Tan, K.H., and Zhao, O. (2019), "Experimental and Numerical Studies of Fixed-Ended Cold-Formed Stainless Steel Equal-Leg Angle Section Columns," *Engineering Structures,* Vol. 184, pp. 134–144. https://doi.org/10.1016/j.engstruct.2019.01.083

Zhang, Y., Bu, Y., Wang, Y., Wang, Z., and Ouyang, Y. (2021), "Study of Flexural–Torsional Buckling Behaviour of 6061-T6 Aluminium Alloy Unequal-Leg Angle Columns," *Thin-Walled Structures,* Vol. 164, 107821. https://doi.org/10.1016/j.tws.2021.107821

Zhang, Y., Wang, Y., Wang, Z., Bu, Y., Fan, S., and Zheng, B. (2020), "Experimental Investigation and Numerical Analysis of Pin-Ended Extruded Aluminium Alloy Unequal Angle Columns," *Engineering Structures,* Vol. 215, 110694. https://doi.org/10.1016/j.engstruct.2020.110694

Ziemian, R.D. (2010), *Guide to Stability Design Criteria for Metal Structures*, 6th Ed., John Wiley & Sons, Hoboken, N.J.

Review and Evaluation of the Separation Factor Approach for Structural Reliability

ISABELLE M. JOLLYMORE, KYLE TOUSIGNANT, and JEFFREY A. PACKER

ABSTRACT

Studies have indicated that resistance factors calculated using a first-order second moment reliability method that uncouples the load effect from the resistance, termed the "separation factor approach" (SFA), differ considerably from those calculated using more accurate methods that also consider statistical variations in both the load effects and resistance. This can be attributed, in part, to the SFA implementing a separation factor, α, equal to 0.55, which was determined from tentative loading criteria and statistics in the 1970s. This paper amalgamates the disparate literature/background on the SFA and investigates its sources of error to illustrate its inherent assumptions and limitations. Three studies are conducted whose results are used to recommend appropriate separation factors (with associated bounds) for use in the SFA when determining resistance factors for steel components.

It is found that $\alpha = 0.55$ was calibrated to an atypical range of live-to-dead load ratios and small values of V_R, which undermines its applicability when used in conjunction with modern-day statistics. Despite this, $\alpha = 0.55$ is found to perform well when the reliability index, β, is equal to 3.0. For $\beta = 3.5$ and $\beta = 4.0$, $\alpha = 0.70$ and $\alpha = 0.80$, respectively, give results that agree with more accurate reliability methods at a live-to-dead load ratio of 3.0.

KEYWORDS: structural reliability, first-order second moment method, reliability index, resistance factors, separation factor.

INTRODUCTION

The load and resistance factor design (LRFD) philosophy uses load and resistance factors to achieve an acceptably small notional probability of failure for steel members, connections, connectors, and whole structures. Load factors are used to increase the load effect, and resistance factors are used to decrease the resistance to emulate a worst-case scenario. Load and resistance factors are chosen such that, if the LRFD design criterion is satisfied under these worst-case conditions, then the notional probability of failure is deemed acceptably small. LRFD is an alternative to the allowable strength design (ASD) philosophy, which aims for the resistance to be greater than the load effect by a factor of safety.

Various reliability methods are used to calculate resistance factors for steel components. A resistance distribution is developed for the component using a representative sample of adequate size, and the statistics pertaining to this are extracted; the same is done for the loading if it is assumed to contribute to reliability. Then, for a target level of reliability (embodied by the reliability index, which corresponds to a specific probability of failure over the component's design life), the resistance factor can be calculated. These methods can also be employed to calculate and compare reliability indices for a given resistance factor.

The separation factor approach (SFA) is a reliability method that arose from the work of Galambos and Ravindra (1973). They derived an equation for the resistance factor, ϕ, that conveniently simplifies the calculation by uncoupling the load effect from the resistance in the ultimate limit state design equation, thereby establishing the inherent assumption that resistance alone determines reliability according to the SFA. This simplification was achieved by introducing a separation factor, α, as proposed by Lind (1971), for the resistance and each load component. Historically, the separation factor has been taken to be 0.55, as per the recommendation of Galambos and Ravindra.

As recently as 2010, use of $\alpha = 0.55$ was endorsed by the Structural Stability Research Council (SSRC) in Appendix B.10 of the SSRC Guide (Ziemian, 2010). This factor continues to be used in conjunction with the SFA for reliability analyses in academia and by some material standards

Isabelle M. Jollymore, Research Assistant, Department of Civil & Resource Engineering, Dalhousie University, Halifax, Nova Scotia, Canada. Email: is582948@dal.ca

Kyle Tousignant, Associate Professor, Department of Civil & Resource Engineering, Dalhousie University, Halifax, Nova Scotia, Canada. Email: kyle.tousignant@dal.ca (corresponding)

Jeffrey A. Packer, Professor, Department of Civil & Mineral Engineering, University of Toronto, Toronto, Ontario, Canada. Email: jeffrey.packer@utoronto.ca

Paper No. 2024-07R

technical committees for resistance factor calculations (CSA, 2011). It has come to light more recently that resistance factors calculated using this approach can differ from those calculated using more accurate methods, particularly for the case where $\alpha = 0.55$ is adopted. As a result, CSA S408-11 (2011) stipulates that this approach should not be used for the calculation of resistance factors. On the other hand, the SFA equation is specified in Commentary Section C2.3.5 of ASCE 7 (2022) to derive resistance factors, using a separation factor of approximately 0.7.

This paper addresses the need for a comprehensive review of the SFA by gathering significant literature on the topic since its inception and explores the implications of the governing assumptions and simplifications of the SFA to establish its merits, shortcomings, and potential sources of numerical error. Following this, three studies are carried out: (1) a recalibration of separation factors using modern statistics, (2) a comparison of the performance of the SFA in modern reliability studies to a more accurate reliability method that considers the loading in addition to resistance, and (3) a numerical experiment in which the SFA using the optimal separation factors determined from the previous two studies and the more-accurate reliability method are equated. The results of these three studies are then used to propose new separation factors with associated bounds for use in the SFA; this paper focuses specifically on reliability of steel components.

LOAD AND RESISTANCE FACTOR DESIGN

The LRFD philosophy may be expressed by the equation (Ziemian, 2010):

$$\phi R_n \geq \sum \gamma_i Q_i \tag{1}$$

which states that the factored resistance (or available strength), ϕR_n, must equal or exceed the effect of the factored loads, $\Sigma\gamma_i Q_i$.

The nominal resistance, R_n, is the strength of an element computed based on nominal material and geometrical properties, and the resistance factor, ϕ, is a dimensionless factor ≤ 1.0. The product ϕR_n embodies the uncertainties associated with the resistance, R, of a structural component. The products of each specified load effect, Q_i, and its corresponding load factor, γ_i, are summed to constitute the load effect side of the design criterion expressed by Equation 1. The term $\Sigma\gamma_i Q_i$ reflects the possibility of overloading and the uncertainties inherent in the calculation of the load effect(s), Q. The probability of failure of a structural component (i.e., the probability that the component will reach a specified ultimate limit state) is equal to the probability that the cumulative load effect, Q, exceeds the resistance, R (i.e., $R < Q$), as shown in Figure 1(a).

LRFD in North America can be traced to the work of Cornell (1969), and the postulate that the probability of failure, p_F, may be accurately determined from the probability density curve for the safety margin (or limit state function), $Z = R - Q$, where p_F is equal to the area under the curve where $Z < 0$, as shown in Figure 1(b). If R and Q are considered random variables and the arbitrary probability density curve of the safety margin Z is known, then a standardized variate, U (of Z), can be defined as:

$$U = \frac{Z - Z_m}{\sigma_Z} \tag{2}$$

where Z_m is the mean of Z and σ_Z is the standard deviation of Z. The expression that describes the probability of failure, p_F, can then be written as (Melchers and Beck, 2018):

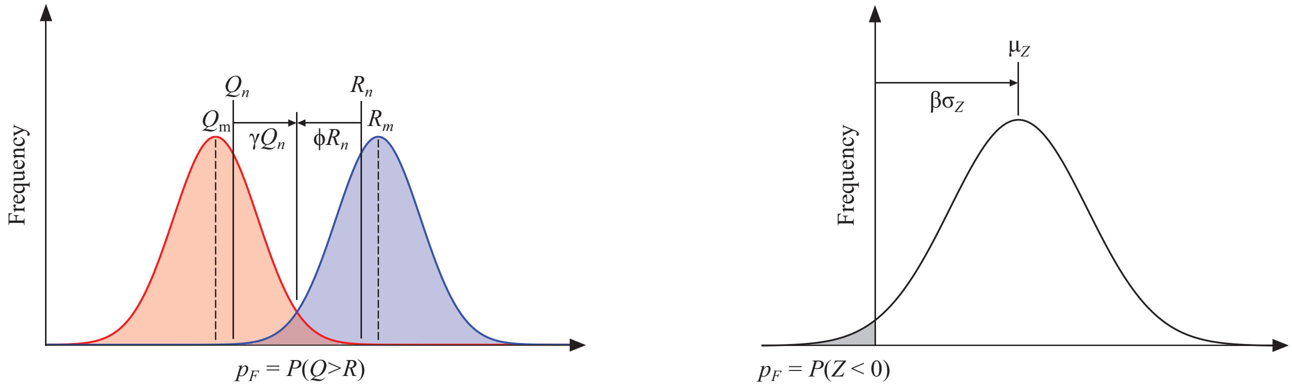

(a) *Load effect,* Q, *and resistance,* R

(b) *Safety margin,* Z

Fig. 1. Symbol, variable, and model definitions.

$$p_F = P\left[U < -\frac{Z_m}{\sigma_Z}\right] \tag{3a}$$

$$p_F = F_U\left[-\frac{Z_m}{\sigma_Z}\right] \tag{3b}$$

where F_U is the cumulative distribution function of U.

The above-mentioned postulate, combined with the principle of constant reliability (Lind, 1971), comprises the basis of first-order second moment reliability methods. Such reliability methods involve (1) linear (i.e., first-order) limit state functions and (2) computing a notional reliability measure, which is a function only of the means and variances (first and second moments, respectively) of the random variables (e.g., R and Q) rather than their probability distributions (Ellingwood et al., 1980). First-order reliability methods are often used because of their simplicity and ability to treat all uncertainties in a design problem in a consistent manner; hence, first-order methods have been used to develop LRFD criteria for steel components.

The ratio Z_m/σ_z in Equations 3a and 3b is referred to as the reliability index, β; it is a unitless measure of safety (or reliability) that represents the number of standard deviations between the mean value of Z (Z_m) and the failure condition ($Z = 0$) (Cornell, 1969). The reliability index has also been called the "safety index" or "performance index"; the term "reliability index" is adopted herein (Ang and Cornell, 1974; Galambos and Ravindra, 1973). The greater the value β, the greater the reliability, where the reliability is quantified as $1 - p_F$ (Allen, 1991). In other words, if σ_z remains constant, then a positive (right-hand) shift in Z_m will reduce p_F; this holds true for practically all probability distributions used for Z.

Equation 3b can therefore be written as:

$$p_F = F_U[-\beta] \tag{4}$$

According to Equation 4, β provides a direct measure of p_F (or, conversely, reliability) if the probability distribution of Z (and hence, the real values of Z_m and σ_z) is known. In practice, however, the distributions of R and Q (and Z) are invariably estimated. When this is done, p_F (calculated from Equation 4) is referred to as the "notional" probability of failure, indicating that it should be interpreted, at best, in a comparative sense (e.g., to evaluate the relative safety of various design alternatives) (Ellingwood et al., 1980).

To estimate the statistics for $Z = R - Q$ (i.e., Z_m and σ_Z) from corresponding estimates of those statistics for R and Q (i.e., R_m and Q_m; the mean values of R and Q, respectively; and σ_R and σ_Q, the corresponding standard deviations), the following statistical laws must be realized (Benjamin and Cornell, 1970):

1. If R and Q are random variables, $Z_m = (R - Q)_m = R_m - Q_m$.
2. Provided that R and Q are independent random variables, ${\sigma_Z}^2 = {\sigma_R}^2 + {\sigma_Q}^2$.
3. V_Z cannot be directly represented as a function of V_R and V_Q.

V_R and V_Q are the coefficients of variation (COVs) of R and Q, respectively. The COV of a random variable is a normalized measure of the dispersion of the probability distribution about the mean value and is equal to the ratio of the standard deviation to the mean. A relatively high COV is undesirable in the context of reliability because it is indicative of greater variation and, thus, lower certainty.

If R and Q are considered independent normal random variables, the probability density curve for $Z = R - Q$ is a normal curve with mean $Z_m = (R - Q)_m = R_m - Q_m$ and standard deviation $\sigma_Z = \sqrt{\sigma_R^2 + \sigma_Q^2}$ (Allen, 1991; Thoft-Christensen and Baker, 1982). However, according to Allen, a better model for structural reliability is to replace the distributions of R and Q by the distributions of their natural logarithms, $\ln R$ and $\ln Q$, and to fit normal curves to these such that the two tails overlap (denoting the region in which failure may occur) in the same way as shown in Figure 1(a). Hence, if R and Q are log-normally distributed, $Z = \ln R - \ln Q$ is taken as normally distributed, and:

$$\beta = \frac{\ln R_m - \ln Q_m}{\sqrt{\sigma_{\ln R}^2 + \sigma_{\ln Q}^2}} \tag{5a}$$

$$\beta = \frac{\left[\ln(R/Q)\right]_m}{\sqrt{\sigma_{\ln R}^2 + \sigma_{\ln Q}^2}} \tag{5b}$$

$$\beta = \frac{\ln(R_m/Q_m)}{\sqrt{\sigma_{\ln R}^2 + \sigma_{\ln Q}^2}} \tag{5c}$$

where $\ln R_m$, $\ln Q_m$, and $\ln(R_m/Q_m)$ are the mean values of $\ln R$, $\ln Q$, and $\ln(R/Q)$, respectively, and $\sigma_{\ln R}$ and $\sigma_{\ln Q}$ are the corresponding standard deviations of $\ln R$ and $\ln Q$, respectively. Log-normally distributed random variables can take only positive real values, which is true-to-life for most engineering measurements, and perhaps the benefit implied by Allen (1991).

By converting the mean values and standard deviations of $\ln R$ and $\ln Q$ to those for R and Q (i.e., through mathematical manipulation), Equation 5c for β can be written as follows (Thoft-Christensen and Baker, 1982; Allen, 1975; Allen, 1991; Galambos and Ravindra, 1973):

$$\beta = \frac{\ln\left[(R_m/Q_m)\sqrt{(1+V_Q^2)/(1+V_R^2)}\right]}{\sqrt{\ln(1+V_R^2)(1+V_Q^2)}} \tag{6}$$

Equation 6 is currently used in CSA S6:19 (CSA, 2019) to calculate β for bridges and bridge components. However, if V_R and V_Q are small [i.e., according to Ellingwood et al. (1980), if V_R and V_Q are both less than about 0.30], then:

$$\beta = \frac{\ln(R_m/Q_m)}{\sqrt{V_R^2 + V_Q^2}} \tag{7}$$

Historically, this assumption has been referred to as the "small-variance assumption," despite referring to the COVs and not the variances of the variables R and Q; for the sake of clarity, it will be termed the "small-COV assumption" herein. The format according to Equation 7 has long been the basis of LRFD criteria in North America (ASCE, 2022; CSA, 2011), as studies have shown that R and Q follow an approximately log-normal distribution (Xi and Packer, 2021; Ellingwood et al., 1980).

Small-COV Assumption

The accuracy of the simplification in Equation 7 is dependent not only on the magnitudes of V_R and V_Q, but also on the ratio R_m/Q_m. For adequate reliability, R_m must be greater than Q_m; however, the distance between these two means, $Z_m = R_m - Q_m$, is not generally known. The effect of the ratio R_m/Q_m on the relative accuracy of the simplification in Equation 7 for predicting β (i.e., how the small-COV assumption affects the calculated β) is shown in Figures 2(a)–2(c), using R_m/Q_m values of 1.70, 2.00, and 2.50, respectively. These values are chosen because Appendix E of the 1969 version of the CSA S16 standard, which was based on ASD, indicates a basic safety factor (R_m/Q_m) of 1.67. This has been employed in structural steel design for several decades, and the factor 1.67 has been rounded off to 1.70 here to avoid unwarranted precision. Table E1 of CSA S16-69 indicates further variations in this factor (from 1.67 to 2.50) based on the type of stress undergone by various elements (CSA, 1969).

In Figures 2(a)–2(c), the solid lines represent Equation 6, long dashed lines represent Equation 7, and short dashed (vertical/horizontal) lines represent the upper limits on V_R and V_Q for the small-COV assumption. Plotting with V_Q on the x-axis and V_R on the y-axis displays the actual equations as somewhat elliptical curves and the approximate equations as circles.

It is evident that when $V_R < 0.30$ and $V_Q < 0.30$ there is a minimum level of reliability (i.e., value of β) associated with R_m/Q_m, which increases with increasing R_m/Q_m [and $\ln(R_m/Q_m)$] as this causes the curves to move further from the origin. It is also clear that for values of V_R that are small (i.e., approaching zero), the approximation given by Equation 7 will underestimate β for a fixed V_R and V_Q. Similarly, for values of V_Q that are small, the approximation will overestimate β for a fixed V_R and V_Q.

To investigate these trends further, a numerical experiment was performed wherein values between 0 and 0.30 were randomly selected for V_R and V_Q, and corresponding values of β and its approximation, denoted β_a, were calculated using Equations 6 and 7, respectively, to determine the percent error in the approximation of β, $\varepsilon_\beta = (\beta - \beta_a)/\beta \times 100\%$. This was performed 100,000 times for each of $R_m/Q_m = 1.70$, $R_m/Q_m = 2.00$, and $R_m/Q_m = 2.50$. The mean percent error, $\overline{\varepsilon}$, the variance of the percent error, σ_ε^2, the maximum percent error, ε_{MAX}, and the minimum percent error, ε_{MIN}, were calculated for each R_m/Q_m. These parameters are calculated to illustrate the distribution of ε_β, as well as best-case ($\varepsilon_{MIN} \le \varepsilon_\beta \le 0$) and worst-case ($\varepsilon_{MAX}$) scenarios. It is found that as R_m/Q_m increases, $\overline{\varepsilon}$ increases and σ_ε^2 decreases; the exact values from the experiment are shown in Table 1. Note that $\varepsilon_\beta > 0$ corresponds to an underestimate by Equation 7 and $\varepsilon_\beta < 0$ corresponds to an overestimate by Equation 7, and thus for all three cases, the approximation results in an underestimate on average.

Whenever a small value of V_R was selected, Equation 6 yielded a larger β than the approximation by Equation 7 (i.e., a positive error), proving the earlier point that the approximation underestimates β when V_R approaches zero. Similarly, whenever a small value of V_Q was selected, the actual equation yielded a smaller β than the approximation (i.e., a negative error), proving that the approximation overestimates β when V_Q approaches zero. Another trend that is discernable from Figures 2(a)–2(c) and from the numerical experiment is that the approximation improves as β increases. Whenever small values of both V_R and V_Q were selected, along with a large value of β, the percent error due to the approximation by Equation 7 was approximately zero.

DERIVATION OF THE SEPARATION FACTOR APPROACH

The governing criterion for LRFD can be expressed in the form of a design criterion (Cornell, 1969):

$$R_m \ge \theta Q_m \tag{8}$$

where the central safety factor, θ, combines the uncertainties of resistance and load effects.

If the small-COV assumption discussed previously (Ellingwood et al., 1980) is valid, Equations 7 and 8 can be used to express the central safety factor approximately as:

$$\theta = \exp\left(\beta\sqrt{V_R^2 + V_Q^2}\right) \tag{9}$$

where Equation 9 implies that $\theta = R_m/Q_m$. Otherwise, Equations 6 and 8 are used to write the equation accurately as:

Table 1. Mean, Variance, Maximum, and Minimum Error in the Approximation of β Using Equation 7

R_m/Q_m	$\bar{\varepsilon}$ (%)	σ_ε^2 (%^{2})	ε_{MAX} (%)	ε_{MIN} (%)
1.70	0.866	11.7	9.49	–6.50
2.00	0.909	6.99	7.87	–4.34
2.50	0.948	4.14	6.54	–2.68

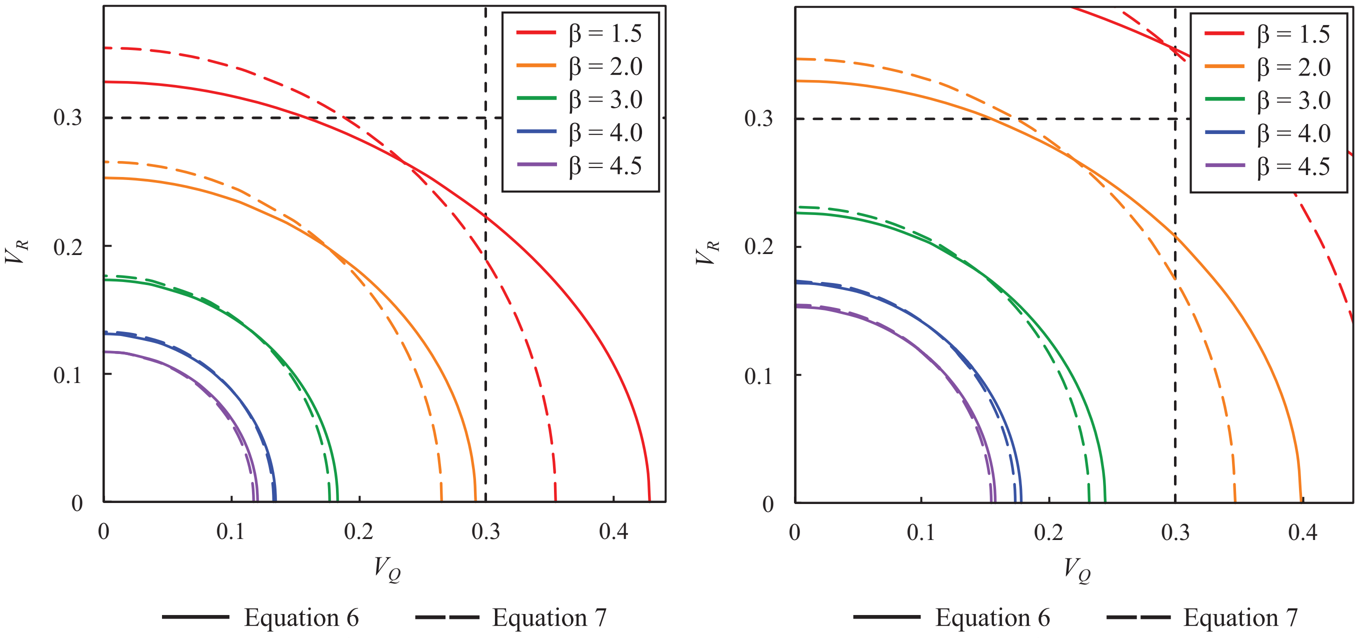

(a) For R_m/Q_m *= 1.70*

(b) For R_m/Q_m *= 2.00*

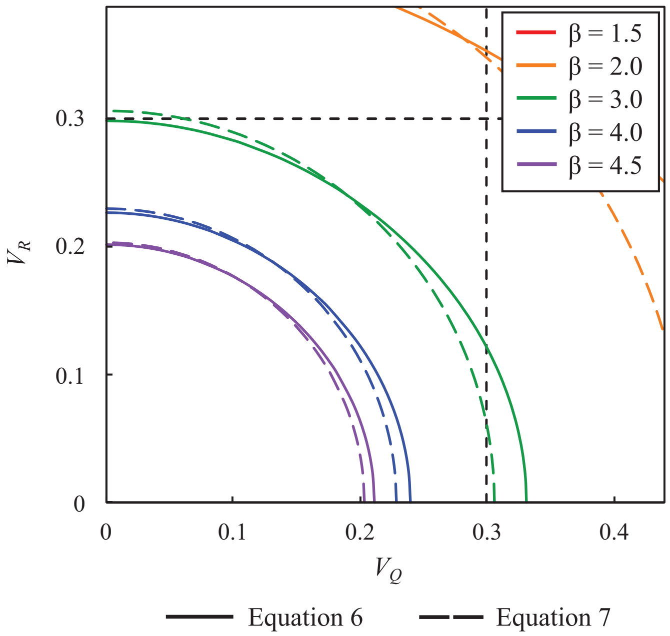

(c) For R_m/Q_m *= 2.50*

Fig. 2. Approximations to various reliability indices, β.

$$\theta = \frac{\exp\left(\beta\sqrt{\ln\left(1+V_R^2\right)\left(1+V_Q^2\right)}\right)}{\sqrt{\dfrac{\left(1+V_Q^2\right)}{\left(1+V_R^2\right)}}} \tag{10}$$

The small-COV form of the central safety factor equation (i.e., Equation 9) is used in the SFA. If the COVs are not small, and if any of the particular cases addressed in the previous subsection hold true, use of this small-COV form can result in excessive error.

The root term in Equation 9 prevents the independent treatment of the resistance and load terms. It is advantageous to separate the COVs so that when a target β is chosen, the resistance factor, ϕ, can be evaluated for different loading uncertainties. Additionally, this would enable γ_i for different load types to be evaluated independent of other load types and of resistance uncertainties.

Lind (1971) showed that the root expression in Equation 9, or any two-variable expression in that form, could be linearized by introducing a so-called separation factor, α:

$$\sqrt{V_R^2 + V_Q^2} \approx \alpha\left(V_R + V_Q\right) \tag{11a}$$

where

$$\alpha = \frac{\sqrt{1+\left(V_R/V_Q\right)^2}}{1+\left(V_R/V_Q\right)} \tag{11b}$$

As shown by the dotted line in Figure 3(a), if V_R/V_Q is near unity, α is relatively constant. This is not always practical; however, if V_R/V_Q is instead restricted to the range $⅓ \leq V_R/V_Q \leq 3$, then α can be set equal to 0.75 with less than 6% error (Lind, 1971), as demonstrated in Figure 3(b).

Therefore, if $V_R < 0.30$ and $V_Q < 0.30$ to satisfy the small-COV assumption, and $⅓ \leq V_R/V_Q \leq 3$, Equation 8 can be written as

$$\exp\left(-\beta\alpha V_R\right)R_m \geq \exp\left(\beta\alpha V_Q\right)Q_m \tag{12}$$

or as

$$\delta_R \exp\left(-\beta\alpha V_R\right)R_n \geq \delta_Q \exp\left(\beta\alpha V_Q\right)Q_n \tag{13}$$

where the bias coefficient for the resistance, δ_R, is the ratio of the mean resistance to the nominal resistance, R_m/R_n, Q_n is the nominal (or specified) total load effect, and δ_Q is the bias coefficient for the total load effect.

Equation 13 takes a similar form as the criterion in Equation 1. Comparing the two, it follows that:

$$\phi = \delta_R \exp\left(-\alpha\beta V_R\right) \tag{14}$$

Equation 14 is the basic form of the equation used in many codes, standards, and guides (e.g., Ravindra and Galambos, 1978; Fisher et al., 1978; Ziemian, 2010; ASCE, 2022) to calculate resistance factors for a target reliability index (or reliability indices for a target resistance factor). This equation clearly demonstrates the philosophy that resistance is the sole determinant of reliability, which is central to the SFA. In the next section, the right-hand side of Equation 13 is separated further into constituent load effects.

Consideration of Different Load Types

Equation 13 was derived by treating the load effect, *Q*, as if it originated from a single load type acting on a structural steel component. However, in general, *Q* arises due to effects from dead load, *D*, live load, *L*, wind load, *W*, and other actions.

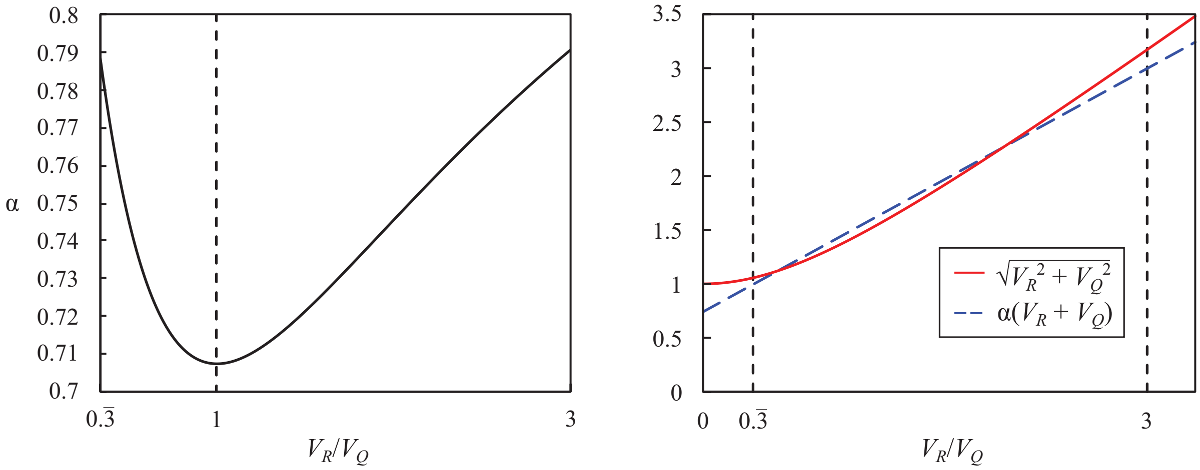

(a) Values of α from Equation 11a

(b) Linearization with α = 0.75

Fig. 3. Variation of α with V_R/V_Q, and accuracy of a single α-value.

In the following, the COV of the total load effect, V_Q, and the central safety factor approximation, θ_a, are derived as shown in Appendix B of Galambos and Ravindra (1973). From these workings, equations for ϕ and γ_i are also defined. Galambos and Ravindra considered two common cases for the load effect side of the first-order second moment design criterion: (1) dead and lifetime maximum live load and (2) dead, sustained live load and lifetime maximum wind load.

Dead and Lifetime Maximum Live Load

Galambos and Ravindra (1973) assumed the load effect, Q, for combined dead and live gravity load, to have the following form:

$$Q = ET \tag{15a}$$

where

$$T = c_D AD + c_L BL \tag{15b}$$

and where D and L are random variables representing dead and live load intensities, respectively, which embody uncertainties due to the idealization of loads that vary randomly in space and time with equivalent uniformly distributed or concentrated design loads; c_D and c_L are deterministic influence coefficients that transform the dead and live load intensities into dead and live load effects, respectively; A and B are random variables reflecting uncertainties in the transformation of the idealized design loads into dead and live load effects, respectively; T is a random variable denoting the total load undergone by a member; and E is a random variable representing the uncertainties in structural analysis.

Assuming E and T are uncorrelated, it follows from Equation 15a that:

$$V_Q = \sqrt{V_E^2 + V_T^2 + V_E^2 V_T^2} \tag{16}$$

where V_E and V_T are the COVs of E and T, respectively. If both V_E and V_T are less than 0.30, the error introduced by eliminating the product term does not exceed 2.2%. Thus, by neglecting the product term, Equation 16 becomes:

$$V_Q = \sqrt{V_E^2 + V_T^2} \tag{17}$$

The equation for V_T can be written as:

$$V_T = \frac{\sqrt{c_D^2 A_m^2 D_m^2 \left(V_A^2 + V_D^2\right) + c_L^2 B_m^2 L_m^2 \left(V_B^2 + V_L^2\right)}}{c_D A_m D_m + c_L B_m L_m} \tag{18}$$

where the numerator represents the standard deviation of T, denoted σ_T, and the denominator is the mean of T, denoted T_m. It is difficult to obtain information about the distributions of the random variables A and B, so it has been common historically to take $A_m = B_m = 1.0$, which is valid for uniformly distributed dead and live loads (Jeong, 1981). Thus, the equation for V_Q can be rewritten by inserting Equation 18 into Equation 17, where $A_m = B_m = 1.0$ and $c_D = c_L = 1.0$:

$$V_Q = \sqrt{V_E^2 + \frac{D_m^2\left(V_A^2 + V_D^2\right) + L_m^2\left(V_B^2 + V_L^2\right)}{\left(D_m + L_m\right)^2}} \tag{19}$$

The governing criterion for the separation factor can be carried further to include the effects of multiple load types (in this case, D and L). Firstly, Equation 12 can be written as:

$$\exp\left(-\beta\alpha_R V_R\right) R_m \geq \exp\left(\beta\alpha_Q V_Q\right) Q_m \tag{20}$$

where two distinct separation factors—α_R for the resistance side and α_Q for the load side—are introduced to encourage a better approximation of Equation 8.

Noting from Equation 17 that $V_Q = \sqrt{V_E^2 + V_T^2}$, and using the concept illustrated by Equation 11a, Equation 20 can be rewritten as:

$$\exp\left(-\beta\alpha_R V_R\right) R_m \geq \left[\exp\left(\beta\alpha_Q \alpha'_E V_E\right) E_m\right]\left[\exp\left(\beta\alpha_Q \alpha_T V_T\right) T_m\right] \tag{21}$$

The second exponential term on the right-hand side of Equation 21 can be approximated further by using the constant and linear terms of a Taylor series exponential expansion [i.e., exp(x) = 1 + x]:

$$\exp\left(\beta\alpha_Q \alpha_T V_T\right) T_m \approx \left(1 + \beta\alpha_Q \alpha_T V_T\right)\left(D_m + L_m\right) \tag{22a}$$

$$\exp\left(\beta\alpha_Q \alpha_T V_T\right) T_m \approx \left(1 + \frac{\beta\alpha_Q \alpha_T \sqrt{D_m^2\left(V_A^2 + V_D^2\right) + L_m^2\left(V_B^2 + V_L^2\right)}}{D_m + L_m}\right)\left(D_m + L_m\right) \tag{22b}$$

where Equation 18 was substituted into Equation 22a to get Equation 22b. An error is introduced with this simplification, which is investigated in the next subsection.

The square root term in Equation 22b can be separated as proposed by Lind (1971) (in Equation 23b), and after rearranging, the final approximation is achieved in Equation 23d:

$$\exp\left(\beta\alpha_Q \alpha_T V_T\right) T_m \approx \left(D_m + L_m\right) + \beta\alpha_Q \alpha_T \sqrt{D_m^2\left(V_A^2 + V_D^2\right) + L_m^2\left(V_B^2 + V_L^2\right)} \tag{23a}$$

$$\exp\left(\beta\alpha_Q \alpha_T V_T\right) T_m \approx D_m + L_m + \beta\alpha_Q \alpha_T \alpha'\left(D_m\sqrt{V_A^2 + V_D^2} + L_m\sqrt{V_B^2 + V_L^2}\right) \tag{23b}$$

$$\exp(\beta\alpha_Q\alpha_T V_T)T_m \approx D_m + L_m + \beta\alpha_Q\alpha_T\alpha'_D D_m\sqrt{V_A^2+V_D^2} + \beta\alpha_Q\alpha_T\alpha'_L L_m\sqrt{V_B^2+V_L^2} \tag{23c}$$

$$\exp(\beta\alpha_Q\alpha_T V_T)T_m \approx \left(1+\beta\alpha_Q\alpha_T\alpha'_D\sqrt{V_A^2+V_D^2}\right)D_m + \left(1+\beta\alpha_Q\alpha_T\alpha'_L\sqrt{V_B^2+V_L^2}\right)L_m \tag{23d}$$

If Equation 23d is substituted into Equation 21, and the products of the separation factor terms are combined into individual separation factors (i.e., $\alpha_E = \alpha_Q\alpha'_E$, $\alpha_D = \alpha_Q\alpha_T\alpha'_D$, and $\alpha_L = \alpha_Q\alpha_T\alpha'_L$), then:

$$\exp(-\beta\alpha_R V_R)R_m \ge \left[\exp(\beta\alpha_E V_E)E_m\right]\left[\left(1+\beta\alpha_D\sqrt{V_A^2+V_D^2}\right)D_m + \left(1+\beta\alpha_L\sqrt{V_B^2+V_L^2}\right)L_m\right] \tag{24}$$

Given that the first-order second moment design criterion for dead and live load can be written as:

$$\phi R_m \ge \gamma_E E_m(\gamma_D D_m + \gamma_L L_m) \tag{25}$$

where γ_E is the load factor accounting for uncertainties in structural analysis, γ_D is the dead load factor, and γ_L is the live load factor, it is implied that:

$$\phi = \delta_R \exp(-\alpha_R\beta V_R) \tag{26a}$$

$$\gamma_E = \exp(\alpha_E\beta V_E) \tag{26b}$$

$$\gamma_D = 1+\alpha_D\beta\sqrt{V_A^2+V_D^2} \tag{26c}$$

$$\gamma_L = 1+\alpha_L\beta\sqrt{V_B^2+V_L^2} \tag{26d}$$

R_m is obtained by rearranging Equation 24 and writing it as an equality, as shown in Equation 27a. Assuming $\theta = R_m/Q_m$, dividing both sides by $Q_m = E_m T_m = E_m(D_m + L_m) = E_m(D_m/L_m + 1)$ gives the central safety factor approximation in Equation 27b:

$$R_m = \frac{\exp(\beta\alpha_E V_E)E_m\left[\left(1+\beta\alpha_D\sqrt{V_A^2+V_D^2}\right)\frac{D_m}{L_m}+\left(1+\beta\alpha_L\sqrt{V_B^2+V_L^2}\right)\right]}{\exp(-\beta\alpha_R V_R)} \tag{27a}$$

$$\theta_a = \frac{\exp(\beta\alpha_E V_E)\left[\left(1+\beta\alpha_D\sqrt{V_A^2+V_D^2}\right)\frac{D_m}{L_m}+\left(1+\beta\alpha_L\sqrt{V_B^2+V_L^2}\right)\right]}{\left(\frac{D_m}{L_m}+1\right)\exp(-\beta\alpha_R V_R)} \tag{27b}$$

Note that both θ and θ_a are technically approximate. As θ_a introduces two additional assumptions on top of the initial small-COV assumption (i.e., simplification of the V_Q equation using another small-COV assumption, and use of the linear Taylor series approximation), it is deemed an approximation of θ.

The values of the four separation factors α_R, α_E, α_D, and α_L are selected to minimize the error in the approximation of the central safety factor, which is defined as $\varepsilon_\theta = (\theta - \theta_a)/\theta$.

Dead, Sustained Live Load, and Lifetime Maximum Wind Load

For this case, the load effect, Q, was assumed to take the same form as in the case of dead and live load (i.e., the form given by Equation 15a). The random variable T can be expressed as:

$$T = c_D AD + c_L BL + c_W CW \tag{28}$$

where W is a random variable representing wind load intensity, c_W is the deterministic influence coefficient that transforms the wind load intensity into wind load effect, and C is a random variable reflecting uncertainties in the transformation of the idealized design load into wind load effect.

Applying the same rationale and assumptions that were employed for the case of dead and live load to this case, the approximation to the central safety factor is derived as:

$$\theta_a = \frac{\exp(\beta\alpha_E V_E)\left[\left(1+\beta\alpha_D\sqrt{V_A^2+V_D^2}\right)+\left(1+\beta\alpha_L\sqrt{V_B^2+V_L^2}\right)\frac{L_m}{D_m}+\left(1+\beta\alpha_W\sqrt{{V_C}^2+{V_W}^2}\right)\frac{W_m}{D_m}\right]}{\left(1+\frac{L_m}{D_m}+\frac{W_m}{D_m}\right)\exp(-\beta\alpha_R V_R)} \tag{29}$$

where

$$V_Q = \sqrt{V_E^2 + \frac{c_D^2 A_m^2 D_m^2(V_A^2+V_D^2)+c_L^2 B_m^2 L_m^2(V_B^2+V_L^2)+c_W^2 C_m^2 W_m^2(V_C^2+V_W^2)}{(c_D A_m D_m + c_L B_m L_m + c_W C_m W_m)^2}} \tag{30}$$

and $A_m = B_m = C_m = 1.0$ and $c_D = c_L = c_W = 1.0$. The first-order second moment design criterion for dead, live, and wind load can be written as:

$$\phi R_m \ge \gamma_E E_m(\gamma_D D_m + \gamma_L L_m + \gamma_W W_m) \tag{31}$$

where γ_W is the wind load factor. By comparing the form of Equation 31 to that of Equation 29, it is implied that:

$$\gamma_W = 1+\alpha_W\beta\sqrt{V_C^2+V_W^2} \tag{32}$$

The equations for ϕ, γ_E, γ_D, and γ_L are unaltered by the inclusion of wind load (i.e., the same as Equations 26a–26d).

Linear Taylor Series Approximation

In the derivation of θ_a for both load cases, the exponential term for the load effect was approximated using the linear Taylor series expansion (for the dead and live load case, Equation 22a). Since the Taylor series is a summation of terms [where the series becomes equal to the function it is approximating as x (i.e., $\beta\alpha_Q\alpha_T V_T$) approaches infinity], this approximation will result in an underestimate for all x (i.e., $\beta\alpha_Q\alpha_T V_T$) greater than zero because it lacks most of the terms. From Figure 4, it is shown that as $\beta\alpha_Q\alpha_T V_T$ departs from zero (i.e., the point about which the Taylor series is centered), the underestimate becomes greater in magnitude.

As demonstrated in Figure 4, the linear function deviates from the exponential function rather quickly. It is useful to quantify this deviation with typical values of each of these parameters; these were chosen to be $0 \le \beta \le 5.0$, $0.5 \le \alpha_Q \le 0.7$, $0.5 \le \alpha_T \le 0.7$, and $0 \le V_T \le 0.3$ (i.e., $0 \le \beta\alpha_Q\alpha_T V_T \le 0.735$). The error does not change with $c_L L_m / c_D D_m$, as $c_L L_m / c_D D_m$ participates as a mere scaling factor in Equation 22b and is thereby unaffected by the introduction of the Taylor series approximation.

This investigation found that the maximum approximation error exceeds 16%. For a more typical range of reliability indices (i.e., $3.0 \le \beta \le 4.0$) and the same ranges of α_Q, α_T, and V_T as before, $\beta\alpha_Q\alpha_T V_T$ ranges from 0 to 0.588, and the maximum error is roughly 11.8%.

Error in the Approximation to the Central Safety Factor

As indicated previously, Galambos and Ravindra (1973) opted to minimize the error in the approximation to the central safety factor as a means of determining appropriate α-values for use in the SFA. To supplement their argument in Appendix B, Galambos and Ravindra (1973) presented Figures B-1 through B-6: Figures B-1–B-3 explored the dead and lifetime maximum live load case at different values of β, while Figures B-4–B-6 explored the dead, sustained live load, and lifetime maximum wind load case at different values of β. This subsection (1) outlines the process that led to the recommendation of a universal α-value ($\alpha = 0.55$) to be used in the SFA, and (2) investigates the Figures B-1–B-6 presented in Galambos and Ravindra (1973).

For their investigation, Galambos and Ravindra (1973) prescribed values (or values with associated frequencies of occurrence) to the variables which define the design situation for both loading cases; these are identified in Table 2.

The shorthand notations V_{AD}, V_{BL}, and V_{CW} were adopted to represent $\sqrt{V_A^2 + V_D^2}$, $\sqrt{V_B^2 + V_L^2}$, and $\sqrt{V_C^2 + V_W^2}$, respectively. Galambos and Ravindra (1973) used V_D, V_L, and V_W interchangeably with V_{AD}, V_{BL}, and V_{CW}, respectively, as it was assumed that $A_m = B_m = C_m = 1.0$; therefore, $V_A = V_B = V_C = 0$, which means that $V_D = V_{AD}$, $V_L = V_{BL}$, and $V_W = V_{CW}$.

For Figures B-1–B-3, $V_{Q,min} \approx 0.06$ (when V_E, V_{AD}, and V_{BL} are smallest and $c_D D_m / c_L L_m$ is largest) and $V_{Q,max} \approx 0.25$ (vice versa); because $V_Q < 0.30$, the small-COV assumption always holds. However, for Figures B-4 and B-6, $V_{Q,min} \approx 0.22$ (when V_E, V_{AD}, V_{BL}, V_{CW}, and $c_D D_m / c_W W_m$ are smallest and $c_D D_m / c_L L_m$ is largest) and $V_{Q,max} \approx 0.60$ (vice versa); in this case, the small-COV assumption does not always hold.

Galambos and Ravindra (1973) carried out an error minimization procedure, whereby various combinations of α_R, α_E, α_D, and α_L (and α_W for the wind case) were tested to determine the set that resulted in the most optimal (minimized) distribution of error. To do this, one of the three

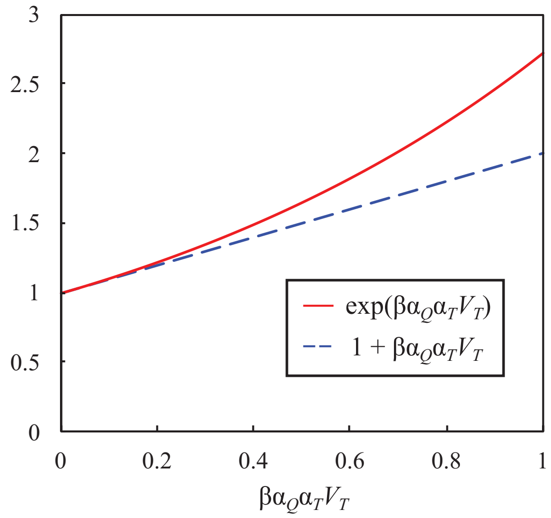

Fig. 4. Exponential function and the linear Taylor series approximation.

Table 2. Data Variables as Specified in Appendix B of Galambos and Ravindra (1973)

Variable	Figure(s)	Range	Value	Frequency of Occurrence
V_R	B-1, B-2, B-3, B-4, B-5, B-6	0.10–0.15	0.13	1.0
V_E	B-1, B-2, B-3, B-4, B-5, B-6	0.05–0.15	0.05 0.10 0.15	0.30 0.50 0.20*
$\sqrt{V_A^2+V_D^2}=V_{AD}$	B-1, B-2, B-3	0.02–0.10	0.02 0.06 0.10	0.20 0.60 0.20
	B-4, B-5, B-6		0.02 0.06 0.10	0.30 0.50 0.20
$\sqrt{V_B^2+V_L^2}=V_{BL}$	B-1, B-2, B-3	0.10–0.40	0.10 0.25 0.40**	0.20 0.60 0.20
	B-4, B-5, B-6	0.40–0.70	0.40 0.55 0.70	0.50 0.30 0.20
$\sqrt{V_C^2+V_W^2}=V_{CW}$	B-1, B-2, B-3	N/A	N/A	N/A
	B-4, B-5, B-6	0.30–0.40	0.30 0.35 0.40	0.50 0.30 0.20
$c_D D_m / c_L L_m$	B-1, B-2, B-3	1.00–4.00	1.00 1.60 4.00	0.20 0.50 0.30
	B-4, B-5, B-6	0.10–0.30	0.10 0.20 0.30	0.30 0.50 0.20
$c_D D_m / c_W W_m$	B-1, B-2, B-3	N/A	N/A	N/A
	B-4, B-5, B-6	0.25–1.00	0.25 0.50 1.00	0.50 0.30 0.20
β	B-1, B-4	3.0–4.0	3.0	1.0
	B-2, B-5		3.25	1.0
	B-3, B-6		3.5	1.0

* In the parameter list for Figure B-1 in Galambos and Ravindra, this was mistakenly written as 0.10.

** In the parameter list for Figure B-1 in Galambos and Ravindra, this was mistakenly written as 0.60.

prescribed values of V_E, V_{AD}, V_{BL}, and $c_D D_m / c_L L_m$ (and V_{CW} and $c_D D_m / c_W W_m$ for the wind case) were randomly sampled according to the frequencies indicated in Table 2; the values selected were used to calculate V_Q, θ, θ_a, and ε_θ in sequence. This process was repeated to an acceptable degree of convergence and for different values of β. For the dead and lifetime maximum live load case, Galambos and Ravindra found that $\alpha_R = 0.52$, $\alpha_E = 0.60$, $\alpha_D = 0.70$, and $\alpha_L = 0.60$ resulted in the least error, yielding a mean error of zero and a standard deviation of 3%; a confirmatory study by the authors found that the mean error was 0.075 and the standard deviation was 3.22%, which corroborates the claims by Galambos and Ravindra. The characteristics that signify an optimal error distribution were not explicitly defined in Galambos and Ravindra, so these are inferred to be (1) a mean error sufficiently close to zero and (2) a reasonably small standard deviation.

Galambos and Ravindra (1973) found that the separation factors were relatively insensitive to changes in the frequencies of occurrence of the varying parameters listed in Table 2, and used this observation as grounds for using a single constant separation factor, α, as opposed to multiple, independent separation factors, in favor of simplicity. Thus, they explored the case where $\alpha = 0.55$ and produced histograms that depicted the distribution of ε_θ for different values of β. To confirm the results from Galambos and Ravindra, the authors repeated their error minimization process herein using 10,000 iterations, which resulted in acceptable convergence of the error distribution. Figures 5(a)–5(f) show comparisons of Figures B-1–B-6 as depicted in Appendix B of Galambos and Ravindra and the remakes of Figures B-1–B-6 resulting from the authors' error minimization process.

From Figures 5(a)–5(f), it becomes evident that Figure B-2 and Figures B-4–B-6 presented in Appendix B of Galambos and Ravindra (1973) do not align with the assigned values and frequencies of the parameters shown therein. The disparity between these histograms and their corresponding parameter lists was investigated by considering the following errors in the latter:

- For Figure B-2, the values of $c_D D_m / c_L L_m$ used to generate the histogram were the reciprocals of the $c_D D_m / c_L L_m$ values identified in the parameter list (i.e., instead of $c_D D_m / c_L L_m = \{1.00, 1.00, 1.60, 1.60, 1.60, 1.60, 1.60, 4.00, 4.00, 4.00\}$, $c_D D_m / c_L L_m = \{1.00, 1.00, 0.625, 0.625, 0.625, 0.625, 0.625, 0.25, 0.25, 0.25\}$ was used).
- For Figures B-4–B-6, the values of $c_D D_m / c_L L_m$ and $c_D D_m / c_W W_m$ used to generate the histograms were the reciprocals of the $c_D D_m / c_L L_m$ and $c_D D_m / c_W W_m$ values identified in the parameter lists; instead of $c_D D_m / c_L L_m = \{0.10, 0.10, 0.10, 0.20, 0.20, 0.20, 0.20, 0.20, 0.30, 0.30\}$ and $c_D \overline{D} / c_W \overline{W} = \{0.25, 0.25, 0.25, 0.25, 0.25, 0.50, 0.50, 0.50, 1.00, 1.00\}$, $c_D D_m / c_L L_m = \{10.0, 10.0, 10.0, 5.00, 5.00, 5.00, 5.00, 5.00, 3.33, 3.33\}$ and $c_D D_m / c_W W_m = \{4.00, 4.00, 4.00, 4.00, 4.00, 2.00, 2.00, 2.00, 1.00, 1.00\}$ were used.
- For Figure B-5, the values of V_L and V_W used to generate the histograms were completely different from the values identified in the parameter lists; through an iterative investigation by the authors, it was found that $V_L = \{0, 0, 0, 0, 0, 0.08, 0.08, 0.08, 0.14, 0.14\}$ and $V_W = \{0, 0, 0, 0, 0, 0.02, 0.02, 0.02, 0.16, 0.16\}$ produced a distribution much like that which Galambos and Ravindra presented.

Figures 6(a)–6(d) show that the aforementioned alterations result in error distributions that sufficiently match those of Galambos and Ravindra (1973).

Several of the statistical values that Galambos and Ravindra (1973) prescribed (i.e., the ranges and values in Table 2) are not in agreement with the accepted statistics of today; these differences are discussed in greater detail later. Most notably, the range of live-to-dead load ratios they assigned differ greatly from the values used in modern day. A typical live-to-dead load range for steel components at the ultimate limit state is $1.0 \leq c_L L_m / c_D D_m \leq 3.0$. The upper limit (i.e., $c_L L_m / c_D D_m = 3.0$) is of notable significance, as in AISC 360, the safety factors in ASD were calibrated to give the same structural reliability as resistance factors in LRFD at a live-to-dead load ratio of 3.0 (AISC, 2022).

Galambos and Ravindra (1973) assigned the range $1.0 \leq c_D D_m / c_L L_m \leq 4.0$ to Figures B-1 and B-3 and $3.33 \leq c_D D_m / c_L L_m \leq 10.0$ to Figures B-4–B-6; these correspond to $0.25 \leq c_L L_m / c_D D_m \leq 1.0$ and $0.10 \leq c_L L_m / c_D D_m \leq 0.30$, respectively, which are atypical ranges for steel components at the ultimate limit state. Figure B-2 was the only figure to which Galambos and Ravindra prescribed a reasonable live-to-dead load range: $1.0 \leq c_L L_m / c_D D_m \leq 4.0$ (or as they had written, $0.25 \leq c_D D_m / c_L L_m \leq 1.0$). However, the mean and variance of the error for Figure B-2 is much higher than the mean and variance of any of the other figures, which suggests that the selection of $\alpha = 0.55$ was based on the more unusual live-to-dead load cases (though still subject to the variability of the other parameters).

INVESTIGATING THE PERFORMANCE OF THE SEPARATION FACTOR APPROACH

In this section, a series of studies is performed on the SFA to investigate its performance with $\alpha_R = 0.55$ and when modified to reflect modern statistics. A recommendation is made based on the collective findings of these studies. These studies focus on the dead plus live load case only; counter to the dead, live, and wind load case, this case is not only prevalent in literature, but is generally more applicable to the steel components considered within the scope of this paper.

Separation Factor Recalibration

This study employs a methodology to recalibrate the separation factors used in the SFA. Using updated statistical values, optimal α-values are determined through a similar iterative process as was used by Galambos and Ravindra (1973), for $\beta = 3.0$ and $\beta = 4.0$, as well as $\delta_R = 1.00$ and $\delta_R = 1.30$ (i.e., four times for each combination of these).

Firstly, $V_E = 0.0$ (and similarly, $V_A = 0.0$ and $V_B = 0.0$) was chosen for the recalibration of α_R. Most modern reliability studies of steel members and components assume that the method of structural analysis is devoid of error (i.e., $E = 1.0$), manifested by no mention of V_E. Furthermore, according to the CSA S6:19 Commentary, statically determinate analysis has an associated bias coefficient and COV of 1.0 and 0.0, respectively (CSA, 2019).

To begin the recalibration, the values or ranges of discrete values with associated frequencies of occurrence shown in Table 3 were assigned to each of the design parameters (COVs, bias coefficients, etc.). The distributions for V_R and δ_R were based on the results of 21 modern reliability studies

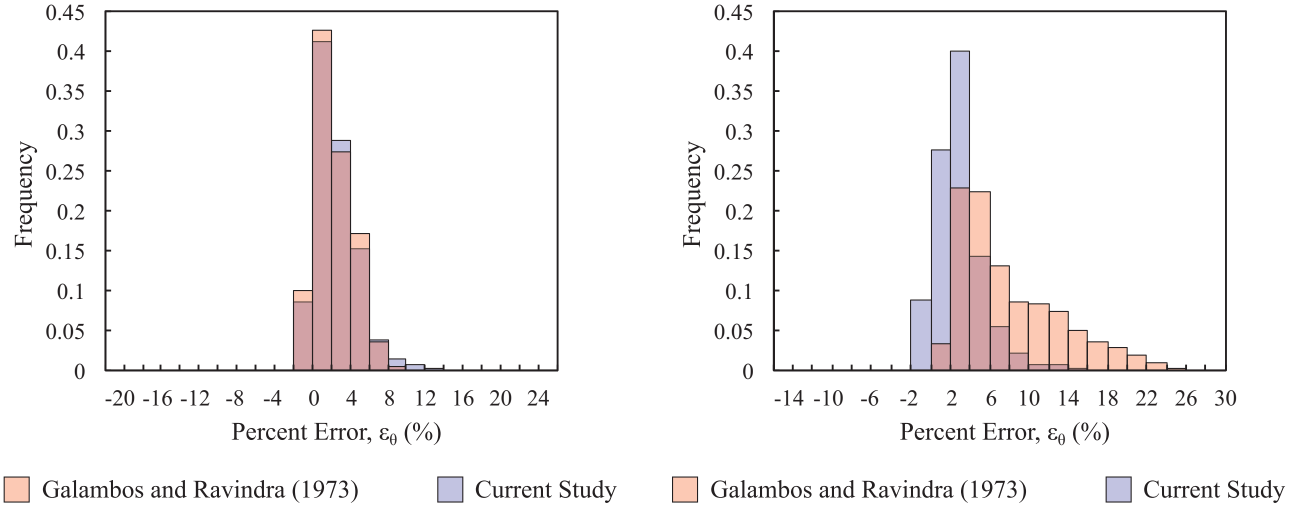

(a) Figure B-1 comparison *(b) Figure B-2 comparison*

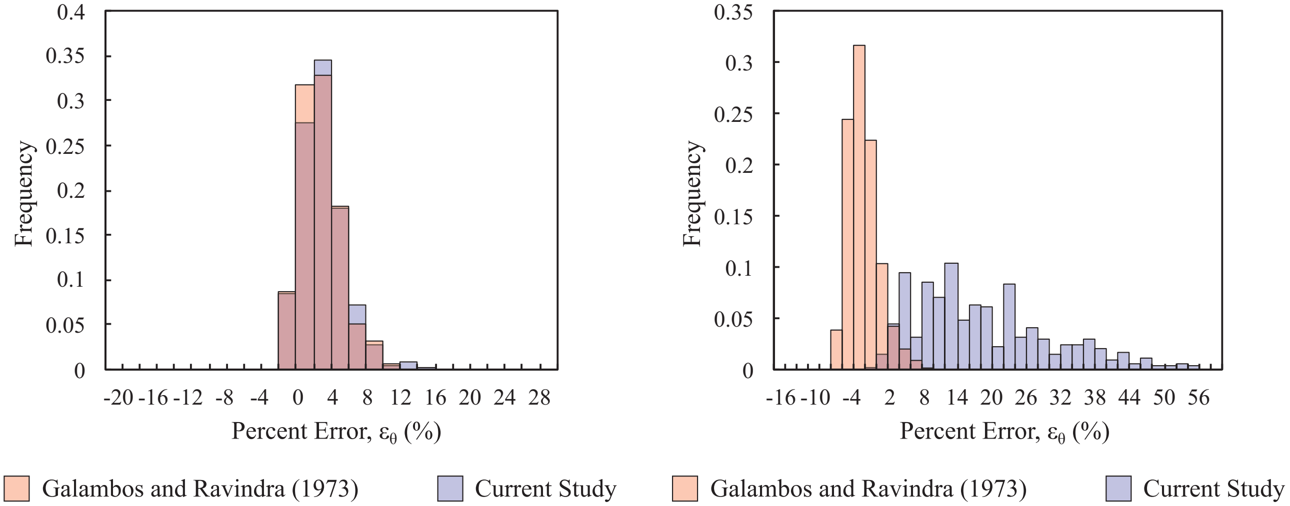

(c) Figure B-3 comparison *(d) Figure B-4 comparison*

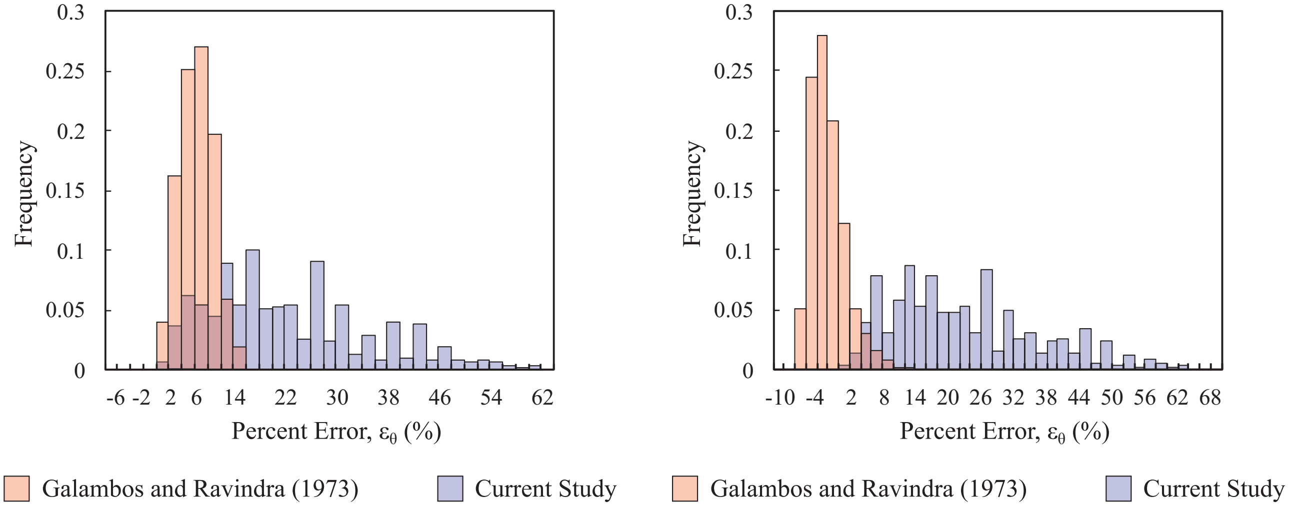

(e) Figure B-5 comparison *(f) Figure B-6 comparison*

Fig. 5. Comparison of the current study results to original error distributions from Galambos and Ravindra (1973).

and statistical data collections, where $\delta_R = 1.30$ represents the mean of the δ_R distribution. Random sampling was then used to calculate ε_θ 50,000 times to produce an error distribution for all combinations of relevant α-values (i.e., α_D, α_L, and α_R) using increments of 0.01. The bounds of these are shown in Table 3. Here, 50,000 iterations were chosen because there are more possible combinations of design parameters than before, and thus more iterations were required for adequate convergence.

It is worth noting the difference between the values used by Galambos and Ravindra (1973) (i.e., the values in Table 2) and those in Table 3, as these generally demonstrate how the statistical values that are widely accepted among researchers have changed over the past 50 years. It was established that Galambos and Ravindra adopted an atypical range for $c_D D_m / c_L L_m$ in their calibration of the SFA and that $1.0 \le c_L L_m / c_D D_m \le 3.0$ (i.e., $0.33 \le c_D D_m / c_L L_m \le 1.0$) is a typical range; this is adopted in the recalibration study herein. Another notable difference can be found in V_R. Modern literature revealed a distribution of V_R akin to the simplified distribution adopted in Table 3, which contains values much higher than the upper limit adopted by Galambos and Ravindra. As a high V_R is indicative of a relatively poor correlation between nominal and measured resistance, Galambos and Ravindra essentially adopted a somewhat optimistic range of V_R in their calibration of

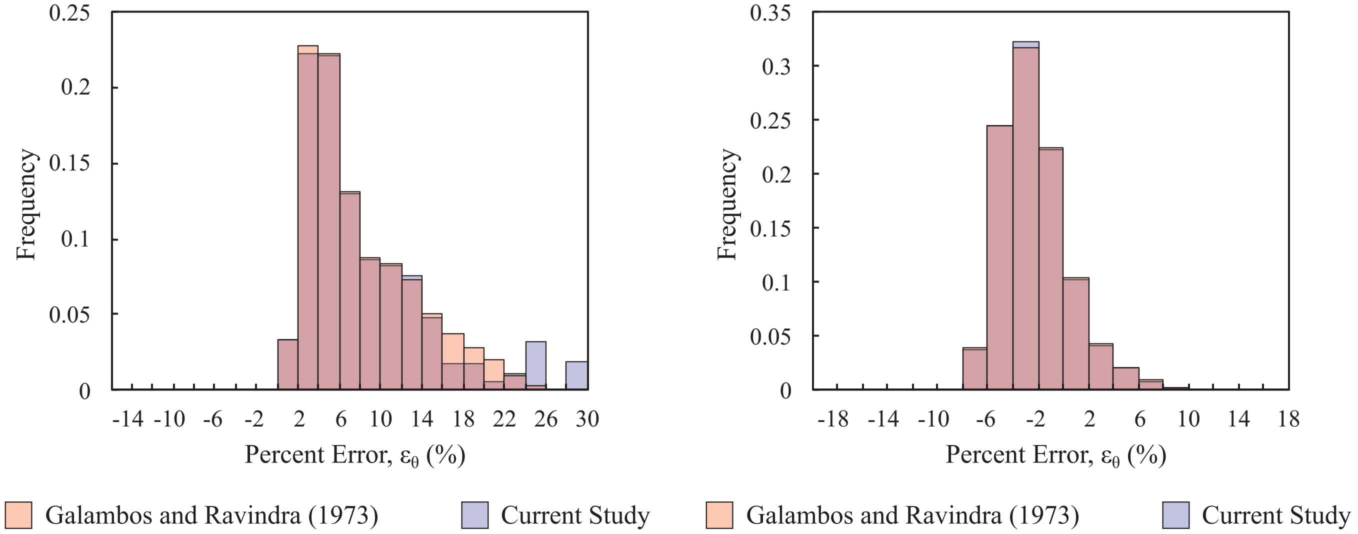

(a) Figure B-2 comparison

(b) Figure B-4 comparison

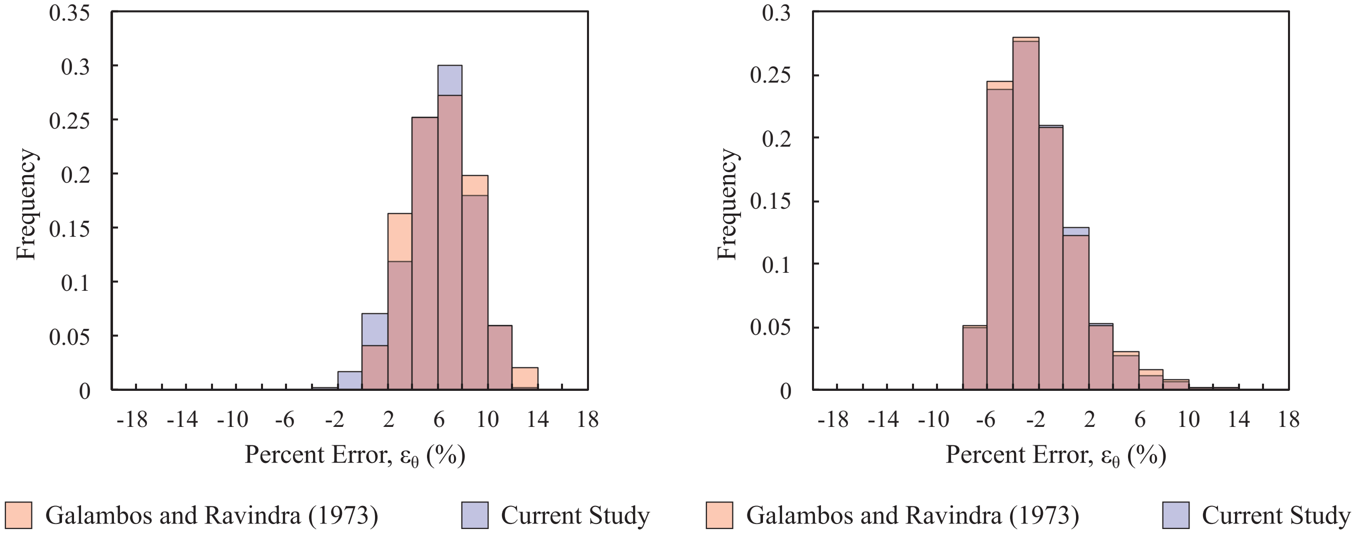

(c) Figure B-5 comparison

(d) Figure B-6 comparison

Fig. 6. Comparison of the modified current study results to original error distributions from Galambos and Ravindra (1973).

Table 3. Data Variables for Recalibrating the Separation Factor(s)

Variable	Value	Frequency of Occurrence
V_R	0.06 0.10 0.14 0.18 0.22 0.26 0.30 0.34	0.02 0.20 0.24 0.10 0.16 0.18 0.05 0.05
V_E	0.0	1.0
V_A	0.0	1.0
V_D	0.10	1.0
V_B	0.0	1.0
V_L	0.27† 0.32††	0.33 0.67
δ_R	1.00 1.30	1.0 1.0
δ_D	1.05	1.0
δ_L	0.78†† 0.90†	0.67 (when $V_L = 0.32$) 0.33 (when $V_L = 0.27$)
$c_D D_m / c_L L_m$	0.33 0.50 1.00	0.40 0.20 0.40

† Value from Bartlett et al. (2003)
†† Value from Schmidt and Bartlett (2002)

the SFA, which may contribute to why $\alpha_R = 0.55$ produces less conservative (more optimistic) values of ϕ compared to more modern methods.

Combinations of α-values that meet the criteria for mean error, $\bar{\varepsilon}$, and coefficient of skewness (COS) of the error, υ, shown in Table 4 were chosen during the iterative process. Then, of the qualifying α-values, optimal combinations were selected based on those that yielded the minimum variance.

The values and thresholds shown in Table 4 are based on extensive numerical experiments performed on the data/statistics used by Galambos and Ravindra (1973) in the initial calibration of the SFA. With these data, it was found that a relatively small negative $\bar{\varepsilon}$ (i.e., slight overestimate on average), a limit on the positive skew (i.e., data forming a rightward tail), and sufficiently minimized variance were optimal distribution characteristics, which resulted in approximately <25% probability of positive error values (i.e., underestimates). Thus, using adjusted ranges of α-values, an optimal set of α-values that repeated these results for modern statistics was investigated.

The amount of positive skew was limited by defining an upper threshold for the COS, which is a measure of skew in a set of data, where a positive COS indicates positively skewed data. The COS is defined as follows:

$$\upsilon = \frac{3(\bar{\varepsilon} - \dot{\varepsilon})}{\sigma_\varepsilon} \tag{33}$$

where $\dot{\varepsilon}$ is the median of the percent error and σ_ε is the standard deviation of the percent error. As seen in Table 4, only a slight positive skew was considered permissible, as greater skew to the right increases the magnitude of underestimates, which is unconservative. Recall that Galambos and Ravindra (1973) did not consider the COS as a criterion for error minimization, only mean error and standard deviation (variance). The results of implementing the above process are shown in Table 5.

Table 4. Thresholds for Separation Factors and Statistical Parameters

Bias Coefficient, δ_R	Parameter	Lower Limit (Inclusive)	Upper Limit (Inclusive)
1.00	α_R	0.60	0.90
	α_D	0.10	1.50
	α_L	0.10	1.50
	Mean, $\bar{\varepsilon}$	–3.00	–1.00
	COS, υ	N/A	0.50
1.30	α_R	0.80	1.20
	α_D	0.50	2.00
	α_L	0.50	2.00
	Mean, $\bar{\varepsilon}$	–9.00	–7.00
	COS, υ	N/A	0.50

Table 5. Optimal Separation Factors

Reliability Index, β	Bias Coefficient, δ_R	α_R	α_D	α_L	Variance
3.0	1.00	0.70	0.45	0.95	7.65
	1.30	0.80	1.00	1.65	11.8
4.0	1.00	0.70	0.30	1.05	13.1
	1.30	0.85	0.50	1.55	33.3

The results in Table 5 can be illustrated in histograms, like those used by Galambos and Ravindra (1973), to depict the distribution of error; these are shown in Figures 7(a)–7(d). As before, the statistical data in Table 3 and 50,000 iterations were used.

For each of the experiments used to produce Figures 7(a)–7(d), the percentage of iterations that gave an error value greater than zero was 16.4%, 1.91%, 17.3%, and 13.9%, respectively. Thus, in all cases, the percentage of positive error values (i.e., underestimates) was confirmed to be <25%.

Evaluating the SFA with Different Separation Factors

This study evaluates the performance of the SFA using different values of α_R when applied to four unique, published reliability studies (henceforth referred to as case studies). The aim of this study is to discern how the results vary between methods to hypothesize the scenarios in which the SFA deviates from the "true" value of ϕ, as well as the scenarios in which it converges on an acceptable value. Three calibrations of the SFA are utilized in this study:

1. Equation 26a using $\alpha_R = 0.55$ (i.e., the SFA as it was originally conceived).
2. Equation 26a with $\alpha_R = 0.70$ when $\beta = 3.0$ and when $\beta = 4.0$ (i.e., the α-values for $\delta_R = 1.00$).
3. Equation 26a with $\alpha_R = 0.80$ when $\beta = 3.0$ and $\alpha_R = 0.85$ when $\beta = 4.0$ (i.e., the α-values for $\delta_R = 1.30$).

Another existing reliability method is also presented in this study: the "approximate first-order reliability method" (or approximate FORM), which is outlined in Appendix B of CSA S408-11 (CSA, 2011). Contrary to the SFA, approximate FORM couples the load and resistance terms when calculating ϕ (CSA, 2011). The general equation for calculating ϕ using the approximate FORM methodology is:

$$\phi = \delta_R \frac{\sum \gamma_i Q_i}{Q_m} \exp\left(-\beta_T \sqrt{V_R^2 + V_Q^2}\right) \tag{34}$$

where β_T is the target reliability index (CSA, 2011). The preceding equation can be rewritten for the case of dead and live load, in terms of the live-to-dead load ratio, L_m/D_m (Schmidt and Bartlett, 2002):

$$\phi = \delta_R \frac{\gamma_D + \gamma_L\left(L_m/D_m\right)}{\delta_D + \delta_L\left(L_m/D_m\right)} \exp\left(-\beta_T \sqrt{V_R^2 + V_Q^2}\right) \tag{35}$$

V_Q is calculated using Equation 36, and like Equation 35, it also varies with L_m/D_m (CSA, 2024):

$$V_Q = \frac{\sqrt{(\delta_D V_D)^2 + \left[\delta_L V_L (L_m/D_m)\right]^2}}{\delta_D + \delta_L (L_m/D_m)} \tag{36}$$

Work by others (e.g., Rudman et al., 2022) has demonstrated that approximate FORM and Monte Carlo simulation (MCS) yield a similar plot of ϕ versus L_m/D_m. MCS is widely regarded as the most accurate method for determining resistance factors, but it comes at the cost of added complexity and computation time. Thus, it makes sense to compare the SFA using different α-values to approximate FORM, and for the sake of this study, to assume that approximate FORM gives "correct" resistance factors.

The case studies are derived from Driver et al. (2006), Tayyebi and Sun (2021), Rudman et al. (2022), and Fidalgo and Packer (2022). These publications contain reliability analyses of specific steel components, and select values were extracted from each to be used in this study. The selected values are shown below in Table 6. Using the approximate FORM and the SFA as described above, ϕ-values were calculated for each column of parameters in Table 6, and the results are shown in Table 7.

Driver et al. (2006) and Tayyebi and Sun (2021) had $\beta_T = 4.5$ and $\beta_T = 2.6$, respectively, which are β-values for which optimal α-values were not calculated in the preceding recalibration. Thus, the optimal α-values for $\beta = 4.0$ and $\beta = 3.0$ were used for Driver et al. and Tayyebi and Sun, respectively. It should also be emphasized that $\beta = 2.6$ as used by Tayyebi and Sun corresponds to small-size, light-gage HSS and should not be used as a reliability index in applications pertaining to overall structural reliability.

Recall that the approximate FORM ϕ-values (henceforth denoted ϕ_{FORM}) are assumed to be the true ϕ-values

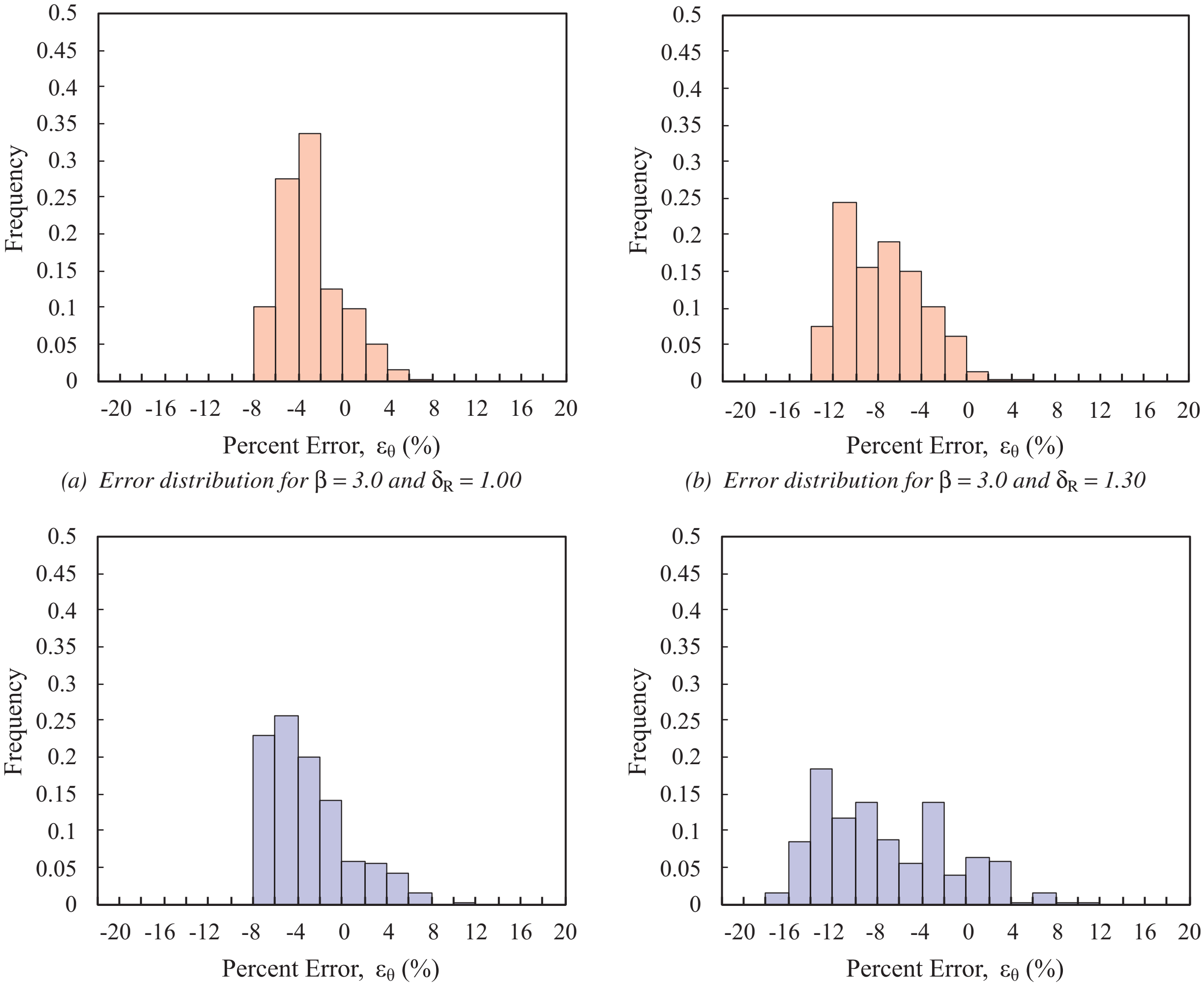

(a) Error distribution for $\beta = 3.0$ *and* $\delta_R = 1.00$

(b) Error distribution for $\beta = 3.0$ *and* $\delta_R = 1.30$

(c) Error distribution for $\beta = 4.0$ *and* $\delta_R = 1.00$

(d) Error distribution for $\beta = 4.0$ *and* $\delta_R = 1.30$

Fig. 7. Error distributions using new statistics and optimal α*-values.*

Table 6. Parameters from Case Studies

Variable	Driver et al. (2006)	Tayyebi and Sun (2021)	Rudman et al. (2022)	Fidalgo and Packer (2022)
V_D	0.10*	0.10*	0.10	0.10*
V_L	0.32*	0.32*	0.32	0.32*
V_R	0.091	0.237	0.247	0.335
β_T	4.5	2.6	3.0	4.0
γ_D†	1.2*	1.2	1.2	1.2*
γ_L†	1.6*	1.6	1.6	1.6*
δ_R	1.32	1.20	1.32	1.75
δ_D	1.05*	1.05*	1.05	1.05*
δ_L	0.78*	0.78*	0.78	0.78*

* Value was assigned for this study as it was not specified in the original study
† All values from ASCE 7 (ASCE, 2022)

Table 7. Resistance Factor Comparison

Method	Driver et al. (2006)	Tayyebi and Sun (2021)	Rudman et al. (2022)	Fidalgo and Packer (2022)
Approx. FORM ($L_m/D_m = 1.0$)	0.924	0.888	0.851	0.619
Approx. FORM ($L_m/D_m = 2.0$)	0.843	0.910	0.865	0.625
Approx. FORM ($L_m/D_m = 3.0$)	0.790	0.911	0.861	0.619
SFA(i)	1.054	0.855	0.878	0.838
SFA(ii)	0.991	0.780	0.786	0.685
SFA(iii)	0.932	0.733	0.730	0.560

in this study. A ϕ-value calculated using the SFA (henceforth denoted ϕ_{SFA}) is unconservative if it exceeds ϕ_{FORM} and is conservative if it falls below ϕ_{FORM}. All uses of conservative and unconservative will pertain to these definitions. Note that “slightly unconservative” isn’t necessarily problematic, and “more conservative” does not necessarily equate to “better.”

The results in Table 7 reinforce that the SFA generally requires a greater value of α_R to give conservative ϕ-values for higher reliability indices, which was originally demonstrated in the recalibration study. Both Driver et al. (2006) and Fidalgo and Packer (2022) had higher β_T and demonstrated that SFA(i) (i.e., $\alpha_R = 0.55$) yielded the least conservative ϕ_{SFA} of the three calibrations. Conversely, when $\beta_T \leq 3.0$, SFA(i)–SFA(iii) generally gave conservative results compared to approximate FORM (i.e., $\phi_{SFA} < \phi_{FORM}$), with SFA(i) giving the closest agreement.

V_R had a noticeable impact on the results, particularly on ϕ_{FORM}. When V_R is small (less than 0.10), ϕ_{FORM} varies noticeably with L_m/D_m, and when V_R is large (approaching or exceeding 0.30), ϕ_{FORM} varies minimally with L_m/D_m. Because ϕ_{SFA} does not vary with loading, this variation makes it more difficult for ϕ_{SFA} to agree with ϕ_{FORM} over a range of L_m/D_m when V_R is smaller.

To ensure that these observed trends are not anomalous, it is important to proceed with a more general approach to identify whether these conclusions hold over an array of cases.

Equating the SFA and Approximate FORM

The SFA and approximate FORM both serve the same purpose but are built on differing key assumptions: the former assumes that resistance alone determines reliability, while the latter assumes that both loading and resistance impact reliability. As such, ϕ_{FORM} and ϕ_{SFA} tend to differ for a given set of statistics; this was shown quite clearly in the previous subsection.

In this final study, the value of α_R is adjusted continuously such that $\phi_{SFA} = \phi_{FORM}$ over a specified range of V_R-values. The values of the other parameters utilized in this study are shown in Table 8. Note that the only significant difference between these values and the values used

Table 8. Data Variables for Equating the SFA and Approximate FORM

Variable	Value or Range
V_R	0.00–0.40
V_D	0.10
V_L	0.32†
γ_D††	1.2
γ_L††	1.6
δ_R	1.00
δ_D	1.05
δ_L	0.78†

† Value from Schmidt and Bartlett (2002)
†† Values from ASCE 7 (2022)

in the recalibration study (i.e., the Table 3 values) is that a wider range of V_R is utilized in this case, with the intent of capturing the behavior of the reliability methods outside the typical range (i.e., for values of V_R exceeding 0.30 and approaching zero).

As noted before, the typical range for the live-to-dead load ratio in many steel applications is $1.0 \le L_m/D_m \le 3.0$ (some studies extend the lower bound to zero). This range is often used to calculate and plot ϕ for a chosen β_T (or vice versa) using approximate FORM in modern reliability studies. Hence, this study considers $L_m/D_m = 1.0$, $L_m/D_m = 2.0$, and $L_m/D_m = 3.0$ as three discrete cases. Given the values in Table 8, V_Q is equal to 0.148, 0.195, and 0.223 for each L_m/D_m, respectively.

To determine values of α_R that establish equality between the SFA and approximate FORM, Equation 26a and Equation 35 (i.e., the equations for ϕ_{SFA} and ϕ_{FORM}) are equated and rearranged for α_R:

$$\alpha_R = \frac{-\ln\left[\dfrac{\gamma_D + \gamma_L\left(L_m/D_m\right)}{\delta_D + \delta_L\left(L_m/D_m\right)}\exp\left(-\beta\sqrt{V_R^2 + V_Q^2}\right)\right]}{\beta V_R} \tag{37}$$

Using Equation 37 and the values in Table 8, α-values were calculated over the specified range of V_R. Figures 8(a)–8(c) show the results for $\beta = 3.0$, $\beta = 3.5$ and $\beta = 4.0$, respectively, and the aforementioned L_m/D_m ratios.

In the Figure 8 plots, the dotted vertical line represents the limit on V_R indicated by Ellingwood et al. (1980), while the dashed horizontal line represents the indicated value of α_R (or α as indicated in the figures). For the value of V_R where the dashed line intersects one of the curves, the α-value corresponding to the dashed line will give equality between the SFA and approximate FORM at that L_m/D_m. When one of the curves falls above the dashed line, this means that a higher α-value than that indicated on the line is required for equality, and thus the SFA using the α-value on the line (0.55 for $\beta = 3.0$, 0.70 for $\beta = 3.5$, and 0.80 for $\beta = 4.0$) will give *unconservative* results (i.e., higher values of ϕ). When a curve falls below the line, the opposite is true: A lower α-value is required for equality, and the SFA using the α-value on the line gives *conservative* results (i.e., lower values of ϕ).

The α-values that represent the dashed lines displayed in Figures 8(a)–8(c) were chosen based on the results of the previous studies and by inspection of the plot trends. They represent the α-values that would somewhat minimize the magnitude of the error between ϕ_{SFA} and ϕ_{FORM} for each β, prioritizing the case of $L_m/D_m = 3.0$ (given by the blue curve) at which LRFD and ASD give equivalent structural reliability (AISC, 2022). This rationale assumes that the goal is to achieve the best agreement with approximate FORM, which is not necessarily the ideal result within the philosophy of SFA, as the aim of the SFA is to minimize the error in θ_a. However, considering the greater accuracy of approximate FORM, this approach is appropriate.

Figures 8(a)–8(c) both show that, as V_R approaches zero, the required α for equality diverges, beginning at around $V_R = 0.05$ for Figure 8(a) and $V_R = 0.10$ for Figures 8(b) and 8(c). Because the divergence approaches $+\infty$, the SFA becomes increasingly unconservative when using the α-value corresponding to the dashed line. This aligns with the observation made in the previous study: Because $V_R < 0.10$, the SFA gave unconservative values compared to approximate FORM.

The most prominent observation from the two previous studies is strongly supported by the results found here: that higher reliability indices warrant the use of higher values of α_R for use of the SFA. This and other observations are reflected in the following recommendation.

Recommendation

Based on the preceding findings, use of the SFA to calculate resistance factors for steel members and components is recommended as follows:

$$\phi = \begin{cases} \delta_R \exp(-0.55\beta V_R); & 0.05 \le V_R \le 0.30, \ \beta \approx 3.0 \\ \delta_R \exp(-0.70\beta V_R); & 0.10 \le V_R \le 0.40, \ \beta \approx 3.5 \\ \delta_R \exp(-0.80\beta V_R); & 0.10 \le V_R \le 0.40, \ \beta \approx 4.0 \end{cases} \quad (38)$$

The limits imposed on V_R ensure that the SFA will give satisfactory agreement with approximate FORM and prevent unconservative results. The scope of this work is limited to steel component reliability and a load case containing only dead and live loads, so the recommendation should be utilized accordingly. Beyond these limits, it is recommended to rely on more accurate reliability methods, such as approximate FORM or Monte Carlo simulation.

CONCLUSIONS

A comprehensive overview of the origin, initial derivation, and later development of the separation factor approach (SFA) has been summarized herein. From the amalgamation of this literature, it is found that the SFA was built on a few key simplifying assumptions that resulted in numerical

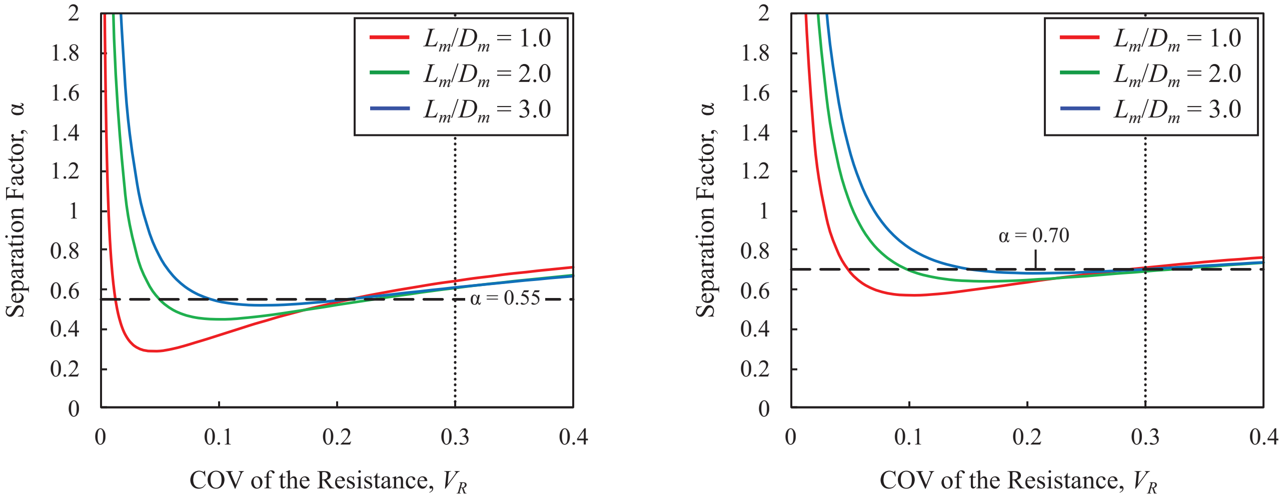

(a) $\beta = 3.0$

(b) $\beta = 3.5$

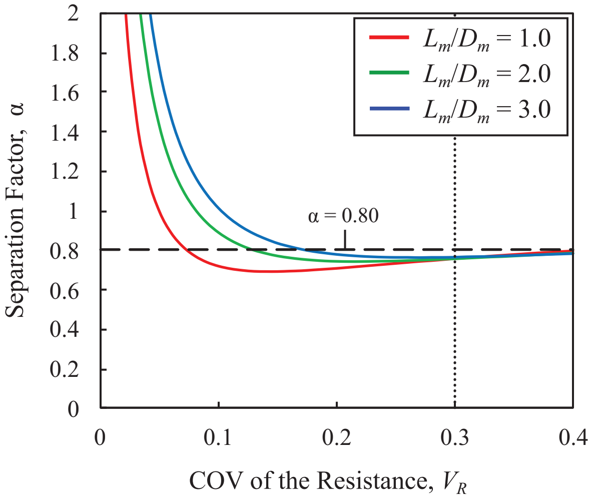

(c) $\beta = 4.0$

Fig. 8. Required separation factor for equality of the SFA and approximate FORM.

error of as much as 16% (underestimate) in the central safety factor, which contributes to the observed inaccuracy of the SFA in application. It is observed that the single constant separation factor, $\alpha = 0.55$, proposed by Galambos and Ravindra (1973) was not the optimal value according to the definition adopted by the SFA (i.e., minimization of the error in the approximation of the central safety factor) because it was calibrated to an atypical range of live-to-dead load ratios. Furthermore, it is found that the error in the approximation of the central safety factor can be better minimized if all separation factors (α_D, α_L, α_E, α_R) are varied independently of one another to determine an optimal combination. When this is performed using more up-to-date load and resistance statistics combined with a realistic range of live-to-dead ratios, it is found that a value of α_R ranging from 0.70 to 0.85 most effectively reduces the approximation error distribution.

Because the SFA uncouples the load and resistance terms while more accurate reliability methods do not, it should be expected that these methods will yield different resistance factors, even when both are used under optimal circumstances defined by their own assumptions. Despite this differing philosophy, separation factors can be calibrated such that the SFA will be in relative agreement with more accurate reliability methods under certain conditions. If agreement with more accurate reliability methods at $L_m/D_m = 3.0$ is the favored result, it is found that $\alpha_R = 0.55$, $\alpha_R = 0.70$, and $\alpha_R = 0.80$ give adequate results for reliability indices of 3.0, 3.5, and 4.0, respectively, over specified ranges of the coefficient of variation (COV) of the resistance, V_R, that prevent unconservative (overestimated) resistance factors. If accurate use of the SFA for calculating resistance factors for steel components is desired, the equation given in Equation 38 is recommended when operating within the specified limits of validity. This recommendation provides a basis for more definitive guidance on resistance factor determination in accordance with AISC 360 Section B3.1 Commentary.

ACKNOWLEDGMENTS

This work received financial support from the Natural Sciences and Engineering Research Council of Canada (NSERC) and was also funded in part by the Canadian Standards Association (CSA). The views expressed are those of the authors and do not necessarily reflect the views of CSA.

SYMBOLS

A	Random variable accounting for uncertainties in the transformation of dead load intensities into dead load effects
A_m	Mean of A
B	Random variable accounting for uncertainties in the transformation of live load intensities into live load effects
B_m	Mean of B
C	Random variable accounting for the uncertainties in the transformation of wind load intensities into wind load effects
C_m	Mean of C
D	Dead load effect
D_m	Mean dead load effect
D_n	Nominal dead load effect
E	Random variable accounting for uncertainties in structural analysis
E_m	Mean of E
F_U	Cumulative distribution function of U
L	Live load effect
L_m	Mean live load effect
L_n	Nominal live load effect
Q	Total load effect
Q_i	Constituent load effect
Q_m	Mean of the total load effect
Q_n	Nominal total load effect
R	Resistance
R_m	Mean resistance
R_n	Nominal resistance
T	Random variable denoting the total load on a member
T_m	Mean of the total load on a member
U	Standardized variate of Z
V	Coefficient of variation (COV)
V_A	COV of A
V_{AD}	COV of the dead load effect accounting for uncertainties in load transformation
V_B	COV of B
V_{BL}	COV of the live load effect accounting for uncertainties in load transformation
V_C	COV of C
V_{CW}	COV of the wind load effect accounting for uncertainties in load transformation

V_D	COV of the dead load effect
V_E	COV of E
V_L	COV of the live load effect
V_Q	COV of the total load effect
V_R	COV of the resistance
V_T	COV of the total load on a member
V_W	COV of the wind load effect
V_Z	COV of the safety margin
W	Wind load effect
W_m	Mean wind load effect
Z	Safety margin
Z_m	Mean of the safety margin
c_D	Deterministic influence coefficient that transforms dead load intensities into dead load effects
c_L	Deterministic influence coefficient that transforms live load intensities into live load effects
c_W	Deterministic influence coefficient that transforms wind load intensities into wind load effects
i	Subscript that can take on different load types (e.g., D, L, W)
p_F	Probability of failure
Φ	Cumulative distribution function of the standard normal distribution
α	Separation factor
α'	Intermediate separation factor
α_D	Separation factor for determining the dead load factor
α'_D	Intermediate separation factor for determining the dead load factor
α_E	Separation factor for determining the load factor accounting for the uncertainties in structural analysis
α'_E	Intermediate separation factor for determining the load factor accounting for the uncertainties in structural analysis
α_L	Separation factor for determining the live load factor
α'_L	Intermediate separation factor for determining the live load factor
α_Q	Separation factor for the total load effect
α_R	Separation factor for determining the resistance factor
α_T	Separation factor for the total load on a member
α_W	Separation factor for determining the wind load factor
β	Reliability index
β_T	Target reliability index
γ	Load factor
γ_i	Constituent load factor
γ_D	Dead load factor
γ_E	Load factor accounting for uncertainties in structural analysis
γ_L	Live load factor
γ_W	Wind load factor
δ	Bias coefficient
δ_D	Bias coefficient for the dead load effect
δ_L	Bias coefficient for the live load effect
δ_Q	Bias coefficient for the total load effect
δ_R	Bias coefficient for the resistance
ε_β	Percent error in the approximation of β
ε_θ	Percent error in the approximation of θ
ε_ϕ	Percent error between ϕ using the approximate FORM and ϕ using the SFA
$\overline{\varepsilon}$	Mean percent error
$\dot{\varepsilon}$	Median percent error
ε_{MAX}	Maximum percent error
ε_{MIN}	Minimum percent error
θ	Central safety factor
θ_a	Approximation of the central safety factor
σ	Standard deviation
$\sigma_{\ln Q}$	Standard deviation of the natural logarithm of the total load effect
$\sigma_{\ln R}$	Standard deviation of the natural logarithm of the resistance
σ_Q	Standard deviation of the total load effect
σ_R	Standard deviation of the resistance
σ_T	Standard deviation of the total load on a member
σ_Z	Standard deviation of the safety margin
σ_ε	Standard deviation of the percent error
υ	Coefficient of skewness (COS)
ϕ	Resistance factor

REFERENCES

AISC (2022), *Specification for Structural Steel Buildings*, ANSI/AISC 360-22, American Institute of Steel Construction, Chicago, Ill.

Allen, A.O. (1991), *Probability, Statistics, and Queueing Theory with Computer Science Applications*, 2nd Ed., Academic Press Professional, San Diego, Calif.

Allen, D.E. (1975), "Limit States Design—A Probabilistic Study," *Canadian Journal of Civil Engineering*, Vol. 2, No. 1.

Ang, A.H.-S. and Cornell, C.A. (1974), "Reliability Bases of Structural Safety and Design," *Journal of the Structural Division*, ASCE, Vol. 100, No. ST9, pp. 1,755–1,769.

ASCE (2022), *Minimum Design Loads and Associated Criteria for Buildings and Other Structures*, ASCE/SEI 7-22, American Society of Civil Engineers, Reston, Va.

Bartlett, F.M., Hong, H.P., and Zhou, W. (2003), "Load Factor Calibration for the Proposed 2005 Edition of the National Building Code of Canada: Statistic of Loads and Load Effects," *Canadian Journal of Civil Engineering*, Vol. 30, pp. 429–439.

Benjamin, J.R. and Cornell C.A. (1970), *Probability, Statistics, and Decision for Civil Engineers*, McGraw-Hill, New York, N.Y.

Cornell, C.A. (1969), "A Probability-Based Structural Code," *Journal*, American Concrete Institute, Vol. 66, No. 12, pp. 974–985.

CSA (1969), *Steel Structures for Buildings*, CSA S16-1969, Canadian Standards Association, Toronto, On.

CSA (2011), *Guidelines for the Development of Limit States Design Standards*, CSA S408-11, Canadian Standards Association, Toronto, On.

CSA (2019), *Canadian Highway Bridge Design Code*, CSA S6:19, Canadian Standards Association, Toronto, On.

CSA (2024), *Design and Construction of Steel Structures*, CSA S16:24, Canadian Standards Association, Toronto, On.

Driver, R.G., Grondin, G.Y., and Kulak, G.L. (2006), "Unified Block Shear Equation for Achieving Consistent Reliability," *Journal of Constructional Steel Research*, Vol. 62, pp. 210–222.

Ellingwood, B., Galambos, T.V., MacGregor, J.G., and Cornell, C.A. (1980), "Development of a Probability Based Load Criterion for American National Standard A58," *Special Publication 577*, National Bureau of Standards, Gaithersburg, Md.

Fidalgo, A. and Packer, J.A. (2022), "Evaluation of Bolted CHS Flange-Plate Connections under Axial Tension," *Journal of Constructional Steel Research*, Vol. 196, pp. 107399-1–102399-18.

Fisher, J.W., Galambos, T.V., Kulak, G.L., and Ravindra, M.K. (1978), "Load and Resistance Factor Design Criteria for Connectors," *Journal of the Structural Division*, ASCE, Vol. 104, No. 9, pp. 1,427–1,441.

Galambos, T.V. and Ravindra, M.K. (1973), "Tentative Load and Resistance Factor Design Criteria for Steel Buildings," Research Report No. 18, Civil and Environmental Engineering Department, Washington University, St. Louis, Mo.

Jeong, H. (1981), "Examination of Resistance Factor for Load and Resistance Factor Design Criteria," Master's Thesis, The Pennsylvania State University, State College, Pa.

Lind, N.C. (1971), "Consistent Partial Safety Factors," *Journal of the Structural Division*, ASCE, Vol. 97, No. ST6, pp. 1,651–1,669.

Melchers, R.E. and Beck, A.T. (2018), *Structural Reliability Analysis and Prediction*, 3rd Ed., Wiley, Hoboken, N.J.

Ravindra, M.K. and Galambos, T.V. (1978), "Load and Resistance Factor Design for Steel," *Journal of the Structural Division*, ASCE, Vol. 104, No. 9, pp. 1,337–1,353.

Rudman, D.F., Xi, Q., Packer, J.A., and Tousignant, K. (2022), "Reliability of HSS Cross Connections in Branch Axial Compression," *Engineering Journal*, AISC, Vol. 59, No. 4, pp. 313–336.

Schmidt, B.J. and Bartlett, F.M. (2002), "Review of Resistance Factor for Steel: Resistance Distributions and Resistance Factor Calibration," *Canadian Journal of Civil Engineering*, Vol. 29, pp. 109–118.

Tayyebi, K. and Sun, M. (2021), "Design of Direct-Formed Square and Rectangular Hollow Section Stub Columns," *Journal of Constructional Steel Research*, Vol. 178, pp. 106499-1–106499-14.

Thoft-Christensen, P. and Baker, M.J. (1982), *Structural Reliability Theory and Its Applications*, Springer-Verlag, New York, N.Y.

Xi, Q. and Packer, J.A. (2021), "Assessing the Probabilistic Assumptions behind Structural Reliability via Simulation," Canadian Society for Civil Engineering Annual Conference, Virtual, Canada, STR230.

Ziemian, R. (2010), *Guide to Stability Design Criteria for Metal Structures*, 6th Ed., Wiley, New York, N.Y.

Impact of Bolt Pretension on Bearing Strength for All-Steel Members and Composite Members

JIA-HAU LIU and MICHEL BRUNEAU

ABSTRACT

Bolted connections are widely used in steel structures, and their design for slip-critical resistance and bearing strength is well documented in past research and current standards. However, the physical behavior that explains how friction and bearing forces interact in a pretensioned bolted connection and how these forces evolve under axial deformation remains unclear. This paper investigates the influence of bolt pretension on bearing strength through finite element analyses of both all-steel and composite splices [the latter one, of the type that would be found in composite plate shear walls/concrete filled (C-PSW/CF)]. The analyses captured the behavior of bolted connection, showing significant reduction in friction forces as bolt hole elongation increased. A simplified free-body diagram with contact springs was then employed to explain the yielding and bending of bolts, the loss of clamping forces, and the thinning of plates (due to the Poisson ratio effect), all of which contribute to the reduction of friction as hole elongation increases. Additionally, the study examines how bolt pretension affects C-PSW/CF connections under compression, showing that concrete restricts hole deformation and allows friction forces to be sustained until the concrete cracks and deformation progresses.

Keywords: bolted connections, bolt pretension, composite plate shear wall/concrete filled, finite element analysis.

INTRODUCTION AND BACKGROUND

Bolted connections are widely used in steel structures due to their efficiency and ease of construction. The design of these connections is sometimes governed by two main limit states: slip-critical resistance and bearing strength. Since the plies in a bearing connection are required to be in firm contact, pretension may be applied in a bearing connection, not only in slip-critical connections, but also in bearing-type connections. The application of pretension induces friction between the bolts and steel plates, which complicates the understanding of how friction and bearing stresses contribute to the overall strength of the connection. Previous studies have investigated bearing-type bolted connections, contributing to the development of bearing strength parameters as outlined in current standards (Brown et al., 2007; Frank and Yura, 1981; Kim and Yura, 1996; Kulak et al., 1987; Lewis and Zwememan, 1996). According to the AISC *Specification for Structural Steel Buildings* (AISC, 2022b), hereafter referred to as the AISC *Specification*, the calculations for bearing strength and slip-critical resistance of a bolted connection are considered separately.

To compare the effect of bolt clamping forces, Frank and Yura (1981) conducted a series of tests for specimens with fully tensioned and not fully tensioned bolts for the bearing and net section failure type connections. The findings indicated that fully tensioned bolts exhibit a 10% higher capacity compared to snug-tightened bolts when failure is defined as the point when hole deformation is equal to 0.25 in. Note that the pretension in snug-tight bolts is not reported in these studies and that there is no upper limit on the pretension in a snug-tight bolt (although, technically, it should be low). However, no increase in capacity was observed when failure is defined in terms of ultimate load for the bearing-controlled connections. Kulak et al. (1987) compared earlier bearing test results from studies by Back and Bouwman (1959), Frank and Yura (1981), Hirano (1970), Jones (1958), and Nunse (1959). The test results indicated that the application of a clamping force somewhat increased the "ultimate bearing strength," suggesting partial load transmission through friction. Note that the "ultimate bearing strength" here refers to the failure loads observed during testing. Consequently, the "actual bearing strength" (i.e., the portion of the total bearing strength that is due to the contact stresses acting on a bolt hole) is lower than the "ultimate bearing strength" calculated based on the total applied load.

More recently, Može (2018) conducted a series of bearing tests on bolted connections with large end distances and bolt spacings and used finite element analysis to investigate the development of friction force during axial tensile

---

Jia-Hau Liu, Graduate Research Assistant, Department of Civil Structural and Environmental Engineering, University at Buffalo, Buffalo, N.Y. ORCID: https://orcid.org/0009-0003-9608-1932. Email: jiahauli@buffalo.edu (corresponding)

Michel Bruneau, SUNY Distinguished Professor, Department of Civil Structural and Environmental Engineering, University at Buffalo, Buffalo, N.Y. ORCID: http://orcid.org/0000-0003-1170-468X. Email: bruneau@buffalo.edu

Paper No. 2024-14

ISSN 2997-4720

loading of several single-bolt connections. The analyses also included a preloaded connection with a friction coefficient of 0.15 for comparison. Results from this latter analysis demonstrated that friction forces are generated between contact interfaces during axial loading, even without bolt pretension, and that these forces increase when the friction coefficient is greater. The friction forces in the preloaded connections showed no significant difference compared to those without preload once large deformations are developed. These analysis results provided evidence that both the forces in the bolt and the friction force stop increasing once the bolt has yielded.

Recent research conducted by Franceschetti and Denavit (2021) provides proposed formulas to evaluate tearout strength of bolted connections. The research summarized 471 specimens of single and multiple bolts in the database that failed in bearing and tearout. Among these specimens, only a few of them were fully pretensioned. This study also contains tension tests of 22 single-bolt butt splice connections with different hole types and edge distances. The test bolt was snug-tightened, and the plies were ensured to be in firm contact except for one specimen where grease was applied to the faying surfaces. The report observed that the greased specimen has a less stiff load-deformation curve compared to the snug-tightened specimen, and the strength of snug-tightened bolt at ¼ in. and ultimate deformation are 13% and 12% greater than the greased specimen.

To expand on this knowledge and better understand the behavior of bolted splices, research was conducted using finite element analysis to investigate the impact of bolt pretension on the bearing strength of bolted connections. The splice components considered as part of these analyses are steel bolted splice connections with single or double bolts, relying on the limit state of bolt bearing strength to resist the tension forces applied to the connected steel plates. The objective of these analyses was to capture the physical behavior of such connections under progressively increasing tension loading up to peak bearing strength, with a particular focus on understanding the evolution of the contribution of friction forces present between the splice plates due to bolt pretension. The subsequent discussion will highlight key factors that contribute to the reduction of clamping and friction forces in bolted splice connections as the applied loading is increased.

Additionally, the study explores the same behavior in bolted splices that would be used in composite plate shear wall/concrete filled (C-PSW/CF). This type of composite wall, which consists of two steel faceplates with a concrete core sandwiched between them, has been extensively investigated in past research (Agrawal, 2020; Alzeni, 2014; Alzeni and Bruneau, 2017; Kizilarslan, 2021; Kizilarslan and Bruneau, 2021, 2023; Sener and Varma, 2014; Shafaei et al., 2021; Varma et al., 2014), and is detailed in ASCE/SEI 7, *Minimum Design Loads and Associated Criteria for Buildings and Other Structures* (2022), the AISC *Specification* (2022b), and the AISC *Seismic Provisions for Structural Steel Buildings* (2022a). The national attention generated by implementations of C-PSW/CF in seismic regions has also led to interest for its use in nonseismic regions where bolted splices are preferred over welded splices. Consequently, numerical analyses have also been conducted to examine the effect of pretension on bearing strength in bolted composite splices.

FINITE ELEMENT MODELS

The section details the finite element models developed in LS-DYNA (Hallquist, 2006) to explore the relationship between friction and bearing in bolted connections for both all-steel and C-PSW/CF models.

All-Steel Bolted Connections

Analyses were first conducted on all-steel bolted connections. Figure 1 shows the geometries and finite element models of bolted splice connections relying on a single bolt or two bolts to transfer a tension loading applied to the steel plates, along with the reference coordinate system used for the analyses (X, Y, and Z directions). These models consist of faceplates, splice plates, and bolts (the term "faceplate" is used here by analogy with the splices in C-PSW/CF that will be addressed later). Table 1 outlines the geometries used in the finite element models considered. The table shows that the steel plate thickness, t (including faceplates and splice plates), and width, W, remain constant across all models. W_e is the net width of the connection, n denotes the number of bolts, d and d_h are the diameter of the bolt and the bolt hole, respectively, e is the edge distance from the bolt center to the plate edge, and S is the spacing between bolts. The term BR in the table refers to the bearing ratio, which can be expressed as shown in the following equation.

$$BR = \frac{A_e F_u}{ndtF_u} = \frac{W_e t F_u}{ndtF_u} = \frac{W_e}{nd} \tag{1}$$

Equivalently, BR can be defined as the net section area, A_e, divided by the total bearing area, ndt. Consequently, for a steel plate to have a net section rupture strength greater than a bearing strength of $3.0dtF_u$, the BR value must be larger than 3.0.

All steel (plates, bolts, etc.) was modeled using the plastic_kinematic (MAT_003) bilinear material model with kinematic hardening, as summarized in Table 2. In all the bolted connection models considered here, standard hole was used. The edge distance to bolt center, e, and center-to-center bolt spacing, S (as shown in Figure 1), have been chosen to prevent tearout being the controlling limit state.

Table 1. Geometries of Finite Element Models

Model	t (in.)	W (in.)	W_e (in.)	Rows	n	d_h (in.)	d (in.)	E (in.)	S (in.)	BR
1	0.375	6	4.875	1	1	1.125	1	4.00	—	4.875
2	0.375	6	4.875	2	2	1.125	1	4.00	4.00	2.438
3	0.375	6	5.188	2	2	0.8125	0.75	4.00	4.00	3.458
4	0.375	6	5.313	2	2	0.6875	0.625	4.00	4.00	4.250

Table 2. Material Properties for Steel Parts

Part	E_s (ksi)	Possion's Ratio	F_y (ksi)	F_u (ksi)	E_t (ksi)	β
Faceplates	29000	0.3	55	70	109	0.0
Splice plates	29000	0.3	55	70	109	0.0
Bolts/rods	29000	0.3	120	150	221	0.0

Using the AISC *Specification* (2022b), calculated strength for the limit states of bearing strength ($2.4dtF_u$ and $3.0dtF_u$), net section rupture strength (A_eF_u), gross section yielding strength (A_gF_y), and bolt shear strength are summarized in Table 3 for the finite element models considered. Single-bolt (Model 1) and double-bolt (Models 2–4) connections were considered. Three different bolt diameters were used in double-bolt connections (Models 2–4) to assess the influence of bending and shear deformation of bolts on the development of bearing strength. Except for Model 2 where net section failure occurs shortly after the onset of bearing deformations, all bolted connection models are governed by the bearing limit state.

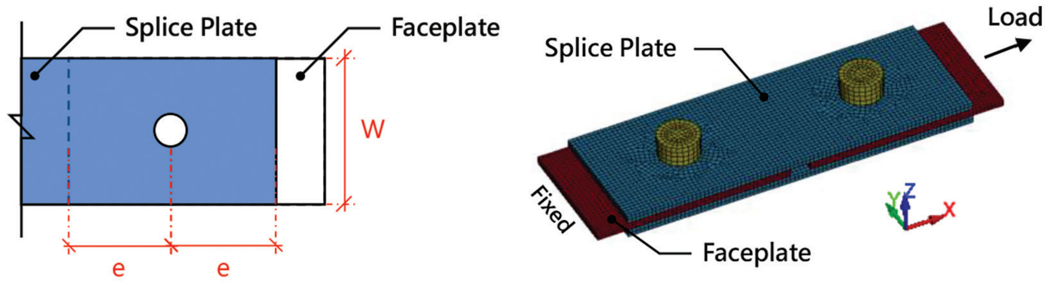

(a) Geometries and finite element model of single-bolt connection

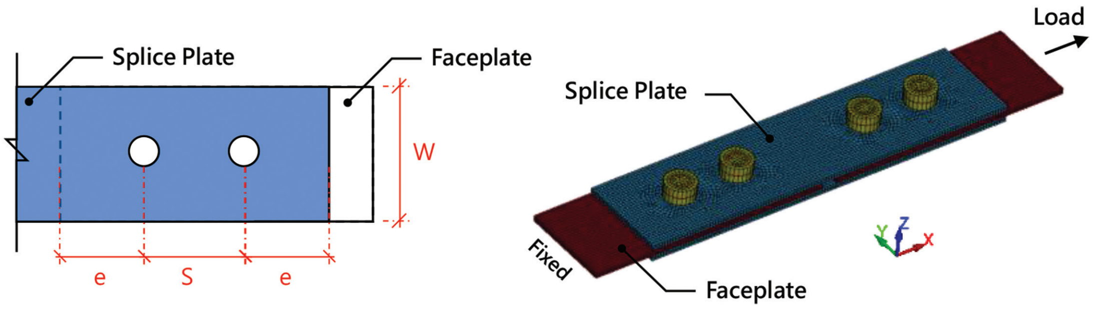

(b) Geometries and finite element model of double-bolt connection

Fig. 1. Finite element models.

Table 3. Design Limit States of Finite Element Models (Strength for Two Bolts in Cases 2, 3, and 4)

Model	A_eF_u (kips)	A_gF_y (kips)	$2.4dtF_u$ (kips)	$3.0dtF_u$ (kips)	Bolt Shear Strength (kips)	Governing Limit State
1	128	124	63.0	78.8	133	Bearing
2	128	124	126	158	265	Gross section yielding
3	136	124	94.5	118	149	Bearing
4	140	124	78.8	98.4	104	Bearing

For all finite element models analyzed, fixed boundary conditions were applied at one end, and a progressively increasing axial deformation was imposed at the other end to induce axial loading on the plates. Additionally, all bolts were preloaded to a stress equal to 105 ksi before any axial loading was applied to the plates. Figure 2 schematically shows the typical contact interfaces in the finite element models. These interfaces include the contact surfaces between steel plates, between bolts and steel plates, and between nuts and splice plates. All these contact interfaces in the analysis were specified using the automatic_surface_to_surface_mortar contact model with a static interface friction coefficient set to 0.3.

Bolted C-PSW/CF Connections

Three finite element models of bolted C-PSW/CF connections were built to study the clamping effect for bolted C-PSW/CF connections. Models T1 to T3, illustrated in Figures 3, 4, and 5, include the corresponding coordinate system (X, Y, and Z directions). These models consist of faceplates, splice plates, bolts or through rods with pipe-sleeves, tie bars, and infill concrete. The steel material model, contact model, and boundary constraints for these models were consistent with those used in the all-steel bolted connection models. The material properties for the steel elements in these bolted C-PSW/CF connection models are summarized in Table 4. The Winfrith concrete material model (MAT_085 in LS-DYNA) was used for concrete elements, as shown in Table 5.

The material model parameters include the elastic modulus, E_c, Poisson's ratio, the concrete compressive strength, f'_c, the concrete tensile strength, f_t, fracture energy, FE, and aggregate size, ASIZE. The same Poisson's ratio of 0.2 and aggregate size of 0.5 were used in all models. The material strengths of the steel plates and concrete were determined from 12 coupon tests and 15 concrete cylinder compressive tests, conducted during cyclic tension tests of the C-PSW/CF components with bolted splices (Liu and Bruneau, 2024). Table 6 provides information on the geometry of the bolted C-PSW/CF connections and includes details on the bearing ratio (BR), which ranges from 2.6 to 5.9 for the cases considered. The results from Models T1 and T2 are used to investigate friction development in scenarios where the connection is primarily governed by bearing strength. In contrast, Model T3 is utilized for comparison in situations where net section yielding occurs before the bearing strength of $2.4dtF_u$.

FRICTION FORCES IN STEEL BOLTED CONNECTIONS

Single-Bolt Connection (Model 1)

Figures 6(a) and 7(a) show the load-deformation curve obtained from the finite element analysis of Model 1 with and without applying bolt pretension. In these figures, deformation is measured from end-to-end of the model. The

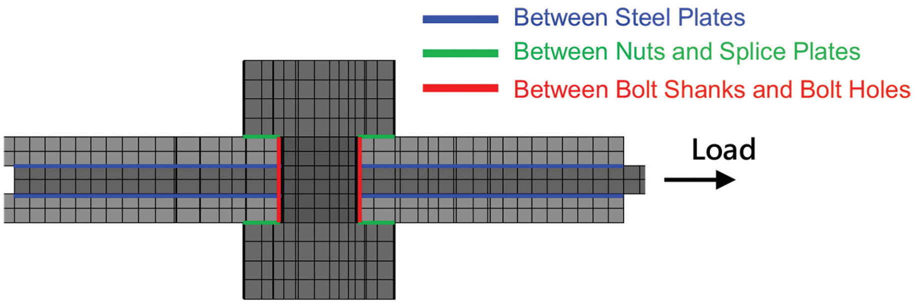

Fig. 2. Typical contact interfaces in the finite element model.

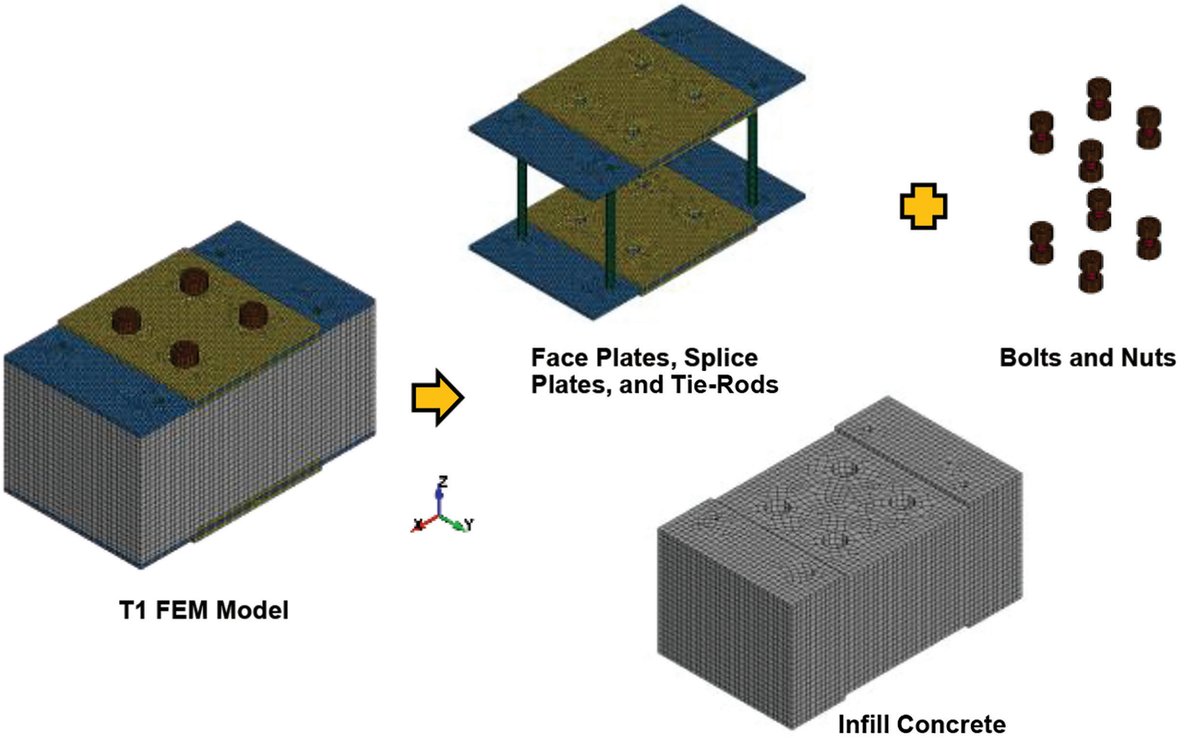

Fig. 3. Finite element model T1.

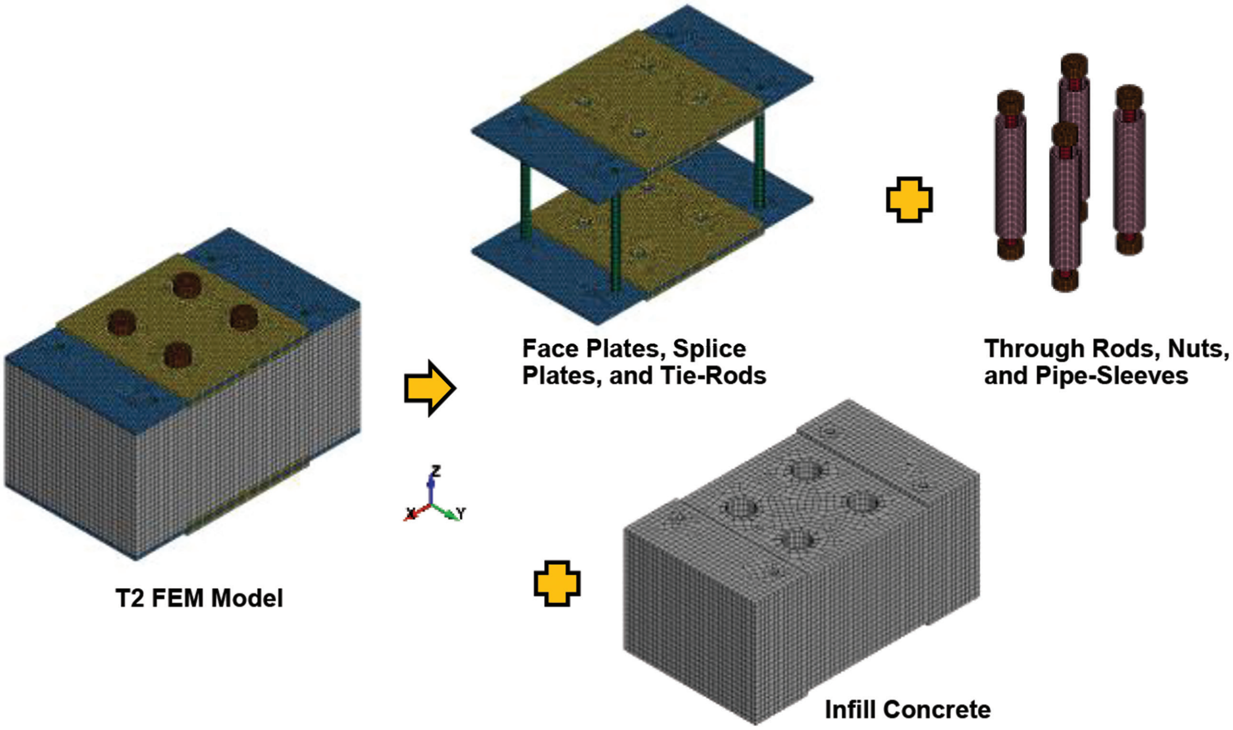

Fig. 4. Finite element model T2.

Table 4. Material Properties of Steel

Part	E_s (ksi)	Possion's Ratio	F_y (ksi)	F_u (ksi)	E_t (ksi)	β
Steel plates	29000	0.3	63.2	83.2	146	0.0
Bolts/rods	29000	0.3	120	150	221	0.0

Table 5. Material Properties of Concrete

Specimen	E_c (ksi)	Possion's Ratio	f'_c (psi)	f_t (psi)	FE	ASIZE
T1	4227	0.2	5500	550	0.00187	0.500
T2	4303	0.2	5700	570	0.00180	0.500
T3	4303	0.2	5700	570	0.00180	0.500

Table 6. Geometries of Models T1, T2, and T3

Specimen	t (in.)	W (in.)	W_e (in.)	Rows	n	d_h (in.)	d (in.)	e (in.)	S (in.)	BR
T1	0.375	14	11.750	1	2	1.125	1	4.00	—	5.875
T2	0.375	14	11.750	1	2	1.125	1	4.00	—	5.875
T3	0.375	14	9.875	1	3	1.375	1.25	4.00	—	2.633

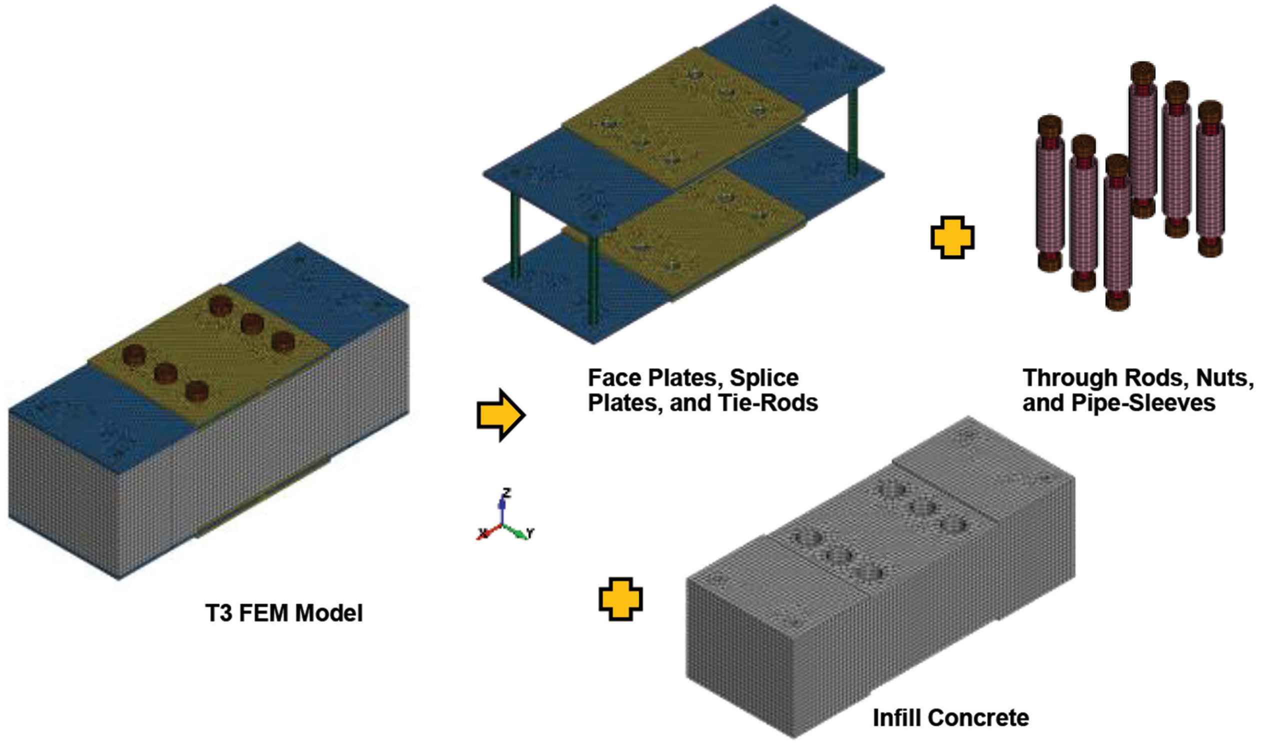

Fig. 5. Finite element model T3.

load-deformation curves compare the total axial force in the connection with the friction and bearing forces obtained from the contact interfaces. To evaluate the impact of the inelasticity of bolts on behavior, separate analyses were conducted, first with the material properties of the bolts modeled as elastic, and then using the inelastic bolt material properties listed in Table 2. Both results considering regular (i.e., inelastic) and elastic bolt material are shown in Figures 6(a) and 7(a).

For the bolted connection with bolt pretension (Figure 6), the preloaded stress is 105 ksi on 1-in.-diameter bolts, and the pretension force, T_b, is:

$$\begin{aligned} T_b &= \left(\frac{\pi}{4}\right)(1\text{ in.})^2(105\text{ ksi}) \\ &= 82.5\text{ kips} \end{aligned}$$

Therefore, the calculated slip resistance is:

$$\begin{aligned} 2(\mu T_b) &= 2(0.3)(82.5) \\ &= 49.5\text{ kips} \end{aligned}$$

The value is close to the numerically obtained initial friction (51.6 kips) marked in Figure 6(a). The effective area of bolt shanks, accounting for threads, and the D_u factor were omitted for simplicity in calculating slip-critical resistance. This simplification results in an approximately 15% overestimation of the slip-critical resistance based on AISC *Specification* Equation J3-4.

After the connection slid, the bearing force started to develop. It can be observed that as the bearing force and deformations increased, the friction force decreased simultaneously. At a deformation of 2.0 in., the maximum axial forces for regular and elastic bolt models reached 104 kips and 109 kips, while the maximum bearing forces reached 88.7 kips and 80.5 kips, respectively. The residual friction forces for regular and elastic bolt models were 17.5 kips and 30.4 kips at 2.0 in. deformation, representing 34% and 59% of the initial friction force, respectively. By comparing the regular and elastic bolt material, there is an approximate 25% loss (59% − 34%) of friction force due to the partial yielding of bolts.

For the bolted connection without bolt pretension, as shown in Figure 7(a), sliding occurred immediately after applying the axial load. After sliding, the bearing and friction forces developed simultaneously, with friction induced as a consequence of bearing. Similarly, the load-deformation curve shows the analysis results from both regular and elastic bolt models. The maximum axial forces in the regular and elastic bolt models reached 104 kips and 112 kips at 2.0 in. deformation, while the corresponding maximum bearing forces were 81.4 kips and 89.2 kips, respectively. The maximum friction forces reached 28.0 kips at 0.73 in. deformation and 37.6 kips at 1.03 in. deformation in the regular and elastic bolt models. The residual friction forces at 2.0 in. deformation were 16.2 kips and 32.2 kips in the regular and elastic bolt models, respectively, which are values nearly identical to the case with pretension.

Figures 6(b) and 7(b) show the relationship between total deformation (labeled "deformation") and hole elongation for Model 1 for the case of regular bolt material. Note that the vertical axis in these figures represents the sum of hole elongation from both sides of the splice. Both figures show

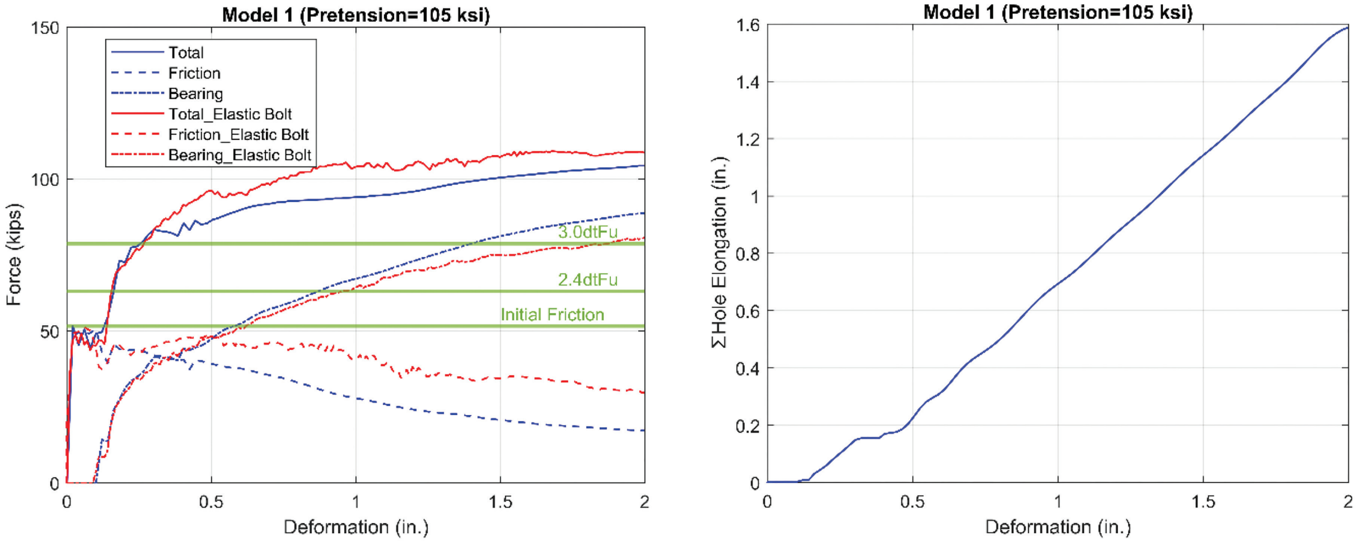

(a) Load-deformation curve

(b) Deformation vs. hole elongation

Fig. 6. Analysis result of Model 1 (with pretension).

that hole elongation contributed to approximately 80% of the total deformation (measured between the two ends of the model). With pretension (Figure 6), when the axial load reached the bearing strength of $2.4dtF_u$, the total deformation was 0.16 in, corresponding to sum of hole elongation of 0.03 in. When the bearing force alone reached $2.4dtF_u$, the total deformation was 0.87 in., corresponding to a sum of hole elongation of 0.6 in. For comparison, without pretension (Figure 7), at the same bearing strength of $2.4dtF_u$, the total deformation was 0.43 in, corresponding to a sum of hole elongation of 0.17 in. When the bearing force alone reached $2.4dtF_u$, the total deformation was 0.85 in., corresponding to a sum of hole elongation of 0.55 in. Sum of hole elongation of 0.55 to 0.6 in. corresponds to individual hole elongation of half those values. This suggests that without friction, the bolt hole elongation at the bearing strength of $2.4dtF_u$ in Model 1 is close to the 0.25 in. elongation observed in the tests by Frank and Yura (1981).

Further analysis of the results was performed to identify the causes for this progressive reduction in friction forces. Figure 8 shows the von Mises stress distribution in the connection at different deformation stages, illustrating the growth of the yielding "field" in the faceplate as hole elongation increases. Figure 9 shows typical deformations of this single-bolt connection at 2.0 in. deformation. The observed deformations in both figures around the bolt include hole elongation, thickness changes in the plates, and bending of plates and bolts.

A free-body diagram of the connection system showing contact springs is presented in Figure 10. In this diagram, nuts, splice plates, and faceplates are interconnected by contact springs, forming a system of springs in series. The spring constant is determined based on the stiffness factor, k_i, defined in the LS-DYNA theory manual (Hallquist, 2006). The stiffness factor, k_i, is given in terms of the bulk modulus, K_i, the volume, V_i, and the face area, A_i, in the contact interface. Based on the findings from Kizilarslan and Bruneau (2023) and Polat and Bruneau (2018), it was recommended that the contact stiffness in the model be set to 10 ($f_{si} = 10$) to prevent slippage of the concrete core under large deformations. Note there is no gap for the contact spring in the bolted connection studied here. Upon applying axial deformations to the connection, relative movements develop between the plates, and the faceplate undergoes substantial hole elongation, as illustrated in Figure 11. As this occurs, the initial contact spring loses contact area and contact stiffness due to hole elongation and thinning of the faceplate in tension due to Poisson's effect (Figure 12). Figure 13 highlights the thickness change around bolt holes in the spliced plate at three different positions (P1, P2, and P3, respectively located at the left, middle, and right end of the bolt hole), and Figure 14 shows the thickness change along with the axial deformation of the connection. These show an increase in the spliced plate thickness as it is compressed by the bolts in bearing. This increase in the thickness of the faceplate at the bolt bearing point increases the distance between the bolt head and the nut on that one side of each bolt, resulting in bolt bending and yielding (Figure 15). These factors collectively influence the behavior of the contact springs on both sides of the bolt. A net reduction in contact forces results in decreased clamping and friction forces. These behaviors contribute significantly to the reduction in friction observed across all finite element models.

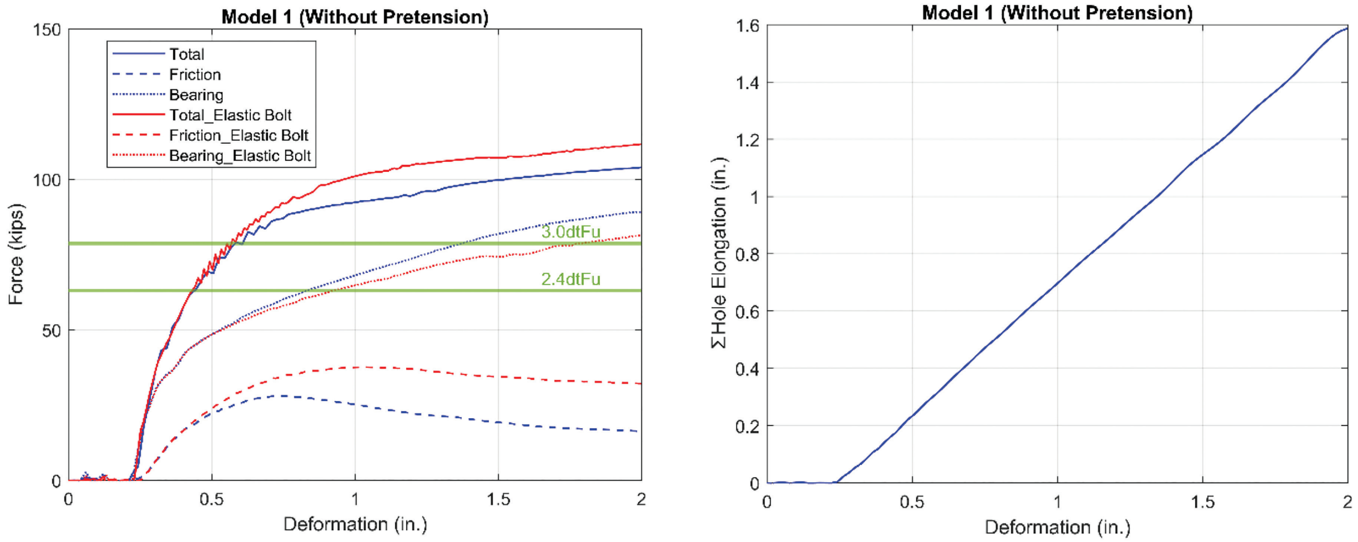

(a) Load-deformation curve

(b) Deformation vs. hole elongation

Fig. 7. Analysis result of Model 1 (without pretension).

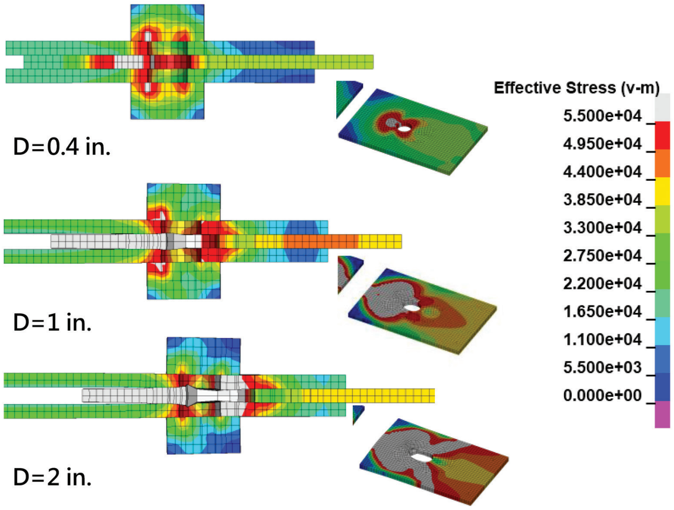

Fig. 8. Von Mises stresses of Model 1 at different deformations (bolt shank not shown).

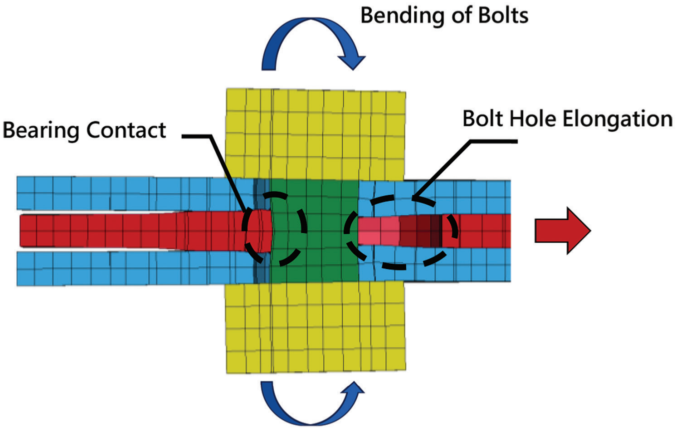

Fig. 9. Deformation around bolts of Model 1 (deformation = 2 in.).

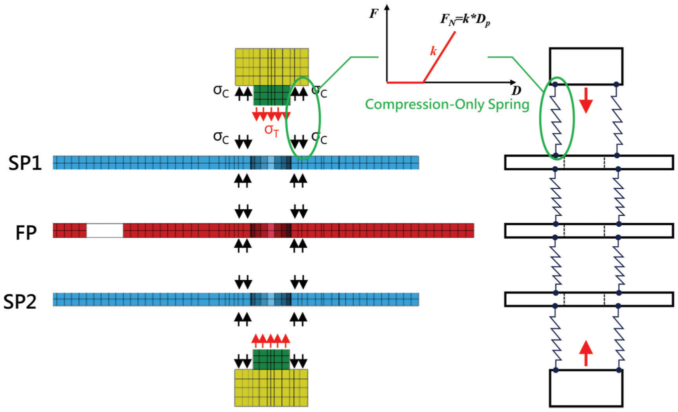

Fig. 10. Free-body diagram of spring system of bolted connections (preload stage).

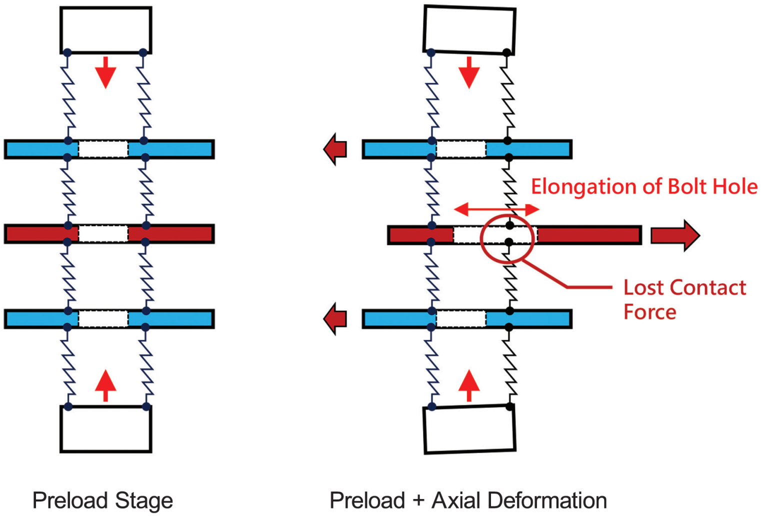

Fig. 11. Free-body diagram of spring system of bolted connections (preload and deformed stages).

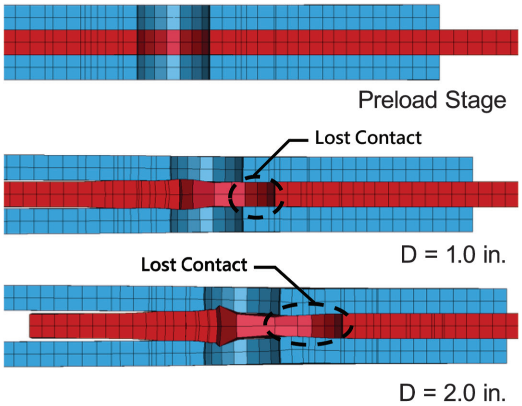

Fig. 12. Deformation of connection Model 1 (bolts not shown).

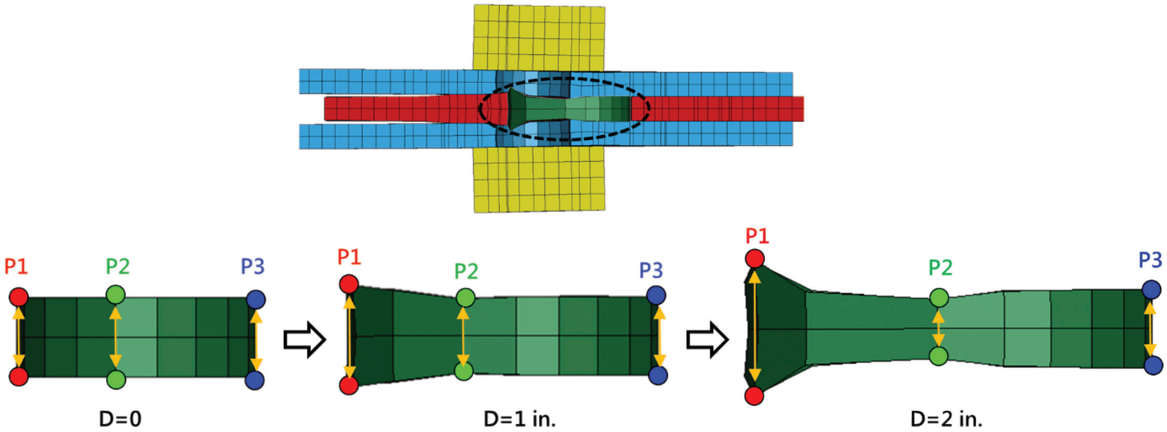

Fig. 13. Thickness change around bolt holes (Model 1).

Figure 16 shows the history of clamping stress vectors at different values of connection axial deformation. For the reasons mentioned earlier, the clamping stress vectors on the right (the side where the hole elongates in that figure) lost contact area and stiffness, resulting in a significant reduction in magnitude of the stress vectors with the application of axial deformation. Simultaneously, the thickness of the faceplate around the bolt hole became thinner there, leading to reduced clamping stresses around the bolt hole. Figures 17 and 18 show the 2D distribution of these clamping and friction stress vectors on a splice plate and the faceplate, respectively. Similarly, the clamping stress vectors are shown to significantly reduce as hole elongation increase. Figure 19 shows the variation in the clamping force and bolt tensile force as a function of bolt hole elongation. The clamping force decreased from initial value of 85 kips to 31 kips as the hole elongated to 0.8 in. deformation, and the axial force in the bolt correspondingly reduced by the same amount.

Double-Bolt Connection (Model 2 to Model 4)

As mentioned earlier, Models 2, 3, and 4 were used for investigating the clamping effect considering various bolt diameters (1 in., ¾ in, and ⅝ in. in Models 2, 3, and 4, respectively), with a *BR* ranging from 2.44 to 4.25. As previously noted in Figure 9, Model 1 exhibited some bolt bending behaviors. Consequently, there was interest in exploring

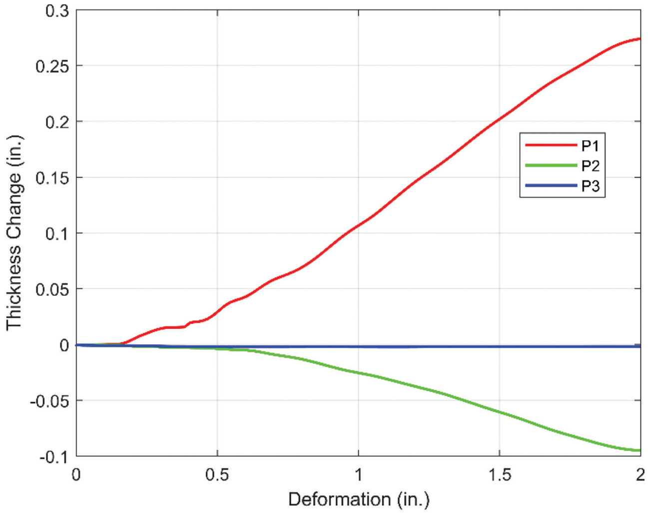

Fig. 14. Thickness change around bolt holes (Model 1).

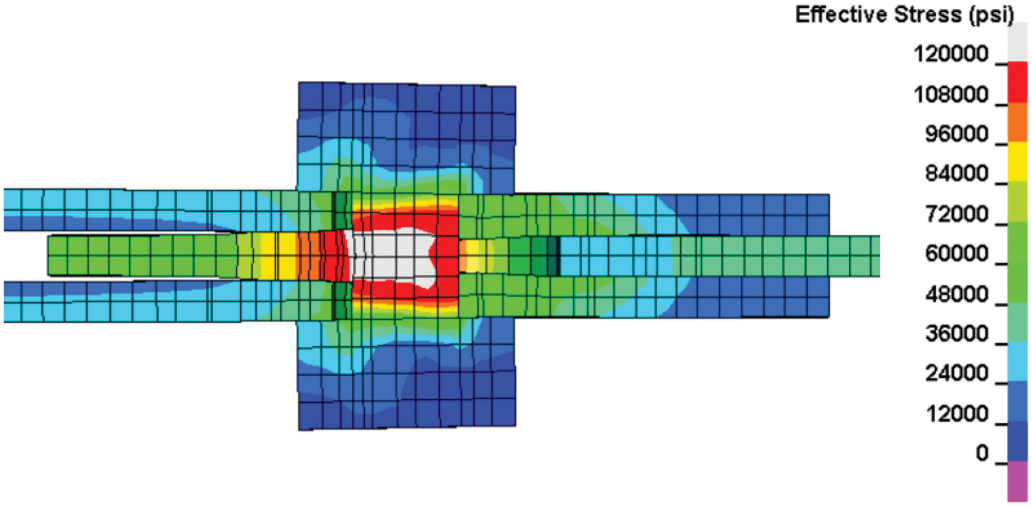

Fig. 15. Bending and yielding of bolts (Model 1).

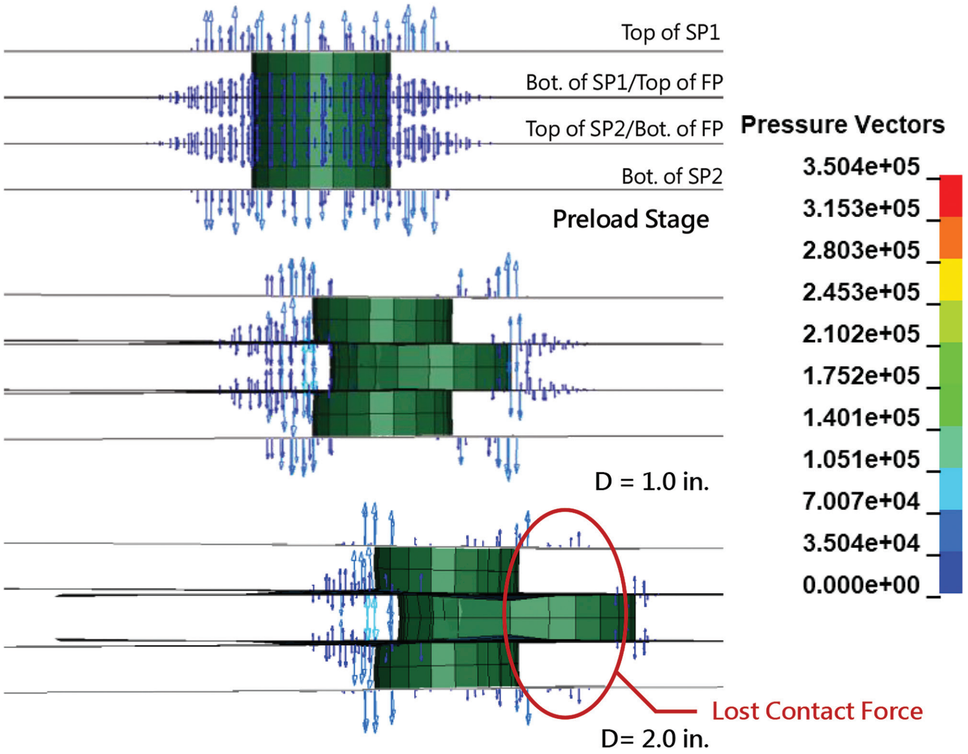

Fig. 16. Elevation views of contact interfaces showing clamping stress vectors (Model 1).

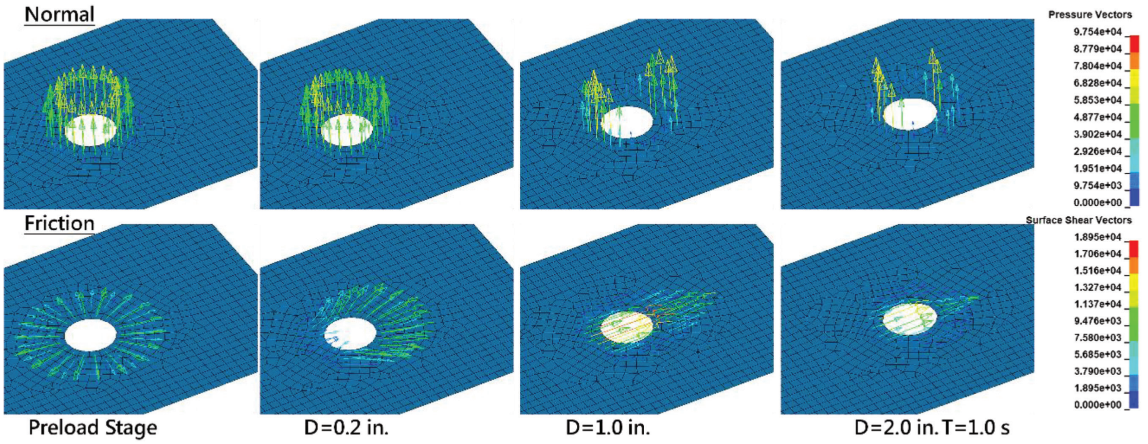

Fig. 17. Normal and friction stresses on the surface of the splice plate (Model 1).

this behavior under double-bolt connections in Models 2–4. The aim was to assess whether the bending of bolts will be mitigated in these configurations and to understand the influence on the development of friction. Figures 20–22 show the load-deformation curves of the finite element analysis for Models 2–4. Table 7 provides the calculated slip resistance for the models.

In Model 2 (Figure 20), the calculated slip resistance and numerically obtained initial friction force are 99.0 and 97.7 kips, respectively. After the connection slip, the bearing force started to develop, reaching its maximum value at the end of the analysis (arbitrarily stopped at 2.0 in. deformation). As mentioned in Table 3, the governing limit state in Model 2 is gross section yielding. Accordingly, the total axial force reached a plateau near 120 kips after 0.4 in. deformation, closely approaching the gross section yielding strength. The peak total axial force reached 125 kips at a deformation of 2.0 in., exceeding the gross section yielding strength of 124 kips and approaching the bearing strength of $2.4dtF_u$, set at 126 kips. At 2.0 in. deformation, the residual friction force is 40 kips, representing a 59% reduction compared to the initial friction force. When comparing Models 1 and 2, both featuring 1 in. bolt diameters and including single-bolt and double-bolt connections, it is observed that the residual friction in Models 1 and 2 is 34% and 41% of their initial friction force, respectively. This suggests that there is a greater reduction in friction in single-bolt connections compared to double-bolt connections under large bolt hole deformation due to bearing.

In Model 3 (Figure 21), the calculated slip resistance and numerically obtained initial friction force are 55.7 and 52.7 kips, respectively. The bearing force developed after connection slip, and it reached $2.4dtF_u$ at 0.8 in. deformation. Concurrently, the total axial force reached the bearing strength of $2.4dtF_u$ at a deformation of 0.23 in., and it achieved the bearing strength of $3.0dtF_u$ at a deformation of 0.89 in. The peak total axial force reached 127 kips at 2.0 in. deformation, which is larger than the gross section yielding strength of 124 kips. Meanwhile, the residual friction force was 18 kips, representing a 66% reduction compared to the initial friction force.

Finally, for Model 4 (Figure 22), the calculated slip resistance and initial friction force are 38.7 and 37.0 kips, respectively. The bearing force developed after connection slip, and it reached $2.4dtF_u$ and $3.0dtF_u$ at 0.51 and 0.81 in. deformations. Meanwhile, the total axial force attained the bearing strength of $2.4dtF_u$ at a deformation of 0.29 in., and it achieved the bearing strength of $3.0dtF_u$ at a deformation of 0.61 in. The peak total axial force attained 126 kips at 2.0 in. deformation, surpassing the gross section yielding strength of 124 kips. At that point, the residual friction force was 8 kips, representing a 78% reduction compared to the initial friction force. Table 8 compares Models 2–4, which have bolt diameters of 1.0, ¾, and ⅝ in., respectively. It lists the maximum axial forces at a 2.0 in. deformation as well as the initial and residual friction forces. Notably, the residual friction forces in Models 2–4 are 40, 18, and 8 kips, respectively, representing 41%, 34%, and 22% of their respective initial friction forces. The data show that smaller bolt diameters lead to greater reductions in friction due to their increased bending and shear deformations in bolted connections.

Figures 23–25 show the von Mises stresses distribution of these models at different deformation stages, highlighting the progressive yielding on the plates. As previously noted, the peak axial forces in Models 2–4 reached the

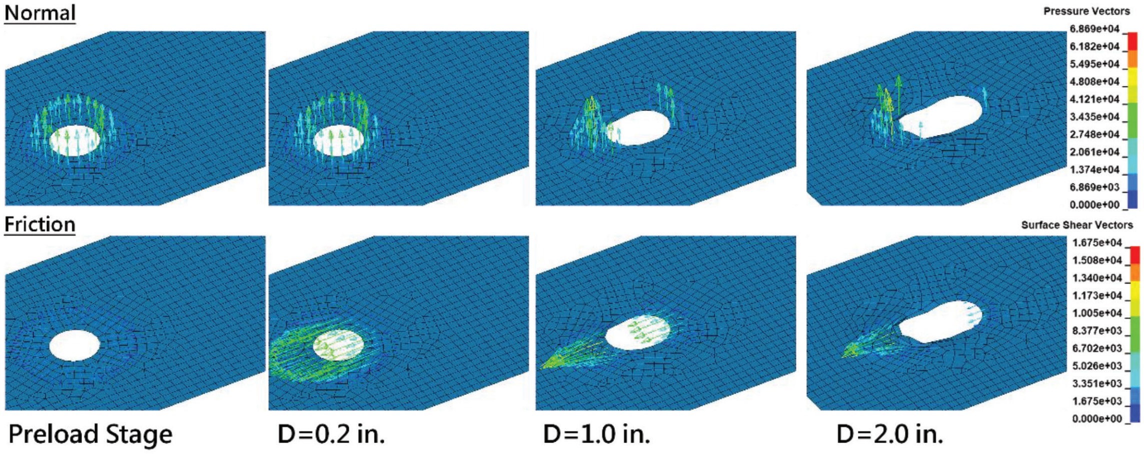

Fig. 18. Normal and friction stresses on the surface of the faceplate (Model 1).

gross section yielding strength, leading to observable whole section yielding around the inner bolts. In contrast, Model 1, which features a single-bolt connection and is shown in Figure 8, did not achieve its gross section yielding strength. In this model, yielding initiated around the bolt and extended toward the free edge, illustrating a different pattern of bearing stress distribution compared to the double-bolt connections.

Figure 26 shows the deformation of double-bolt connections (Models 2–4) at 2.0 in. deformation. Recall that these models have various bolt diameters, equal to 1, ¾, and ⅝ in. in Models 2, 3, and 4, respectively. It is noticeable that as the bolt diameter decreases, the bolt shanks exhibit more pronounced bending behavior (although, in Model 2, behavior was more dominantly governed by plate yielding rather than bolt bearing). Figure 27 shows the deformation of Model 3 (design governed by bearing) without showing the bolt shanks, providing a clearer view to observe the thickness change around bolt holes at locations identified as Bolt 1 and Bolt 2 in the figure. It can be observed that the bolt hole elongation is larger at location Bolt 1 (closer to the edge of splice plates), while the elongation is smaller at location Bolt 2 (closer to the center of the splice plates).

Recall from Figure 11, that as axial deformations are applied to the connection, relative movements occur between the plates, resulting in significant hole elongation in the faceplate. Figures 28–30 show the history of clamping stress vectors over axial deformation in Models 2–4. In the case of Model 2, where the design is governed by gross section yielding, the hole elongation of Bolt 2 is significantly less than that of Bolt 1. Therefore, the reduction of clamping stress vectors at Bolt 2 is less significant than at Bolt 1. Conversely, in Models 3 and 4, where the design is governed by bearing with smaller diameters of bolts, the bolts experience more bending, and the bolt holes have larger elongations, resulting in a more significant loss of clamping stress vectors. This phenomenon can also be observed by plotting the clamping force to hole elongation curves as shown in Figures 31–33. Also, the same conclusions were found by observing the clamping and friction stress vectors on the splice plate and faceplate as shown from Figures 34–39.

FRICTION FORCES IN BOLTED C-PSW/CF CONNECTIONS

Bolted C-PSW/CF Connections in Tension

Six cyclic C-PSW/CF components with bolted splices were tested by Liu and Bruneau (2024) to investigate the cyclic axial behavior of such splices in composite members. Results from the three specimens (T1–T3), for which bearing strength was the governing limit state, have been used here for comparison with the finite element analyses to investigate the impact of bolt pretension in this application.

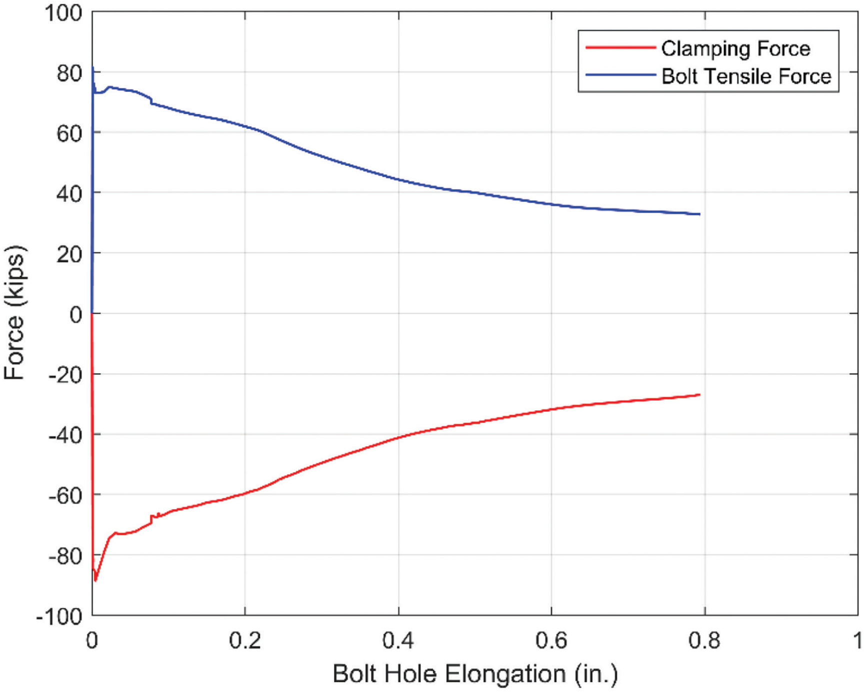

Fig. 19. Clamping force and bolt hole elongation curve (Model 1).

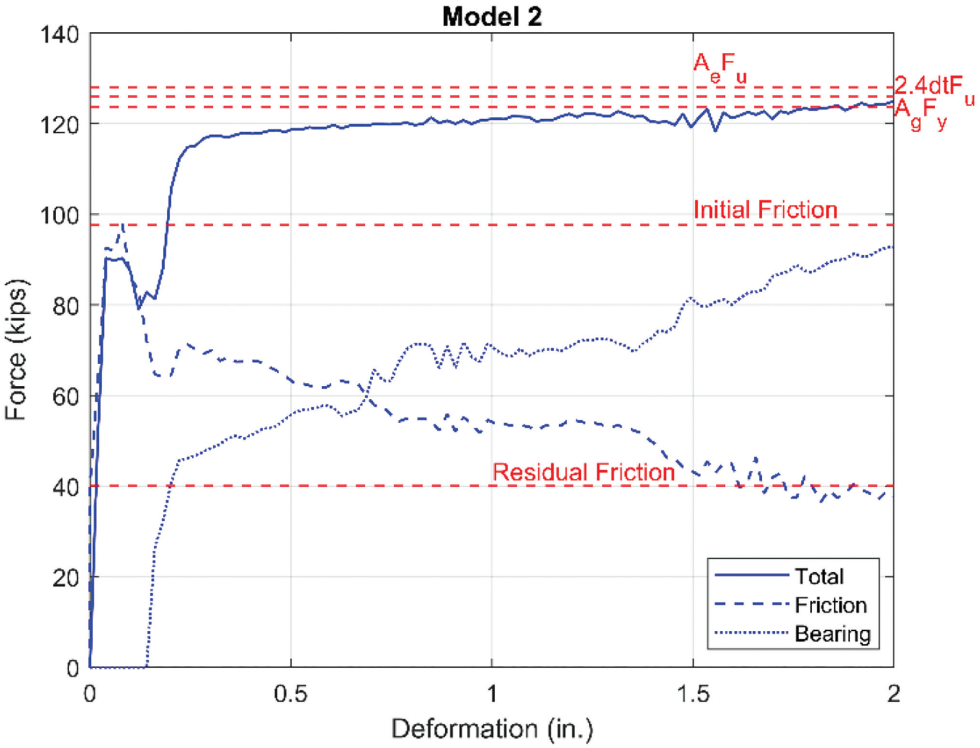

Fig. 20. Total axial force and friction force of Model 2.

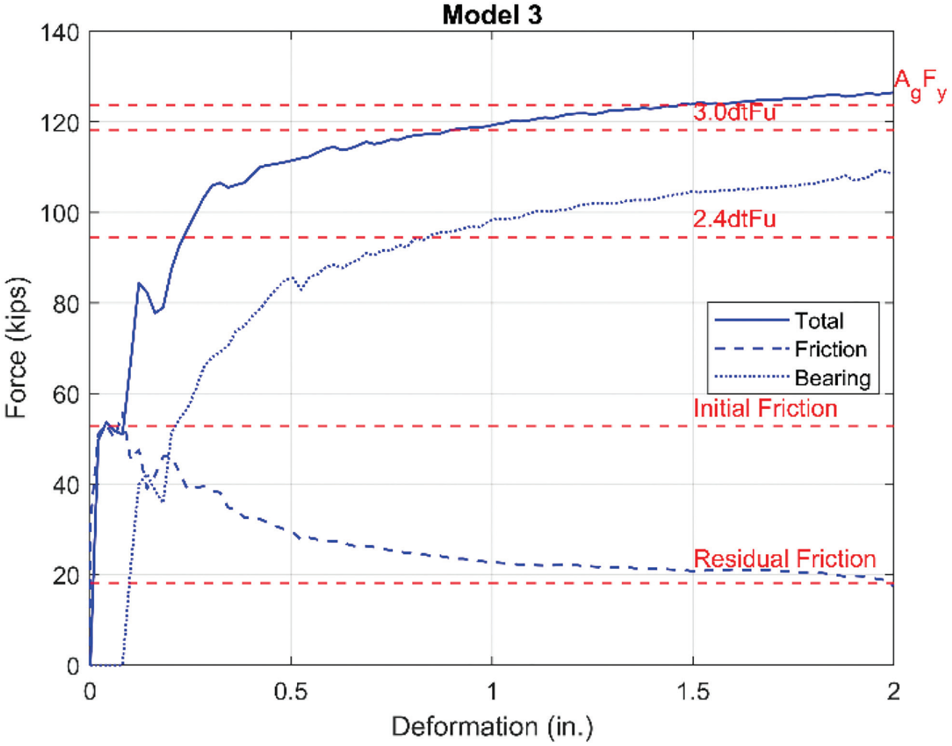

Fig. 21. Total axial force and friction force of Model 3.

Table 7. Calculated Slip Resistance for Models 2, 3, and 4

Model	Pretension T_b (kips)	Slip Resistance (kips)
2	82.5	99.0
3	46.4	55.7
4	32.2	38.7

Table 8. Initial and Residual Friction Forces in Models 2, 3, and 4

Model	Maximum Axial Force (kips)	Initial Friction Force (kips)	Residual Friction Force (kips)
2	125	97.7	40.0
3	126	52.7	18.0
4	125	37.0	8.0

Figures 40–42 present analysis results for Models T1–T3 (defined previously), showing the total axial forces and friction forces as a function of axial deformation. In these figures, the blue lines represent the results obtained from cyclic tension tests of the CPSW/CF components with bolted splices (Liu and Bruneau, 2024). The FEM analysis considers different pretension values in the bolts or through rods of the C-PSW/CF connections, with corresponding test results included in the figures. More specifically, the analyses of Models T1–T3 consider three pretension stress values—namely, 0 ksi (no pretension), 52.5 ksi (50% pretension), and 105 ksi (full pretension). These values correspond to axial forces of 0, 41.23 kips, and 82.5 kips for the 1-in.-diameter bolts/rods used in Models T1 and T2, and 0, 64.4 kips, and 129 kips for the 1¼-in.-diameter rods used in Model T3.

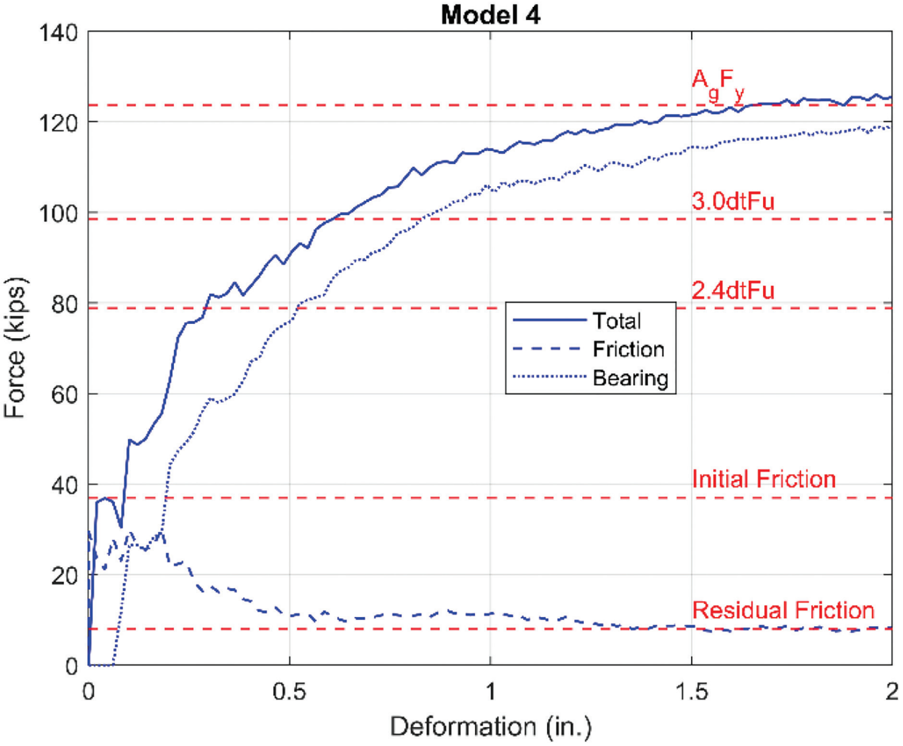

Fig. 22. Total axial force and friction force of Model 4.

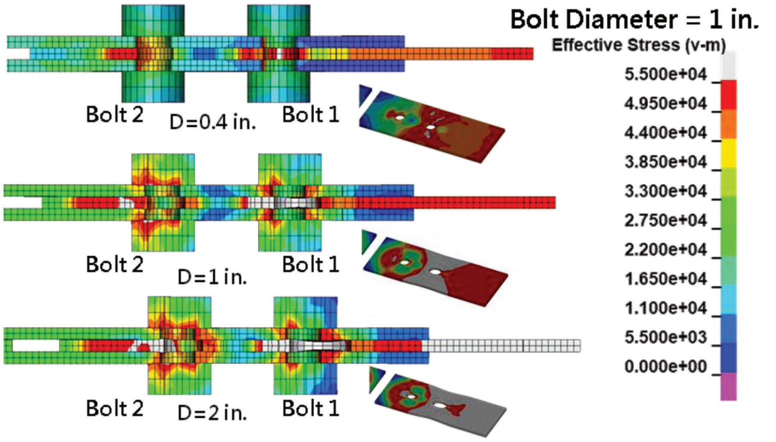

Fig. 23. Von Mises stresses of Model 2 at different deformations (bolt shank not shown).

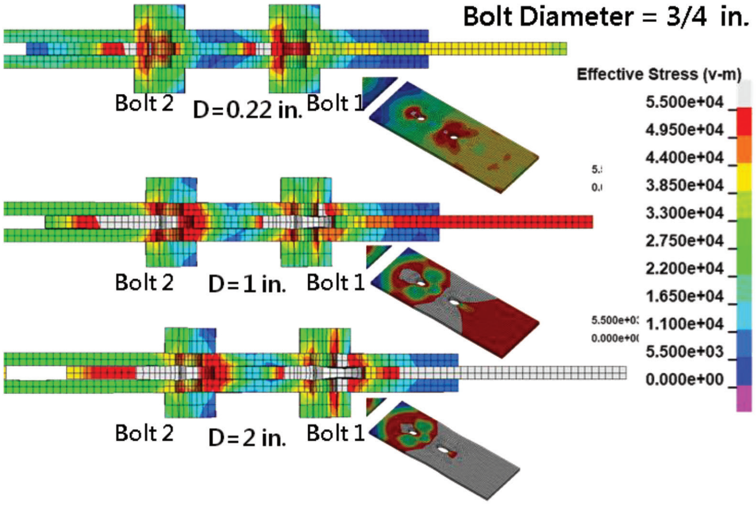

Fig. 24. Von Mises stresses of Model 3 at different deformations (bolt shank not shown).

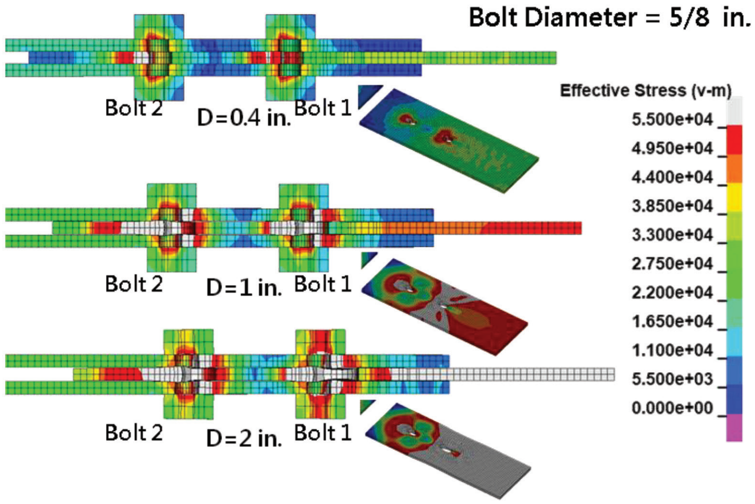

Fig. 25. Von Mises stresses of Model 4 at different deformations (bolt shank not shown).

The behaviors of steel bolted connections and C-PSW/CF bolted connections in tension show similarities. In both types, the bearing force begins to develop after connection slip, and the friction force starts decreasing following the development of the bearing force. In Models T1 and T2 (bearing-controlled case), the total axial forces reached $2.4dtF_u$ and $3.0dtF_u$ at axial deformations of approximately 1.3 and 1.2 in., regardless of the applied pretension values. For Model T3 (net section yielding-controlled case), the peak axial load reached net section yielding strength A_eF_y at deformations of 0.2, 0.55, and 0.82 in., for the cases of bolts pretensioned to values of 105, 52.5, and 0 ksi, respectively. The axial loads in the models plateaued after reaching net section yielding. Subsequently, regardless of pretension values, the axial load reached the bearing strength of $2.4dtF_u$ at deformation of 1.5 in.

While the curves indicate a significant drop in friction forces as axial deformation increases, regardless of the initially assigned pretension value, it can be observed there is no significant difference in the residual friction forces among each model under large axial deformation of connections—that is, when the connections reach their maximum bearing strength. Figure 43 shows the development of clamping stress vectors in Model T2, exhibiting a reduction behavior similar to the one described in the case of pure steel bolted connections. Figure 44 shows the clamping force versus bolt hole deformation curve for Models T1–T3, each under a pretension value of 52.5 ksi. The initial clamping forces for Models T1–T3 are 38, 38, and 55 kips,

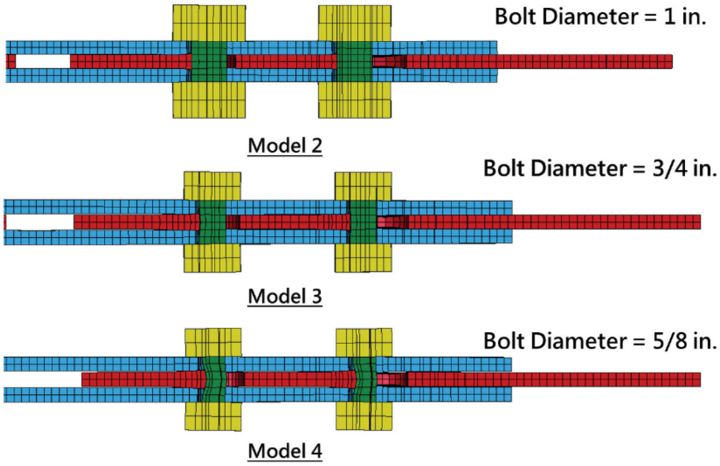

Fig. 26. Deformation of double-bolts connections (deformation = 2.0 in.).

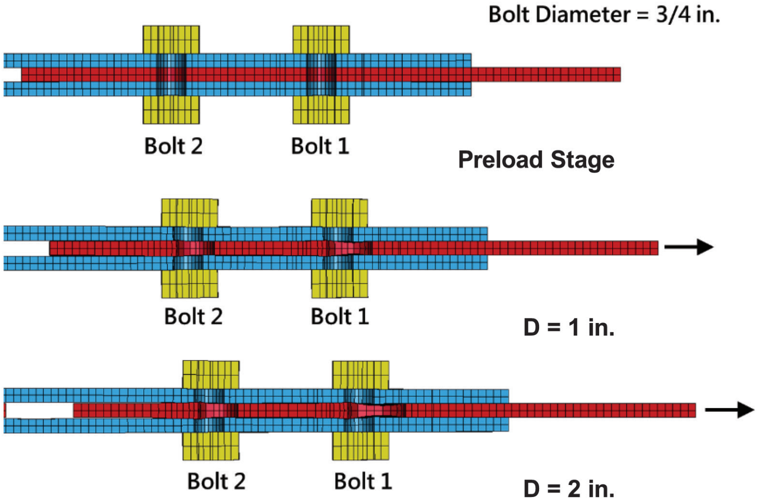

Fig. 27. Deformation of connection Model 3 (bolts shank not shown).

while the residual clamping forces are 16, 18, and 30 kips, respectively, representing 42%, 47%, and 55% of the initial clamping force. Models T1 and T2 show similar reductions in clamping force, likely due to having identical bolt numbers and diameters. Model T3 exhibits a smaller reduction in clamping force, likely due to its lower *BR*.

Bolted C-PSW/CF Connections in Compression

When a C-PSW/CF bolted connection is in compression, the high strength and stiffness of concrete contribute significantly to the axial load capacity. Model T1 was chosen to numerically explore the friction force that develops in the bolted splice region between the steel components as well as between the steel and concrete when the C-PSW/CF connection is in compression. The pretension value of this model was set at 55 ksi for 1-in.-diameter bolts. To simulate the lateral confinement in real wall scenarios, an additional side restraint was applied to the models.

Figure 45 shows the load-deformation curves obtained from the finite element analysis of Model T1 in compression in terms of the total axial force, the axial force in steel, and the axial force in concrete. The steel plates started sliding at a deformation of −0.01 in, corresponding to an axial load in the steel equal to 100 kips (labeled as P_1 in the figure), and the concrete resisted 261 kips (70% of the total axial load). At this point, the total axial load, P_{T1}, reached −372 kips. For comparison, the theoretical axial load in steel and concrete, P_{S1} and P_{C1}, predicted using relative elastic stiffness are:

$$\text{PT1} = -372 \text{ kips} \tag{2}$$

$$P_{S1} = P_{T1}\frac{E_s A_s}{E_s A_s + E_c A_c} = -85.6 \text{ kips} \tag{3}$$

$$P_{C1} = P_{T1}\frac{E_c A_c}{E_s A_s + E_c A_c} = -286 \text{ kips} \tag{4}$$

where the Young's modulus of steel and concrete, E_s and E_c, are equal to 29,000 ksi and 4,227 ksi, respectively, and the area of steel and concrete, A_s and A_c, are 7 in.^{2} and 161 in.^{2}, respectively.

The member axial stiffness did not change significantly after sliding of steel plates started, and the concrete alone resisted the additional axial load. At a deformation of −0.04 in, when the total axial load reached −993 kips (labeled as P_2 in Figure 45), some concrete cracks were observed at this point as the infill concrete elements reached its compressive strength (5,500 psi), as shown in Figure 46, leading to a significant change in axial stiffness. At that point, the concrete resisted −871 kips, which is 88% of the total applied axial load. Peak strength for the connection

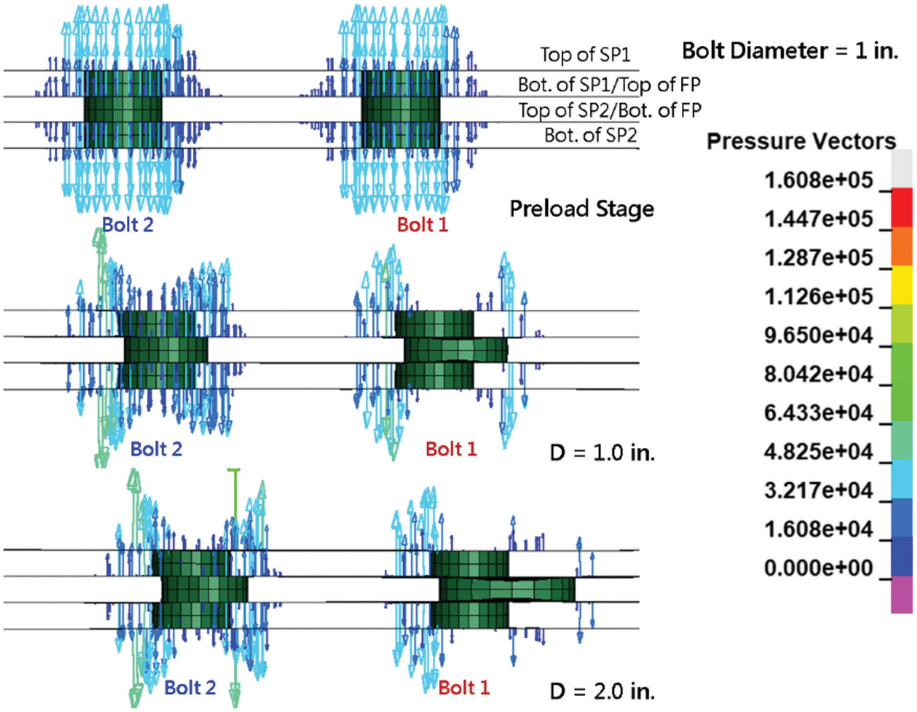

Fig. 28. Elevation views of contact interfaces with clamping stress vectors (Model 2).

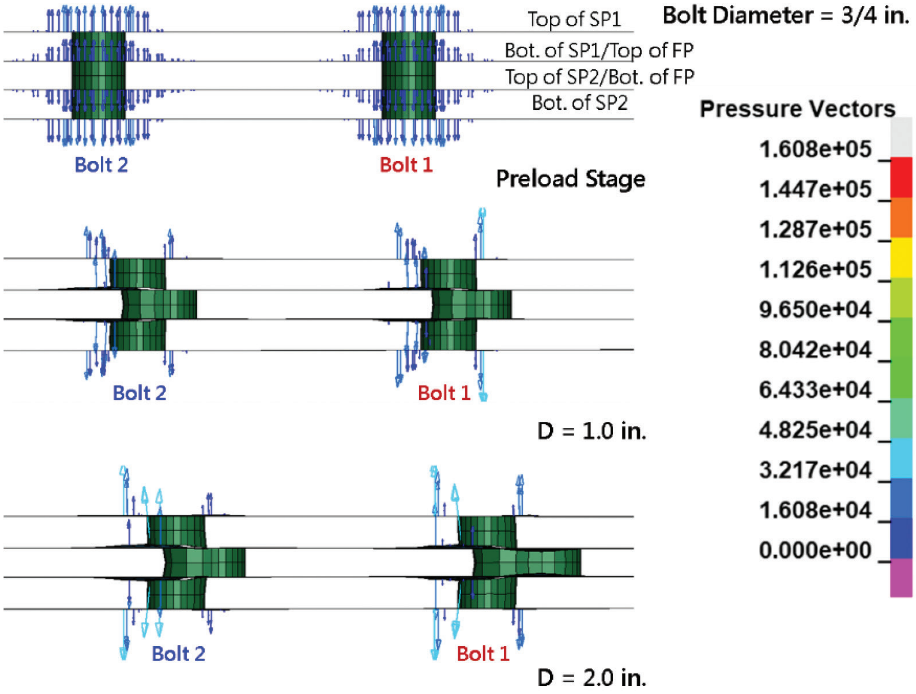

Fig. 29. Elevation views of contact interfaces with clamping stress vectors (Model 3).

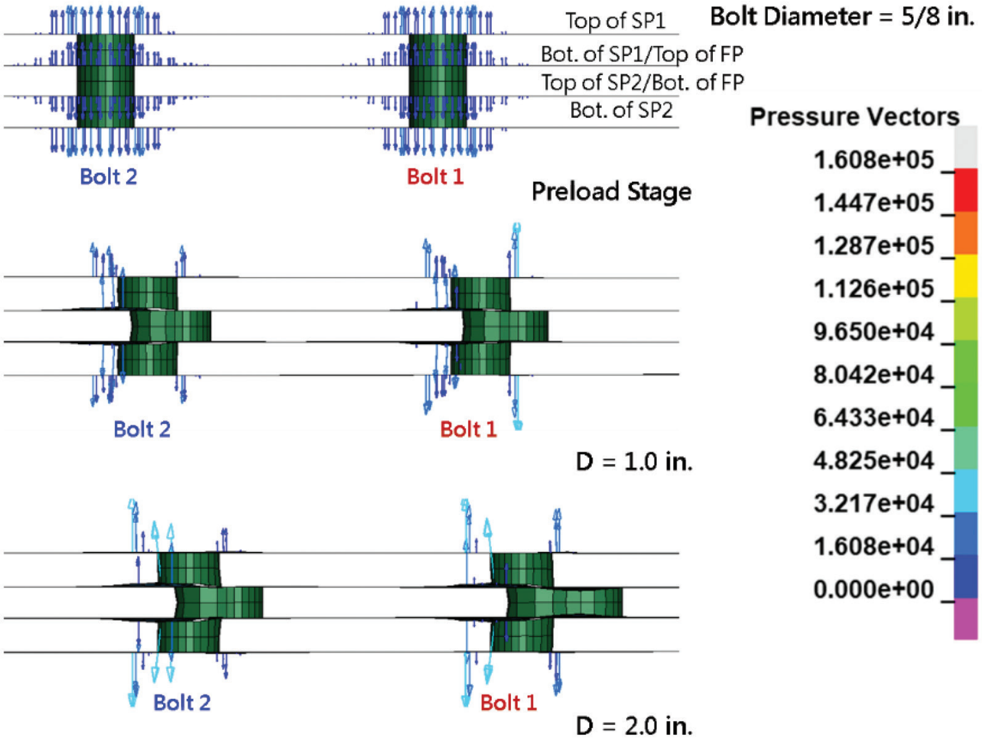

Fig. 30. Elevation views of contact interfaces with clamping stress vectors (Model 4).

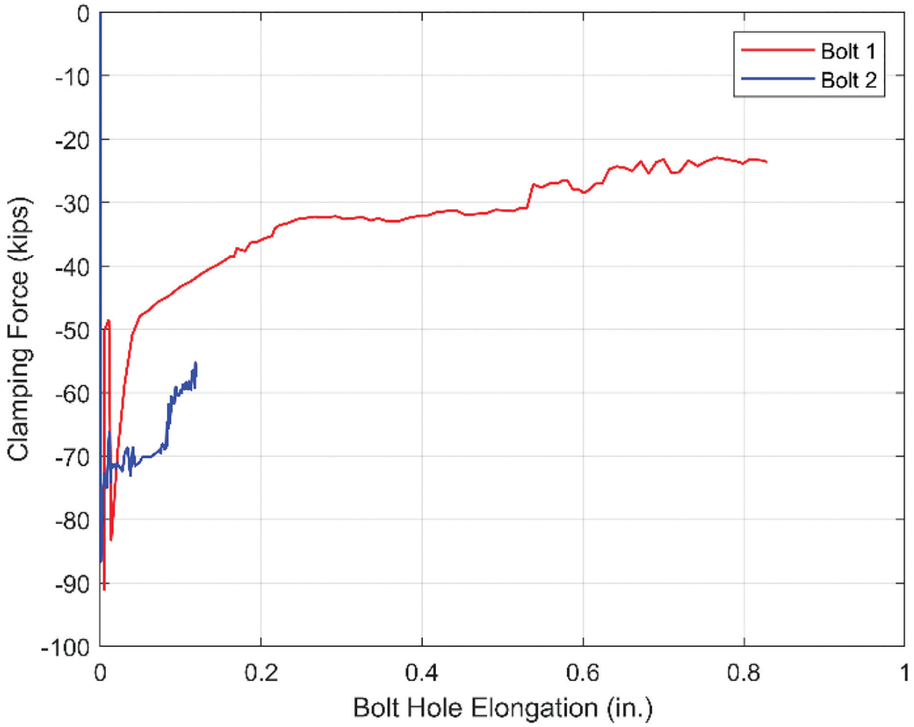

Fig. 31. Clamping force and bolt hole elongation curve (Model 2).

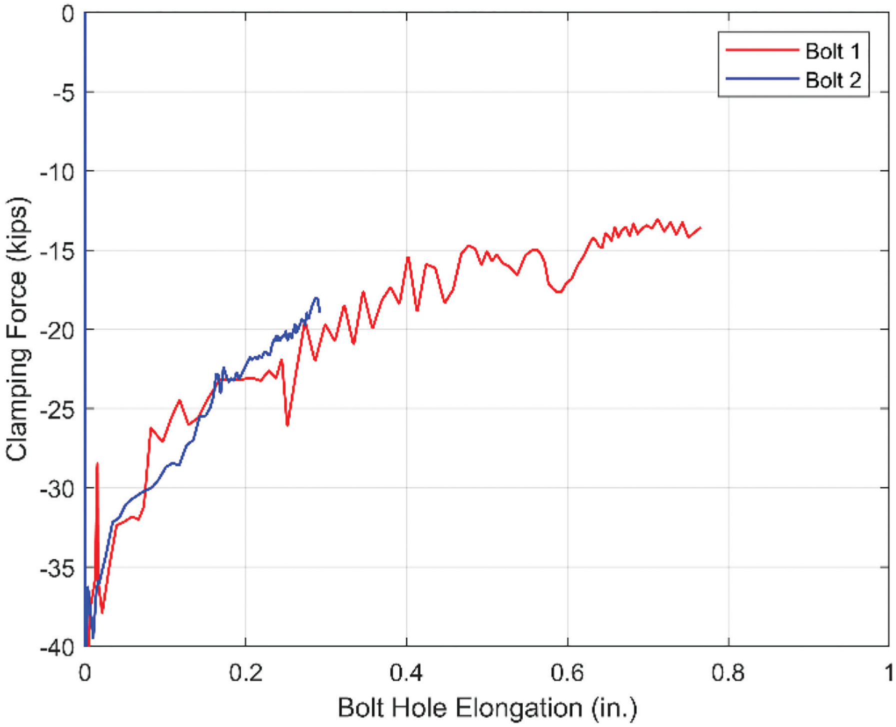

Fig. 32. Clamping force and bolt hole elongation curve (Model 3).

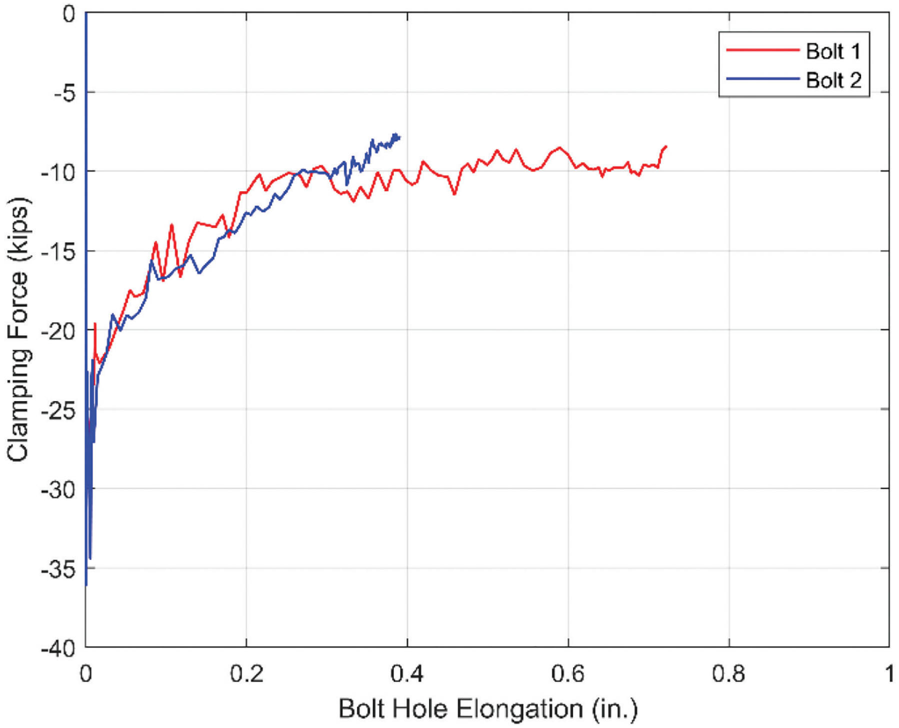

Fig. 33. Clamping force and bolt hole elongation curve (Model 4).

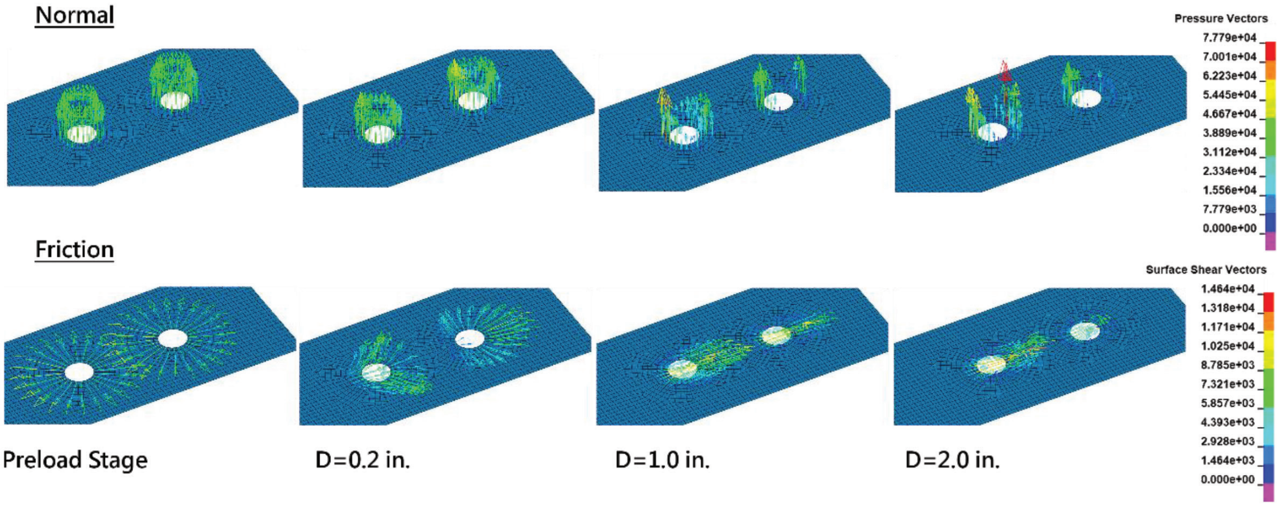

Fig. 34. Normal and friction stresses on the surface of the splice plate (Model 2).

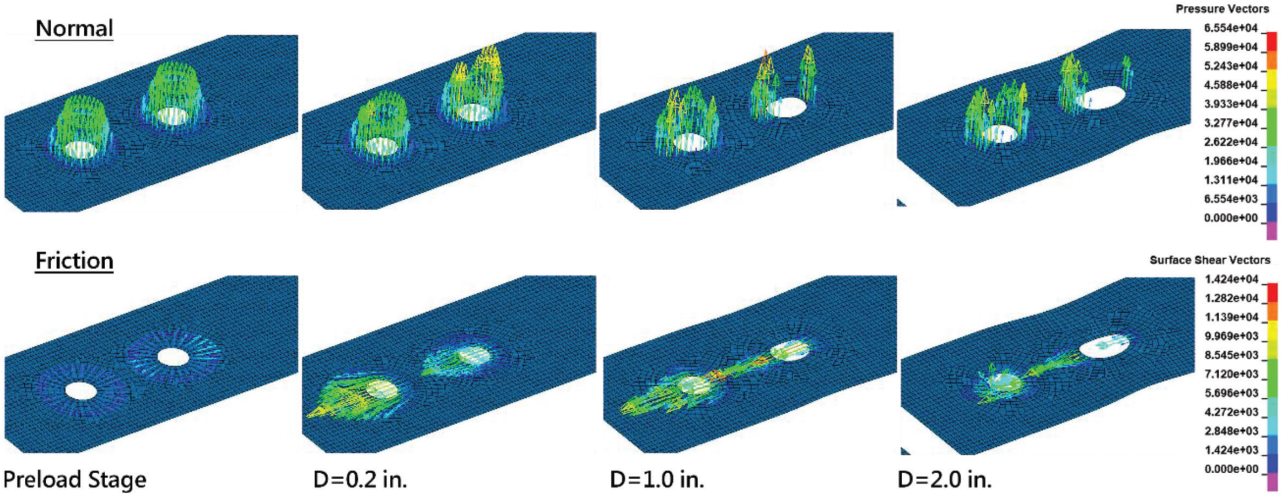

Fig. 35. Normal and friction stresses on the surface of the faceplate (Model 2).

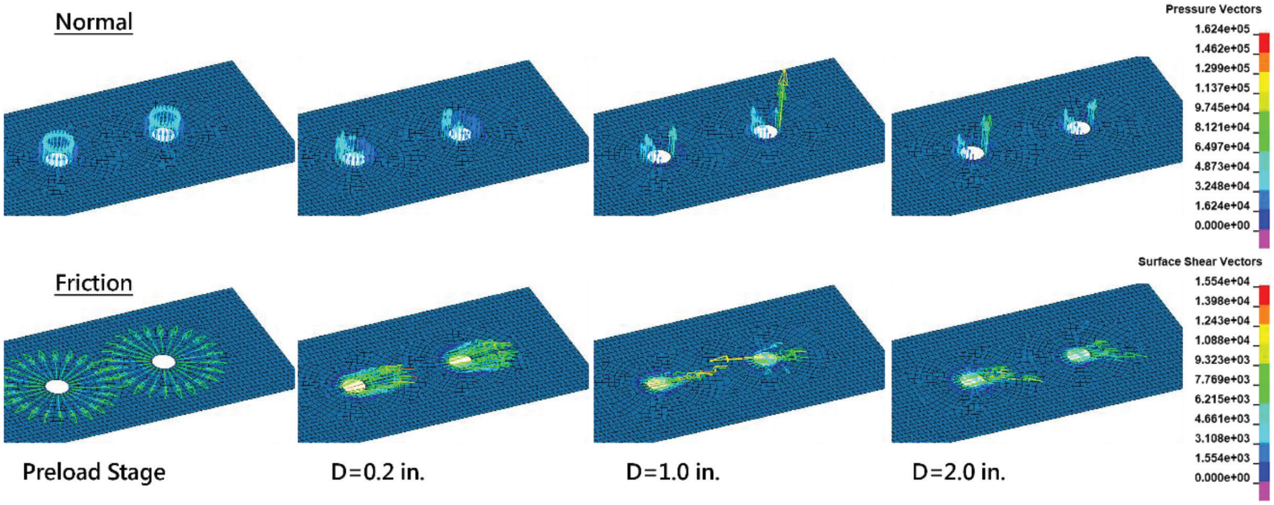

Fig. 36. Normal and friction stresses on the surface of the splice plate (Model 3).

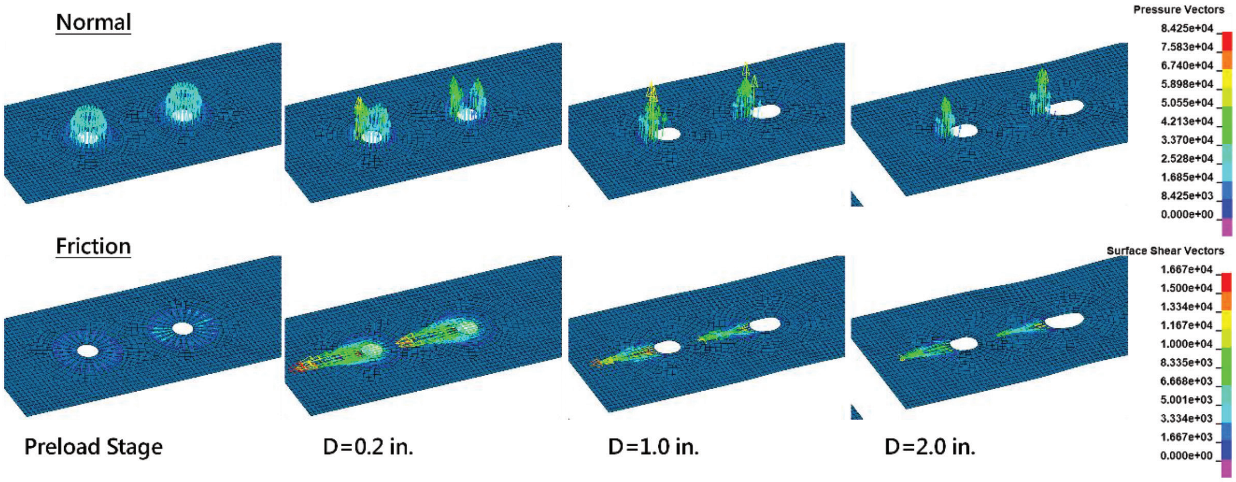

Fig. 37. *Normal and friction stresses on the surface of the faceplate (Model 3).*

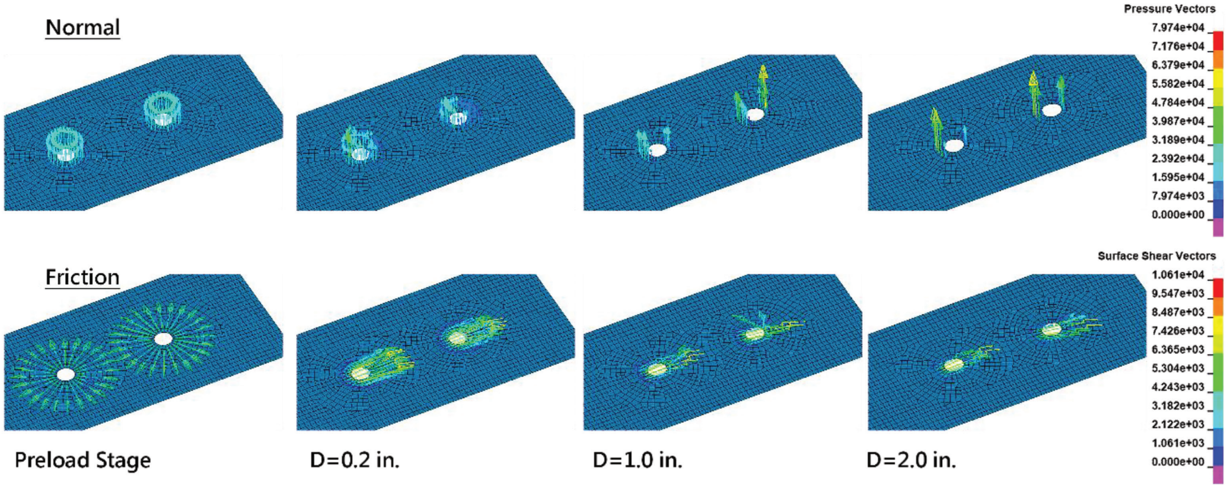

Fig. 38. *Normal and friction stresses on the surface of the splice plate (Model 4).*

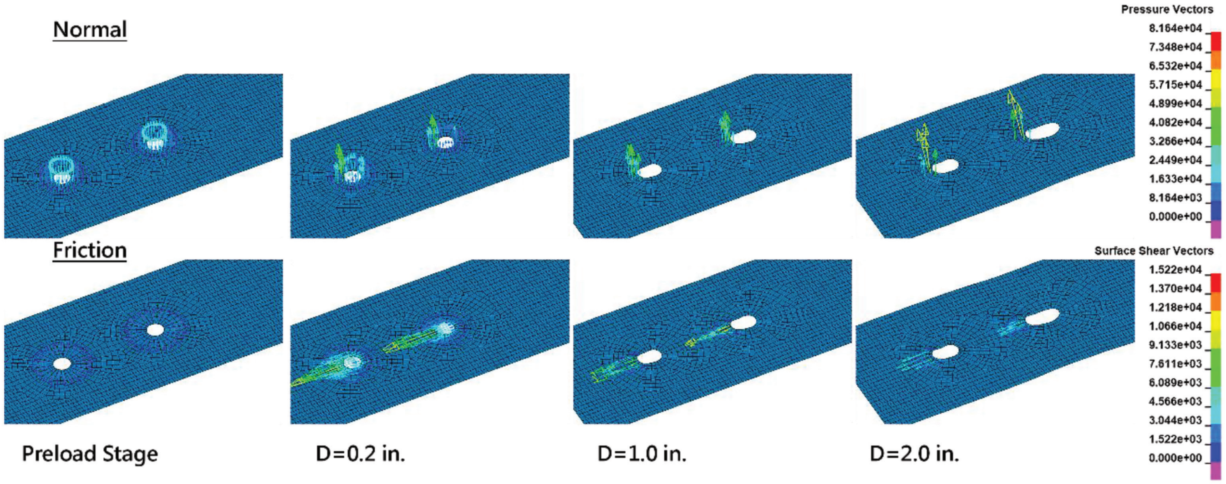

Fig. 39. *Normal and friction stresses on the surface of the faceplate (Model 4).*

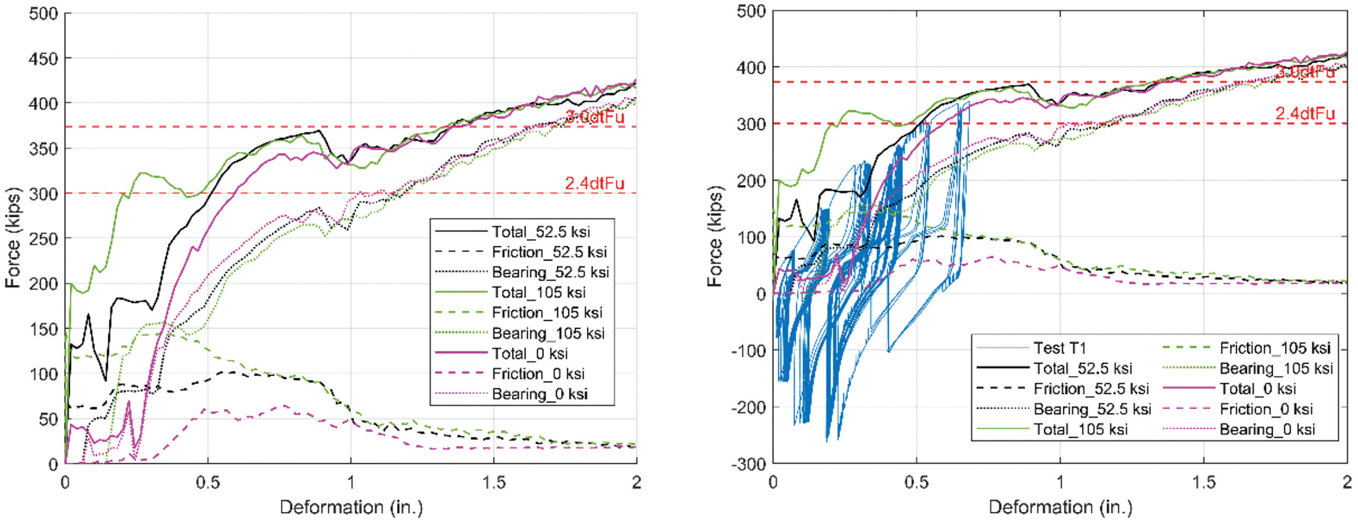

(a) FEM analysis results *(b) FEM analysis vs. test*

Fig. 40. Force-deformation curve of Model T1 with different pretensions.

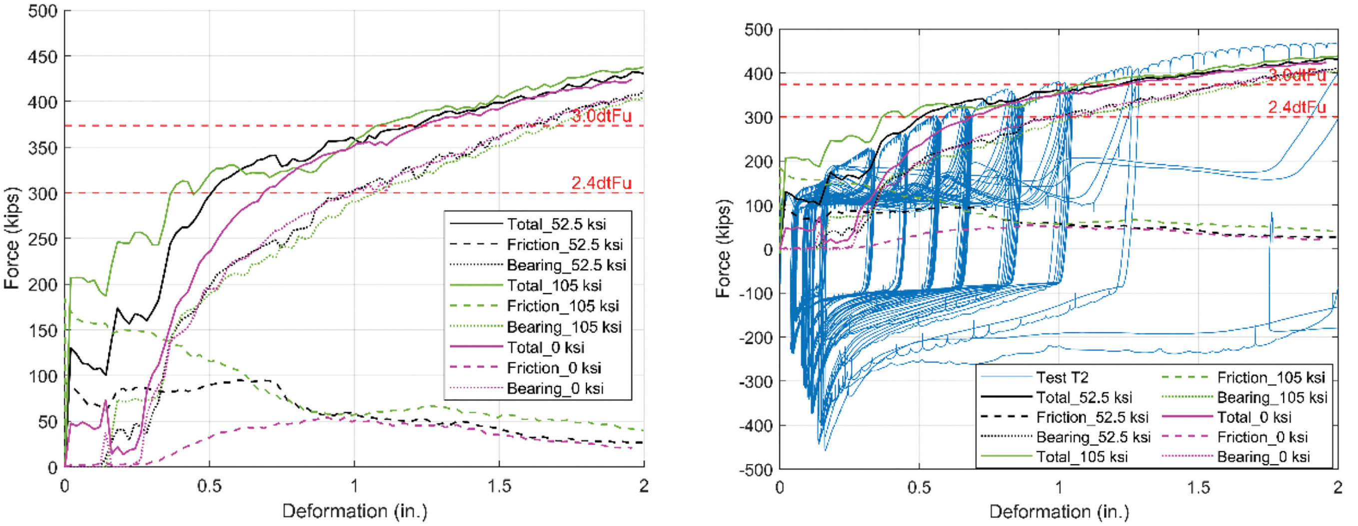

(a) FEM analysis results *(b) FEM analysis vs. test*

Fig. 41. Force-deformation curve of Model T2 with different pretensions.

was 1,126 kips, reached at −0.2 in. deformation. For comparison, the nominal axial strength of the connection can be calculated as:

$$P_{T,n} = A_s F_y + 0.85 A_c f_c' \\ = -1{,}194 \text{ kips} \tag{5}$$

where the compressive strength of concrete, f_c', is equal to 5.5 ksi. The peak strength reached by the numerical model is less than this value because the strength of the steel splice is governed by bearing, which developed at stresses over the plate cross section, A_s, of less than F_y. For comparison, at peak total strength in the numerical model, the average stress developed in the steel and concrete area was −17.5 ksi and −6.32 ksi, respectively. At that deformation level, bolts are bearing on the bolt holes but have not produced large hole deformations yet, as shown in Figure 47.

To investigate the load-transfer mechanisms that develop in the splice region, Figures 48 and 49 provide global and local free-body diagrams of the forces between steel plates and between steel and concrete there. All force components shown in the free-body diagrams are plotted in Figures 50 and 51. The force equilibrium formulas are presented below, and Figure 52 shows the results of these formulas, confirming compliance with force equilibrium.

$$sumG1 = P_{FP} - F_{r5} + F_6 - P_{SP1} - P_{SP2} \tag{6}$$

$$sumG2 = P_{FP} + F_{r1} + F_{r4} - F_{r5} - \\ B_1 + B_2 + B_3 - P_{SP1} - P_{SP2} \tag{7}$$

$$sumL1 = F_{r1} + F_{r4} + B_2 - P_{SP1} \tag{8}$$

$$sumL2 = P_{FP} - B_1 - F_{r2} - F_{r3} \tag{9}$$

$$sumL3 = F_{r3} + F_{r4} - F_{r5} + P_{FP} + B_3 - P_{SP2} \tag{10}$$

At the initial stage (before connection slip and at −0.01 in. deformation), the axial forces P_{FP}, P_{SP1}, and P_{SP2} were 46.2, 27.6, and 22.0 kips, respectively. At this stage, the friction forces F_{r2} and F_{r3}, each contributing 23.1 kips, reached their slip-critical state. Meanwhile, the friction forces F_{r1} and F_{r4} were −0.9 and 4.2 kips, respectively. After the connection slip, the axial forces P_{FP} and P_{SP1}, and the friction forces F_{r2} and F_{r3} remained unchanged as they were in plateau. However, the axial force P_{SP2} and friction force F_{r4} kept increasing and plateaued at 42.7 and 20.0 kips at a deformation of −0.05 in. At this point, the contact force F_6 acting on the nuts reached 17 kips.

It can be observed that the bearing force B_1 initiated at a deformation of −0.12 in. and continued to increase until it plateaued at 45 kips at −0.17 in. deformation. During this period, the axial force P_{FP} increased to 87 kips, and the axial force P_{SP1} rose to 42 kips, approaching the magnitude of P_{SP2}. Concurrently, the friction force F_{r1} changed from −3.3 to 20.7 kips, reaching its plateau at deformation of −0.17 in. Furthermore, the contact force F_6 changed from 11.3 to −2 kips. At a deformation of −0.23 in., the bearing forces acting on splice plates (B_2 and B_3) began to develop.

In other words, the sequence of events can be described as follows: When the axial load on the faceplate, P_{FP}, increased to the slip-critical resistance of bolts at a deformation of −0.01 in., the sliding intended to occur on the friction forces between faceplate and splice plate (F_{r2} and F_{r3}). However, the sliding was prevented because the nuts embedded inside concrete could not move. Between deformation of −0.01 to −0.05 in., the friction force between the bolt nut and inside splice plate, F_{r4}, the contact force between the bolt nut and concrete, F$_6$, and the axial force on the inside splice plate, P_{SP2}, continued to increase to a

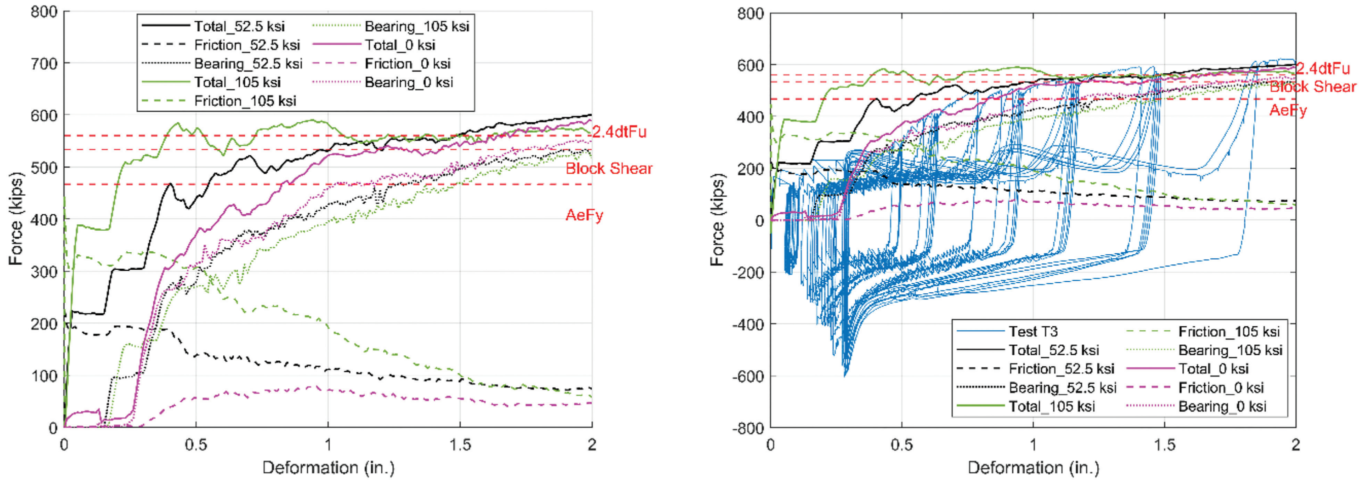

(a) *FEM analysis results*

(b) *FEM analysis vs. test*

Fig. 42. Force-deformation curve of Model T3 with different pretensions.

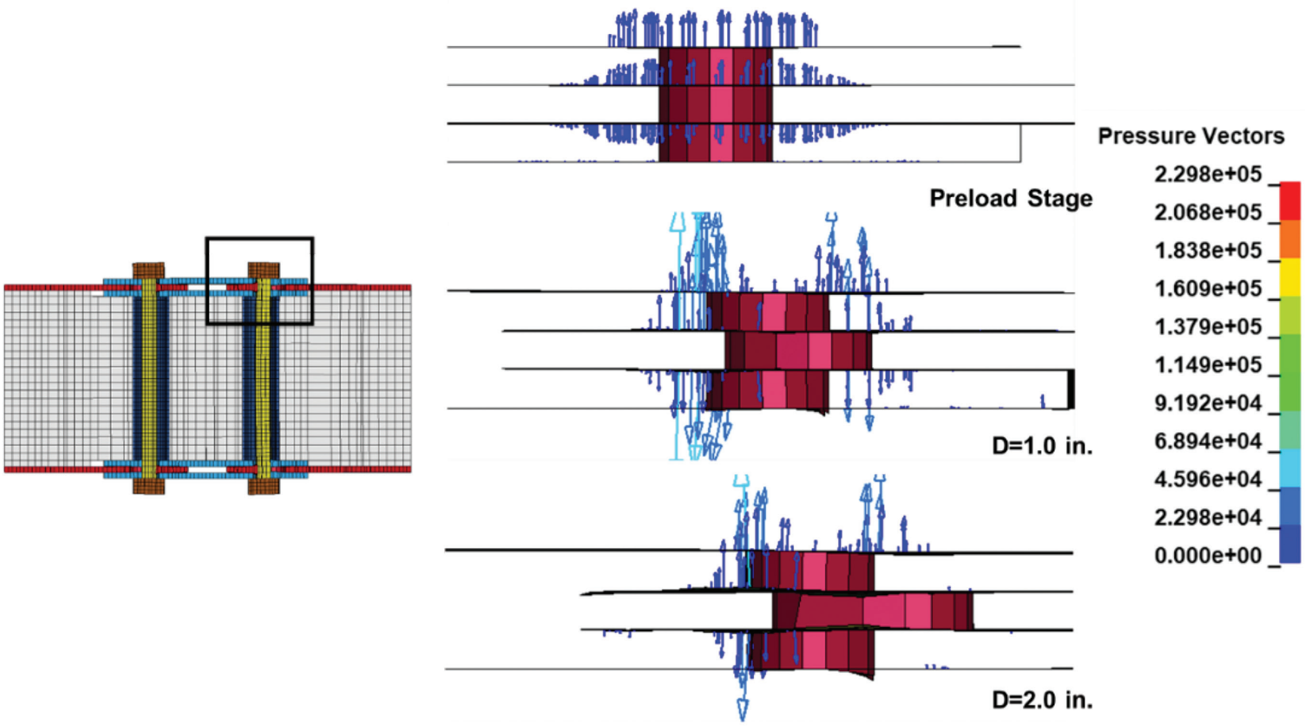

Fig. 43. Clamping stress vectors in Model T2.

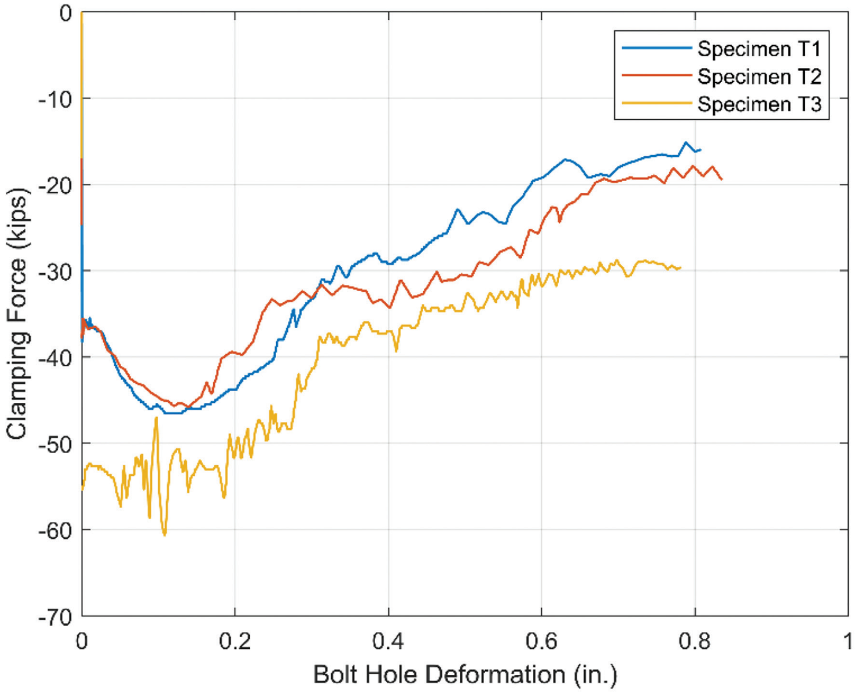

Fig. 44. Clamping force-hole deformation curve of Models T1–T3.

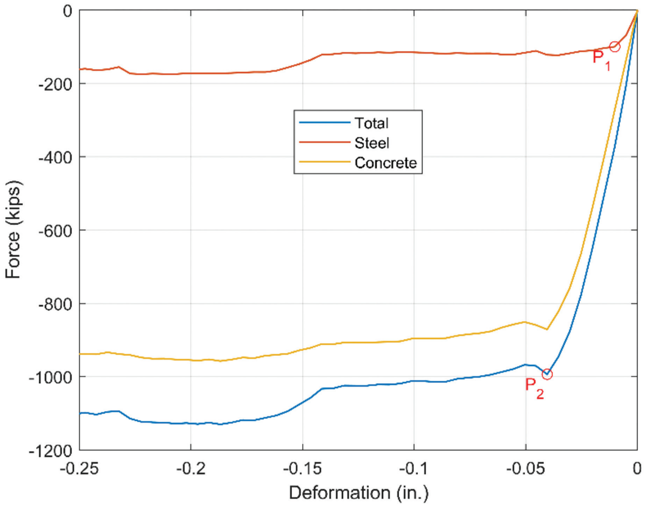

Fig. 45. Force-deformation curve of Model T1 in compression.

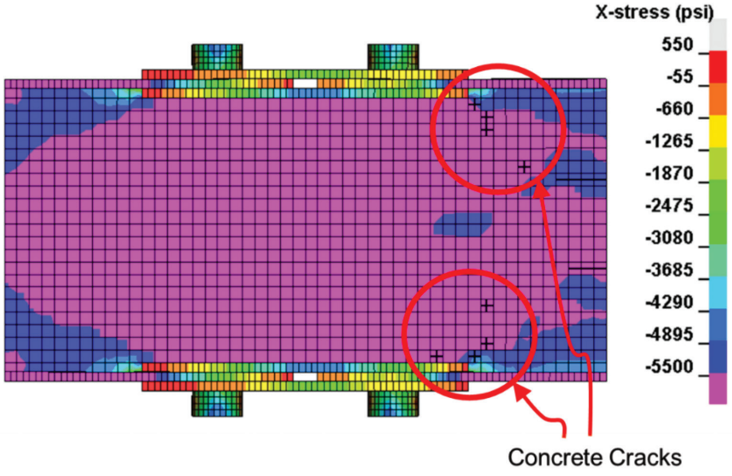

Fig. 46. Initiation of concrete cracks of Model T1 in compression.

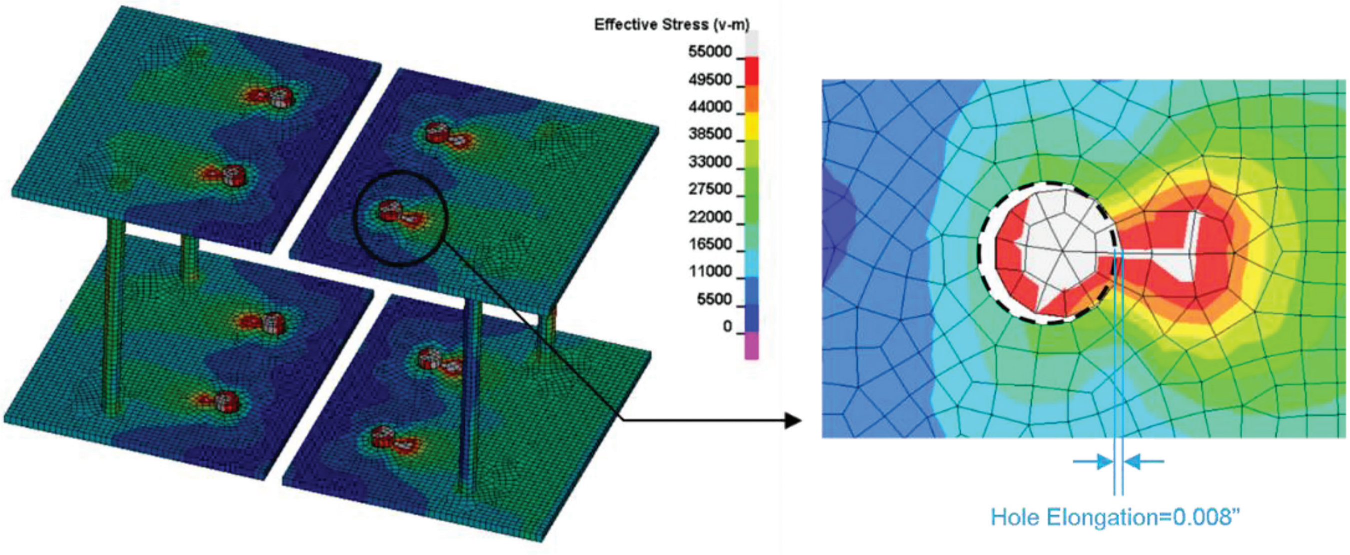

Fig. 47. Bolt hole elongation at −0.20 in. deformation.

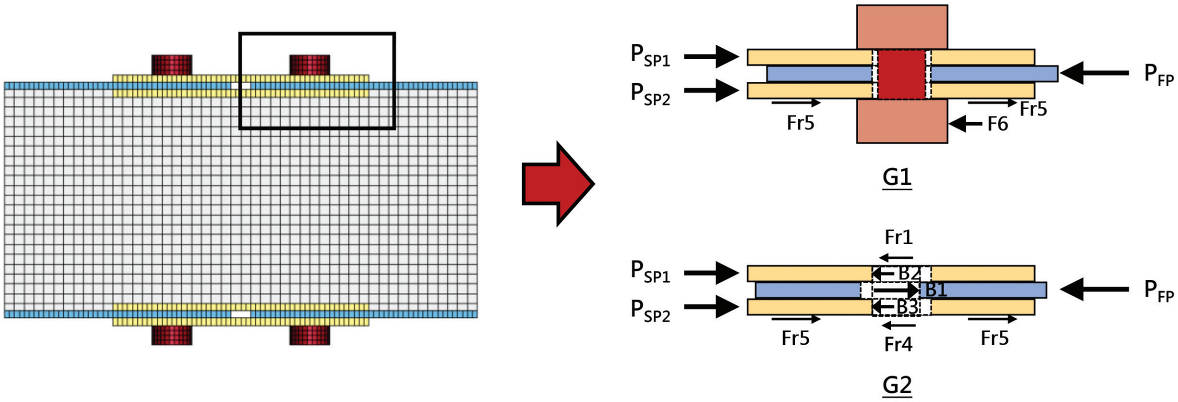

Fig. 48. Global free-body diagram of Model T1.

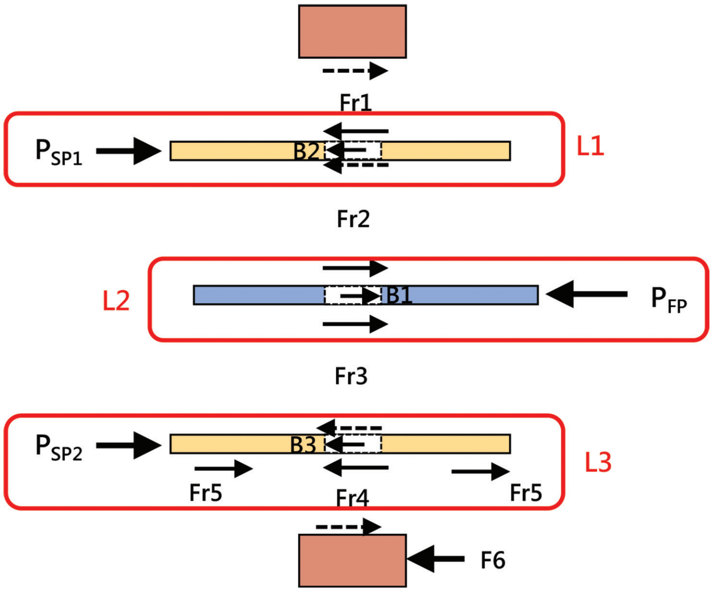

Fig. 49. Local free-body diagram of Model T1.

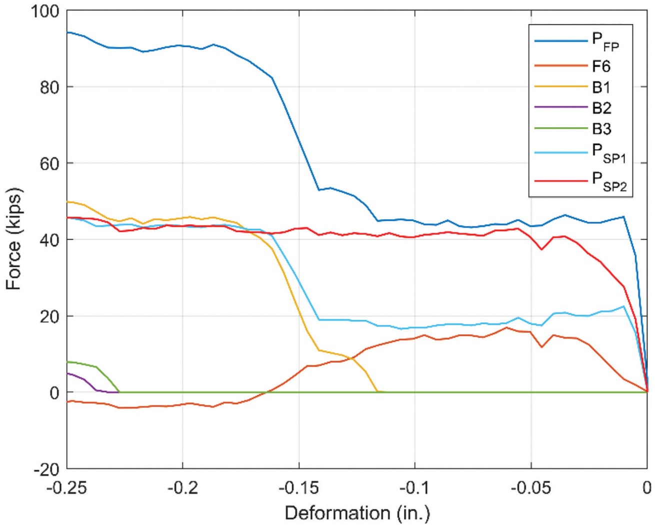

Fig. 50. Axial forces on steel plates and bearing forces in Model T1.

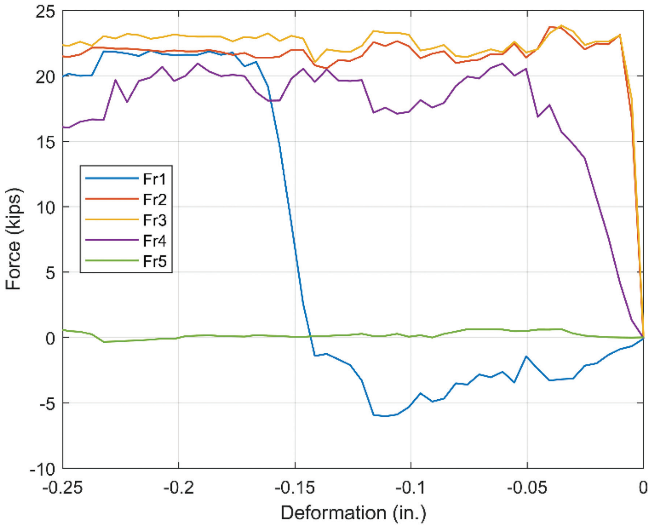

Fig. 51. Friction forces in Model T1.

plateau at a deformation of −0.05 in. After the bolt shank started touching bolt holes at a deformation of −0.12 in., the axial forces on the faceplate and splice plate, P_{FP} and P_{SP1}, bearing force on the faceplate, B_1, and friction force between the bolt head and the outside splice plate, F_{r1}, started to develop. These forces increased to a plateau until the bearing force on the faceplate, B_1, reached its plateau at a deformation of −0.17 in. Finally, at −0.23 in. deformation, the axial forces on the faceplate, P_{FP}, and the axial forces on the splice plates, P_{SP1} and P_{SP2}, increased again as the bearing forces splice plates, B_2 and B_3, started to develop.

During the preceding compressive deformation, the friction forces did not experience a significant reduction compared to the connection subjected to tension because the hole elongations are limited due to the presence of the concrete.

SUMMARY AND CONCLUSIONS

This study explored the effect of bolt pretension on bearing strength in bolted connections of all-steel and C-PSW/CF models through finite element analysis. Finite element models and simplified free-body diagrams with contact springs were used to examine the relationship of the clamping and bearing stress development in bolted connections. For connections under tension, friction forces generally decrease as the bolt hole elongation increases due to combined effects of the inelastic deformation and bending of bolt shanks, loss of contact area and stiffness in the initial contact springs, and thinning of the faceplates in tension due to Poisson's effect. These factors significantly impact the development of friction, indicating that for design, the bearing strength and slip-resistance strengths cannot be combined to calculate the overall strength of a bolted connection. In a bolted C-PSW/CF connection subjected to compression, the elongation of bolt holes due to bearing forces is restricted. Initially, the friction force reaches its slip-critical resistance, after which the axial force is transferred to the concrete. As the concrete reaches its compressive strength and begins to crack, its contribution diminishes, leading to the development of slip in the steel connection. The friction forces remain at a plateau before significant slip deformation occurs. While the creep effect of concrete is beyond the scope of this study, it is not anticipated to have a significant effect other than possibly slightly delaying the transfer of axial force to concrete once the friction force reaches its slip-critical resistance. Creep should not impact pretension when the material within the grip of the bolts is all steel, but it is unknown whether it could lead to a loss of pretension for the case of through rods with pipe-sleeves. This does not affect the conclusions of this study but may be investigated in future research.

ACKNOWLEDGMENTS

This research was supported by the Charles Pankow Foundation (CPF), the American Institute of Steel Construction (AISC), the MKA Foundation, and Atlas Tube/Zekelman through CPF research grant 02-21. All opinions, findings, conclusions, and recommendations presented in this paper are those of the authors and do not necessarily reflect the view of the sponsors. The researchers are also grateful

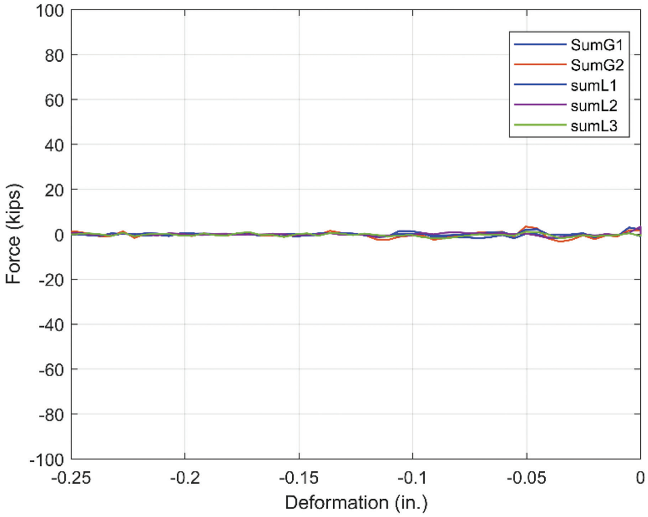

Fig. 52. Force equilibrium of Model T1.

for the technical guidance of its Project Advisory Group members (Glenn Bell, National Institute of Standards and Technology; Ron Klemencic, Chair and CEO, Magnusson Klemencic and Associates; Jim Malley, Senior Principal with Degenkolb Engineers; Rafael Sabelli, Principal and Director of Seismic Design, Walter P. Moore; Devin Huber, Director of Research at AISC; and Christopher Raebel and Larry Kruth, current and former Vice Presidents at AISC).

REFERENCES

Agrawal, S. (2020), "Seismic Design Coefficients for Composite Plate Shear Walls—Concrete Filled (C-PSW/CF)," Purdue University, West Lafayette, Ind.

AISC (2022a), *Seismic Provisions for Structural Steel Buildings*, ANSI/AISC 341-22, American Institute of Steel Construction, Chicago, Ill.

AISC (2022b), *Specification for Structural Steel Buildings*, ANSI/AISC 360-22, American Institute of Steel Construction, Chicago, Ill.

Alzeni, Y. (2014), "Cyclic Inelastic Behavior of Concrete Filled Sandwich Panel Walls Subjected to In-Plane Flexure," State University of New York at Buffalo, Buffalo, N.Y.

Alzeni, Y. and Bruneau, M. (2017), "In-Plane Cyclic Testing of Concrete-Filled Sandwich Steel Panel Walls with and without Boundary Elements," *Journal of Structural Engineering*, Vol. 143, No. 9. https://doi.org/10.1061/(asce)st.1943-541x.0001791

ASCE (2022), *Minimum Design Loads and Associated Criteria for Buildings and Other Structures*, ASCE/SEI 7-22, American Society of Civil Engineers, Reston, Va.

Back, J.D. and Bouwman, L.P. (1959), "The Friction Factor under Influence of Different Tightening Methods of the Bolts and of Different Conditions of the Contact Surfaces," Report 6-59-9-VB-3, Stevin Laboratory, Delft University of Technology, Delft, the Netherlands.

Brown, J.D., Lubitz, D.J., Cekov, Y.C., Frank, K.H., and Keating, P.B. (2007), "Evaluation of Influence of Hole Making upon the Performance of Structural Steel Plates and Connections," Report No. FHWA/TX-07/0-4624-1, University of Texas at Austin, Austin, Tex.

Franceschetti, N. and Denavit, M.D. (2021), "Tearout Strength of Concentrically Loaded Bolted Connections," *Engineering Journal*, AISC, Vol. 58, No. 3. https://doi.org/http://dx.doi.org/10.62913/engj.v58i3.1180

Frank, K.H. and Yura, J.A. (1981), "An Experimental Study of Bolted Shear Connections," Report DOT-FH-11-8900, Federal Highway Administration, Washington, D.C.

Hallquist, J.O. (2006), *LS-DYNA® Theory Manual*, Livermore Software Technology Corporation (LSTC), Livermore, Calif.

Hirano, M. (1970), "Bearing Stresses in Bolted Joints," Society of Steel Construction of Japan, Vol. 6, No. 58.

Jones, J. (1958), "Bearing-Ratio Effect on Strength of Riveted Joints," *Transactions ASCE*, Vol. 123, pp. 964–972.

Kim, H.J. and Yura, J.A. (1996), "The Effect of End Distance on the Bearing Strength of Bolted Connections," University of Texas at Austin, Austin, Tex.

Kizilarslan, E. (2021), "Experimental and Analytical Inelastic Behavior of C- and T-Shaped Composite Plate Shear Walls/Concrete-Filled (C-PSW/CF)," State University of New York at Buffalo, Buffalo, N.Y.

Kizilarslan, E. and Bruneau, M. (2021), "Hysteretic Behavior of Repaired C-Shaped Concrete Filled-Composite Plate Shear Walls (C-PSW/CF)," *Engineering Structures*, Vol. 241. https://doi.org/10.1016/j.engstruct.2021.112410

Kizilarslan, E. and Bruneau, M. (2023), "Cyclic Behavior of T-Shaped Composite Plate Shear Walls–Concrete Filled," *Journal of Structural Engineering*, Vol. 149, No. 8. https://doi.org/10.1061/jsendh.Steng-11693

Kulak, G.L., Fisher, J.W., and Struik, J.H.A. (1987), "Guide to Design Criteria for Bolted and Riveted Joints," RCSC, Chicago, Ill.

Lewis, B.E. and Zwememan, F.J. (1996), "Edge Distance, Spacing, and Bearing in Bolted Connections," Oklahoma State University, Stillwater, OK.

Liu, J.-H. and Bruneau, M. (2024), "Cyclic Tension Behavior of Concrete Filled Composite Plate Shear Wall Components having Bolted Splices" (under review), *Engineering Structures*.

Može, P. (2018), "Bearing Strength at Bolt Holes in Connections with Large End Distance and Bolt Pitch," *Journal of Constructional Steel Research*, Vol. 147, pp. 132–144. https://doi.org/10.1016/j.jcsr.2018.04.006

Nunse, W.H. (1959), "The Effect of Bearing Pressure on the Static Strength of Riveted Connections," *Bulletin 454*, Engineering Experiment Station, University of Illinois, Urbana, Ill.

Polat, E. and Bruneau, M. (2018), "Cyclic Inelastic In-Plane Flexural Behavior of Concrete-Filled Sandwich Steel Panel Walls," *Engineering Journal*, AISC, Vol. 55, No. 1, pp. 45–76.

Sener, K.C. and Varma, A.H. (2014), "Steel-Plate Composite Walls: Experimental Database and Design for Out-of-Plane Shear," *Journal of Constructional Steel Research*, Vol. 100, pp. 197–210. https://doi.org/10.1016/j.jcsr.2014.04.014

Shafaei, S., Varma, A.H., Seo, J., and Klemencic, R. (2021), "Cyclic Lateral Loading Behavior of Composite Plate Shear Walls/Concrete Filled," *Journal of Structural Engineering*, Vol. 147, No. 10. https://doi.org/10.1061/(asce)st.1943-541x.0003091

Varma, A.H., Malushte, S.R., Sener, K., and Lai, Z. (2014), "Steel-Plate Composite (SC) Walls for Safety Related Nuclear Facilities: Design for In-Plane and Out-of-Plane Demands," *Nuclear Engineering and Design*, Vol. 269, pp. 240–249.

Guide for Authors

Scope *Engineering Journal* is dedicated to the improvement and advancement of steel construction. Its pages are open to all who wish to report on new developments or techniques in steel design, research, the design and/or construction of new projects, steel fabrication methods, or new products of significance to the uses of steel in construction. Only original papers should be submitted.

General Papers intended for publication should be submitted by email Margaret Matthew, editor, at **matthew@aisc.org**.

The articles published in the *Engineering Journal* undergo peer review before publication for (1) originality of contribution; (2) technical value to the steel construction community; (3) proper credit to others working in the same area; (4) prior publication of the material; and (5) justification of the conclusion based on the report.

All papers within the scope outlined above will be reviewed by engineers selected from among AISC, industry, design firms, and universities. The standard review process includes outside review by an average of three reviewers, who are experts in their respective technical area, and volunteers in the program. Papers not accepted will not be returned to the author. Published papers become the property of the American Institute of Steel Construction and are protected by appropriate copyrights. No proofs will be sent to authors.

Manuscripts Manuscripts must be provided in Microsoft Word format. Include a PDF with your submittal so we may verify fonts, equations and figures. View our complete author guidelines at **aisc.org/ej**.

Smarter. Stronger. Steel.

American Institute of Steel Construction
130 E Randolph St, Ste 2000, Chicago, IL 60601
312.670.2400 | aisc.org/ej